



UNIVERSITÀ DI PISA

Department of Physics Masters Degree in Physics

Characterization of monolithic CMOS pixel sensors for charged particle detectors and for high intensity dosimetry

6 Candidate:
Ravera Eleonora

Supervisor:
Francesco Forti

7 Academic year 2021/2022

⁸ Contents

⁹ Introduction	5
¹⁰ 1 Use of pixel detectors	6
11 1.1 Tracking in HEP	6
12 1.1.1 Hybrid Pixels at LHC	8
13 1.1.2 Monolithic Active Pixels	9
14 1.2 Other applications	13
15 1.2.1 Applicability to FLASH radiotherapy	13
¹⁶ 2 Pixel detectors	18
17 2.1 Signal formation	18
18 2.2 Charge Coupled Devices	20
19 2.3 Hybrid pixels	20
20 2.4 CMOS MAPS and DMPAS	22
21 2.4.1 DMAPS: large and small fill factor	23
22 2.4.2 A modified sensor	24
23 2.5 Analog front end	26
24 2.5.1 Preamplifier	26
25 2.6 Readout logic	27
²⁶ 3 MAPS devices description	30
27 3.1 The sensor	31
28 3.2 Front end	33
29 3.2.1 ALPIDE-like	34
30 3.3 Readout logic	35
31 3.4 The sensor and the front end	39
32 3.5 Readout logic and data structure	40
33 3.5.1 Matrix division and data-packets	40
34 3.5.2 Matrix division and data-packets	41
³⁵ 4 Characterization	45
36 4.1 TJ-Monopix1 characterization	45
37 4.1.1 Threshold and noise: figure of merit for pixel detectors	45
38 4.1.2 Linearity of the ToT	49
39 4.1.3 Calibration of the ToT	50
40 4.1.4 Changing the bias	55
41 4.1.5 Measurements with radioactive sources	56
42 4.1.6 Dead time measurements	61

43	4.2 ARCADIA-MD1 characterization	63
44	5 Test beam measurements	67
45	5.1 Apparatus description	68
46	5.1.1 Accelerator	68
47	5.1.2 Mechanical carriers	68
48	5.2 Measurements	69
49	Bibliography	74

50 Introduction

51 Since the 1980s, when the fabrication of device with very small electrodes (50-100 μm)
52 became a practical possibility, pixel detectors have been widely employed for imaging and
53 tracking charged particles in the vertex region of experiments at accelerators. Thanks to
54 their excellent spatial resolution, today even better than 10 μm , they allow for true three
55 dimensional space-point determination even at high particle fluxes and in particular for
56 the identification of secondary vertices of short-lived particles such as τ and B mesons.
57 Requirement imposed by accelerators are stringent and they will become even more so
58 with the increase of luminosity; in this scenario CMOS Monolithic Active Pixel Sensors
59 (MAPS), based on the technology of CMOS cameras, are being developed to improve
60 the performance of the hybrid pixel detectors, which currently constitute the state-of-art
61 for large scale pixel detector, in particular by reducing the amount of material, power
62 consumption and pixel dimension. Indeed, while hybrid pixels are made by two parts, the
63 sensor and the electronics, welded together through microconnections, the MAPS integrate
64 them all on the same wafer.

65 Experiments such as ALICE at LHC and STAR at RHIC have already introduced the
66 CMOS MAPS technology in their detectors. ALICE Tracking System (ITS2), upgraded
67 during the LHC long shut down in 2019-20, was the first large-area ($\sim 10 \text{ m}^2$) silicon vertex
68 detector based on CMOS MAPS. Thanks to the reduction of the material budget, ITS2,
69 which uses the ALPIDE chip developed by ALICE collaboration, obtained an amazing im-
70 provement both in the position measurement and in the momentum resolution, improving
71 the efficiency of track reconstruction for particle with very low transverse momentum (by
72 a factor 6 at $p_T \sim 0.1 \text{ GeV}/c$). Further advancements in CMOS MAPS technology are
73 being aggressively pursued for the ALICE ITS3 and the Belle II vertex detector upgrades
74 (both foreseen around 2026-27), and by the R&D53 collaboration for the upgrade at HL-
75 LHC, with the goals of further reducing the sensor thickness and improving the readout
76 speed of the devices, while keeping power consumption at a minimum.

77 Beside tracking, the development of pixel detectors is a very active field with many
78 applications: a noteworthy example of detector originally used in particle physics and later
79 employed for medical imaging, in space detectors and for art authentication, is Medipix,
80 a hybrid system developed at CERN within the Medipix collaboration. Among medical
81 applications, a possible use of CMOS MAPS could be in dosimetry: in the last few years
82 the search of radiotherapy oncological treatments with high intensity beams (FLASH
83 mode) is requiring new dosimeters, both for the therapies as well as new beam-monitors
84 (especially for focused very high energy electron beams), which are capable of deal with
85 extreme dose rate (up to 40 Gy/s).

86 I have studied the characteristics of two ALPIDE-like CMOS MAPS chips and tested
87 them under different front end configuration. The first chip, the TJ-Monopix1 from the
88 Monopix series, is a TowerJazz MAPS fabricated in 180 nm CMOS technology with an

active area of $1 \times 2 \text{ cm}^2$ (448×224 pixels) and is one of the prototypes for the Belle II vertex detector upgrade. The second chip, called Main Demonstrator-1, has an active area of $1.28 \times 1.28 \text{ cm}^2$ (512×512 pixels) is produced by LFoundry in 110 nm CMOS technology and designed by the ARCADIA (Advanced Readout CMOS Architectures with Depleted Integrated sensor Arrays) group; it is intended to be a general purpose device with possible use in medical scanners, space experiments, future lepton colliders and also possibly X-ray applications with thick substrates. The main differences between the two chips are in the output signal type and in the readout sequence of the matrix. Concerning the former, TJ-Monopix1 returns an analog output information, that is the time over threshold of the pulse, which can be related with the charge released by the particle in the sensor, while MD1 returns only a digital information; regarding the latter, instead, TJ-Monopix1 has a completely sequential readout, while MD1 roughly combines the information of the hits before the readout in order to reduce the data transmission time.

I have set up the test systems for the two chips in the INFN clean laboratories and characterized the devices electrically and with radioactive sources in terms of threshold, noise, dead time and analog response. The mean minimum stable threshold evolved through different generation of chips and nowadays it is less than 500 e^- , allowing thinner sensors with smaller signals: TJ-Monopix1 has proven to be in agreement with this trend, having a threshold of $\sim 400 \text{ e}^-$, to be compared with the 2000 e^- signal expected for a minimum ionizing particle in an epitaxial layer of $25 \mu\text{m}$. Moreover, since one of the main challenges of MAPS are the differences between pixels due to process parameters variation across the wafer, which make the sensor response nonuniform, I have measured the threshold and noise dispersion across the matrix, which I found to be 40 e^- and 2 e^- respectively. I have also studied the response of the analog signal recorded by TJ-Monopix1, that is the time over threshold, and performed a calibration of its absolute value using a Fe55 X-ray source. All these measurements are important to verify the design parameters of the chip and to validate the chip simulation.

As conclusion of the measurement campaign, we have tested TJ-Monopix1 at very high intensity using the electron beam of the new ElectronFlash accelerator designed for both medical research and R&D in FLASH-radiotherapy and recently installed at Santa Chiara hospital in Pisa. I have participated in the design of the setup needed for testbeam measurement and I am currently working on the analysis of the data collected.

₁₂₁ **Chapter 1**

₁₂₂ **Use of pixel detectors**

₁₂₃ In the following sections I will use terms such as hybrid pixels, monolithic active pixel system (MAPS), Charge Coupled Devices (CCDs), Depleted Field Effect Transistor sensors (DEPFET) that will be discussed in 2 [disclaimer](#)

₁₂₆ The relation between the development of cameras and that of pixel detectors dates back to 1969, when the idea of CCDs, for which Boyle and Smith were awarded the Nobel Prize in Physics in 2009, revolutionized photography allowing light to be captured electronically instead of on film. Even though the CMOS technology already existed at the time the ₁₂₈ CCDs spread, the costs of production were too high to allow the diffusion of these sensors ₁₃₀ for the following 20 years. From that moment on, the fast diffusion of CMOS was mainly ₁₃₂ due to the lower cost than CCD, and the lower power supply required. Nowadays CCDs ₁₃₃ are still preferred over MAPS in astronomy, where the astronomical sources' rate are low ₁₃₄ enough to cope with slow readout time (tens of ms).

₁₃₅ The principal use cases of pixel detectors are particle tracking and imaging: in the former case individual charged particles have to be identified, in the latter instead an ₁₃₇ image is obtained by the usually un-triggered accumulation of the impinging radiation. ₁₃₈ Also the demands on detectors performance depends on their usage, in particular tracking ₁₃₉ requires high spatial resolution, fast readout and radiation hardness. This chapter tries to ₁₄₀ summarize the main applications of pixel detectors, while a description of the technological ₁₄₁ implementation is presented in 2

₁₄₂ **1.1 Tracking in HEP**

₁₄₃ In the early days of high-energy physics gaseous detector were used for tracking and ₁₄₄ there was no need to replace them since they had a sufficient spatial resolution ($100 \mu\text{m}$). ₁₄₅ Since 1974, with the measurement of the invariant mass of the J/Psi and the affirmation ₁₄₆ of the quark model, all experiments start to look for better spatial resolutions in order to ₁₄₇ achieve the possibility of reconstructing short lived particles and measuring their decay lengths.

₁₄₉ Historically, the first pixel detector employed in particle physics was a CCD: it was ₁₅₀ installed in the spectrometer at the CERN's Super Proton Synchrotron by the ACCMOR ₁₅₁ Collaboration (Amsterdam, CERN, Cracow, Munich, Oxford, RAL) in the mid 1980s, ₁₅₂ with the purpose of studying the (at the time) recently-discovered charmed particles. ₁₅₃ The second famous usage of CCDs took place in the SLAC Large Detector at SLAC ₁₅₄ linear collider in the years 1996-98, where the CCD technology was adopted instead of

155 the microstrip detectors for their excellent spatial resolution (cell size $22 \times 22 \mu\text{m}^2$ giving
156 a resolution of $\sim 5 \mu\text{m}$) thanks to the sufficient time for readout between two successive
157 collisions (160 ms).

158 From that period on, particle tracking in HEP experiments has been transformed
159 radically. It became mandatory to build a inner vertex detector, with the following tasks:

- 160 • pattern recognition with the identification of particle tracks even in the presence of
161 large backgrounds and pile-up
- 162 • measurement of vertices (primary and secondary)
- 163 • multi-track and vertex separation in the core of jets
- 164 • measurement of specific ionization
- 165 • momentum measurement combining with the information from other detectors

166 The more demanding requirements led to the development of hybrid pixel detectors
167 satrting from 1990s: a dedicated collaboration, RD19, was established at CERN with the
168 specific goal of defining a semiconductor micropattern detector with an incorporated signal
169 processing at a microscopic level. In those years a wide set of prototypes of hybrid pixel has
170 been manufactured; among the greatest productions a mention goes to the huge ATLAS
171 and CMS vertex detectors. From the middle of 2013 a second collaboration, RD53, has
172 been established with the new goal of finding a pixel detector suitable for the phase II in
173 future upgrades of those experiments. Even if the collaboration is specifically focused on
174 the design of hybrid pixel readout chips (aiming to 65 nm tecnique), also other options have
175 been taken in account and many test have been done on MAPS. Requirements imposed by
176 LHC are stringent and they will become even more with the increase of luminosity at HL-
177 LHC: for example, a dose and radiation of **5 Mrad** and $10^{16} \text{ 1MeV n}_{eq}/\text{cm}^2$ are exepcted
178 after 5 years of operation. Time resolution, material budget and power consumption
179 are also issues for the upgrade: to distinguish different events from different bunches a
180 time resolution better than 25 ns for a bunch crossing frequency of 40 MHz is required, a
181 material budget lower than $2\% X_0$ and a power consunption lower than 500 mW/cm^2 are
182 required.

183 Amidst the solutions proposed to improve radiation robustness of the sensor, 3D silicon
184 detector, invented by Sherwood Parker in 1995, are very promising. In 3D sensors the
185 electrode is a narrow column of n-type implanted vertically across the bulk instead of being
186 implanted on the wafer's surface. The charge produced by the impinging particle is then
187 drifted transversally within the pixel, and, as the mean path between two electrode can
188 be souffcient low, the trap probability is not an issue. Even if 3D detector are adequately
189 radiation hard and are a possible solution for hybrid pixel modules, especially in the
190 innermost pixel detector layer, their fabrication process is currently low volume, making
191 them unlikely to cover large areas. Another promising possibility is to use fast Monolitich
192 Active Pixels systems which could allow the reduction of material budget and improve
193 spatial resolution.

194 **1.1.1 Hybrid Pixels at LHC**

195 **ATLAS**

196 ATLAS is one of two general-purpose detectors at the LHC and has the largest volume
197 detector ever constructed for a particle collider (46 m long and 25 m in diameter). The
198 Inner Detector (ID) consists of three different systems all immersed in a magnetic field
199 parallel to the beam axis whose main components are: the pixel, the micro-strips and
200 transition radiation trackers. Concerning the pixel detector, they installed a 3-layer hybrid
201 pixel detector in 2007 and an additional one inserted within the original detector envelope
202 and therefore called insertable B-layer (IBL) in 2014. 92 million pixels are divided in 4
203 barrel layers and 3 disks in each end-cap region, covering a total area of 1.9 m^2 and having
204 a 15 kW of power consumption.

205 As stated by the ATLAS collaboration the pixel detector is exposed by an extreme
206 particle flux: "By the end of Run 3¹, the number of particles that will have hit the
207 innermost pixel layers will be comparable to the number it would receive if it were placed
208 only a few kilometres from the Sun during a solar flare". Considering that the particle
209 density will increase even more with HL-LHC, radiation hardness is definitively a target
210 to achieve. Hybrid pixels will be used at the start of high-luminosity application, although
211 an active development of monolithic devices is ongoing for possible future use in the outer
212 pixel layers. The TJ-Monopix1 which I will describe in 3 is part of this development.

213 The sensor will be bonded with ITkPix, the first full-scale 65 nm hybrid pixel-readout
214 chip developed by the RD53 collaboration. Regarding the sensor, a valuable option is
215 using 3D pixels, which have already proved themselves in ATLAS, for the IBL, where they
216 were introduced in a limited acceptance range and introduced a new readout integrated
217 circuit called FE-I4. Also the complexity of the readout will be raised, as the number of
218 pixels will be increased of a factor about 7, passing from 92 millions to 6 billion.

219 **CMS**

220 The CMS hybrid pixel detector has been upgraded in 2017, when, with the replacement
221 of a piece of the beam pipe, a layer has been added to the detector at 3 cm from it.
222 124 million pixels are divided between the barrel pixel detector (BPIX) and the forward
223 disks (FPIX), with sensors which are different from each other and produced by different
224 foundries. The sensors have an area equal to 100 μm by 150 μm and have been produced
225 on 285 μm to 300 μm thick wafers.

226 The time resolution is 25 ns, and the information coming from the detector are stored on
227 chip for the Level-1 trigger latency ($\sim 4 \mu\text{s}$). The upgrade baseline ROIC was redesigned for
228 the outer 3 layers, replacing analog signal readout with on-chip ADCs and digital readout
229 at higher rate. reads out the pulse height information for each pixel.

230 **LHCb**

231 LHCb is a dedicated heavy-flavour physics experiment that exploits pp interactions at
232 14 TeV at LHC. It was the last experiment to upgrade the vertex detector, the Vertex
233 Locator (VELO), replacing the silicon-strip with 26 plane pixel detector (because of the
234 fixed target geometry) in May 2022. As the instantaneous luminosity in Run3 is increased
235 by a factor $\lesssim 10$, much of the readout electronics and of the trigger system have been

¹Run 3 start in June 2022

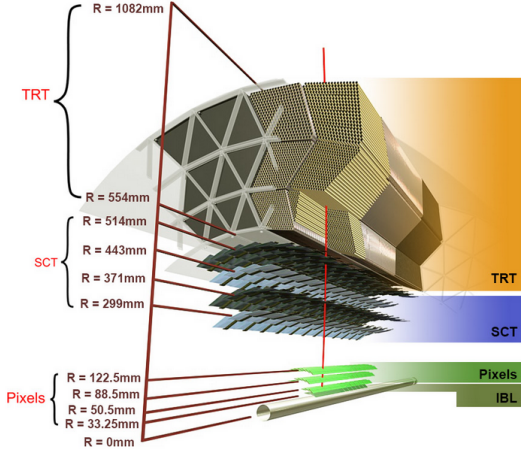


Figure 1.1: ATLAS tracker detector

236 developed in order to cope with the large interaction rate. To place the detector as close as
 237 possible to the beampipe and reach a better track reconstruction efficiency and resolution,
 238 the VELO has a surprising feature: during the injection of LHC protons it is parket at
 239 3 cm from the beams and only when the stability is reach it is moved at \sim 5 mm. Readout
 240 speed is a priority for the detector that use a triggerless readout at 40 MHz collision rate,
 241 producing 20 Gbps per ROIC. The Velopix, which is the hybrid system designed for LHCb,
 242 is made bonding sensors, each measuring 55×55 micrometers, 200 μm -thick to a 200 μm -
 243 thick ASIC specially developed for LHCb and coming from the Medipix family (sec. ??),
 244 which can handles hit rates up to 900 MHz per chip. Since the detector is operated under
 245 vacuum near the beam pipe, the heat removal is particularly difficult and evaporative CO₂
 246 microchannel cooling are used.

247 1.1.2 Monolithic Active Pixels

248 MIMOSA at EUDET and STAR

249 MIMOSA [6][7] (standing for Minimum Ionizing MOS Active pixel sensor), designed in
 250 2008, prefigured the architecture of MAPS for coming vertex detector being the first large
 251 scale sensor to be employed as detector. MIMOSA-26 equiped the final version of EUDET
 252 high resolution beam telescope both at CERN-SPS and at DESY while the MIMOSA-28
 253 devices are used for the first MAPS-based vertex detector at the STAR experiment at
 254 RHIC. MIMOSA-26 is fabricated in a 350 nm CMOS technology, and a module features
 255 1152 columns, split into 18 independent groups, and 576 rows, with square pixels having a
 256 side of 18.4 μm lenght; the epitaxial layer is not fully depleted and the charge collection is
 257 mostly by diffusion, resulting in charge sharing between pixels and collection time bigger
 258 than 100 ns.

259 The chip is an Active Pixels (APS) and therefore it incorporates the amplification on
 260 pixel, while the signal discrimination and zero-suppression logic are placed at the End of
 261 Column: the readout is done in a rolling shutter mode with a frame integration time that
 262 can be lowered down to 85 ms, and a memory allowing to store up to six hits is.

263 The EUDET telescope, equipped with six sensor planes, requires highly granular and
 264 thin pixel detectors in order to achieve an excellent track resolution (around 2 μm) even at



Figure 1.2: (a) Block-diagram of the ULTIMATE-2 sensor. (b) The HFT pixel detector of STAR;

265 the rather low particle energies of up to 6 GeV. The STAR experiment at the Relativistic
 266 Heavy Ion Collide (RHIC) accelerator at the Brookhaven National Laboratory (BNL) is
 267 the first to include MAPS in the vertex detector[8]. The main tracking detector in STAR is
 268 a TPC with radii 60-190 cm embedded in a 0.5 T solenoidal magnetic field, that provides
 269 a pointing resolution of approximately 1 mm. The pixel detector, PXL, is a part of a
 270 3-detector system, Heavy Flavor Tracker (HFT), that has been added to the pre-existing
 271 STAR apparatus just before the 2014 Run in order to improve the impact parameter
 272 resolution and to enable the direct reconstruction of hadronic decays of heavy flavor mesons
 273 and baryons. The Heavy Flavor Tracker (HFT) is composed by the Silicon Strip Detector
 274 (SSD), the Intermediate Silicon Tracker (IST) and the Pixel Detector (PXL); the first
 275 one is placed at 22 cm from the beam pipe and consists of double sided strips with 95 μm
 276 inter-strip pitch, the second one, placed at 14 cm, is made of single sided silicon pads
 277 with 600 μm × 6 mm pitch and the last one made by two layes is placed at 2.8 cm and 8 cm
 278 fabricated with ULTIMATE2 (also known as MIMOSA-28), a successor of MIMOSA-26
 279 sensor, with pitch 20.7 μm and thinned down to 50 μm. An area of 0.16 m² are covered
 280 by 400 MAPS sensor, corresponding to 356 millions of pixels divided into array size of 928
 281 × 960. Each pixel includes circuitry for readout, amplification, and Correlated Double
 282 Sampling (CDS) for signal extraction and noise subtraction and the frame integration time
 283 is 185.6 μs; after the subtraction the signal to noise ratio is ∼ 30, with a noise between
 284 10-12 electrons and a signal of 1000 e⁻. Thanks to the HFT system and the PXL, STAR
 285 achieved a track pointing resolution of 46 μm for 750 MeV/c kaons, and better than 30 μm
 286 for particle momenta bigger than 1 GeV/c: this performance enabled the study of D-meson
 287 production with a high significance signal.

288 ALPIDE at ALICE

289 The ALICE (A Large Ion Collider Experiment) tracking detector consists of the Inner
 290 Tracking System (ITS), the gaseous Time Projection Chamber (TPC) and the Transition
 291 Radiation Detector (TRD), all embedded in a magnetic field of 0.5 T. The ITS is made

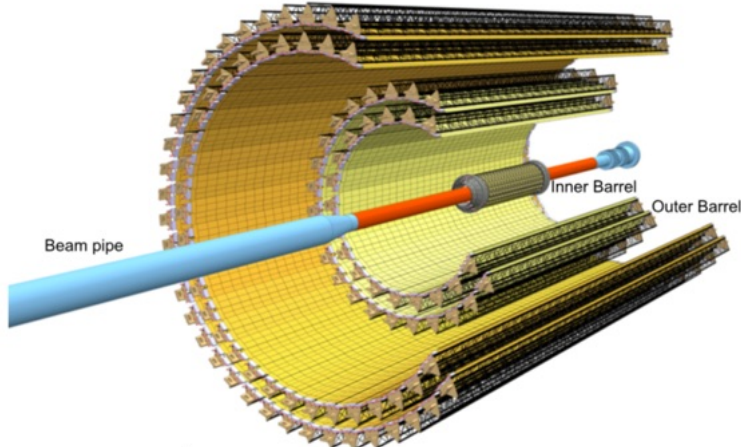


Figure 1.3

292 by six layers of detectors, two for each type, from the interaction point outwards: Silicon
 293 Pixel Detector (SPD), Silicon Drift Detector (SDD) and Silicon Strip Detector (SSD).
 294 Contrary to the others LHC experiments, ALICE tracker is placed in a quite different
 295 environments, which enables the usage of a MAPS-based detector: the expected dose
 296 assorbed by the tracker is expected to be smaller by two order of magnitude and the rate
 297 of interactions is few MHz instead of 40 MHz, even though the number of particles coming
 298 out from each interaction is very high (the SPD is invested by a density of particles of
 299 $\sim 100 \text{ cm}^{-2}$). The reconstruction of very complicated events with a large number of particle
 300 is then a challenge, hence to segment and to minimize the amount of material, which may
 301 cause secondary interaction futher complicating the event topology, is considered a viable
 302 strategy.

303 ITS2, upgraded during the LHC long shut down in 2019-20, was the first large-area
 304 ($\sim 10 \text{ m}^2$ covered by 2.5 Gpixels) silicon vertex detector based on CMOS MAPS. The
 305 detector employs the ALPIDE chip, developed by ALICE collaboration, fabricated in the
 306 180 nm CMOS Imaging Sensor process of TowerJazz, whose design takes full advantage
 307 of process feature which allows full circuitry within the pixel matrix. Thanks to the
 308 reduction in the material budget, ITS2 obtained an amazing improvement both in the
 309 position measurement and in the momentum resolution, especially improving the efficiency
 310 of track reconstruction for particle with very low transverse momentum (by a factor 6 at p_T
 311 $\sim 0.1 \text{ GeV}/c$). Further advancements in CMOS MAPS technology are being aggressively
 312 pursued for the ALICE ITS3 vertex detector upgrades (foreseen around 2026-27), with
 313 the goals of reducing the sensor thickness and improving the readout speed (which now is
 314 completely asynchronous) of the devices, while keeping power consumption at a minimum.

315 Beside tracking, ALICE has been studing the possibility of exploiting the extreme
 316 granularities of MAPS for calorimeter application. In a detector of this type, the energy
 317 measurement would come out from the counts of particles traversing the active layers,
 318 resulting then in a digital calorimeter. A prototype of such a calorimeter fabricated with
 319 the MIMOSA23 chips and containing 39 million pixels devided in 24 layers, alternated
 320 with 24 layers of tungsten, have been tested with electron beams and exhibited an en-
 321 ergy resolution better than standard hadronic calorimeters, with a stochastic terms of
 322 $30\%/\sqrt{E(\text{GeV})}$, a constant term of 2.8% and noise term of 0.063 GeV. Moreover, the

323 passive cooling via the tungsten structure has proven to be sufficient for the higher level of
 324 heat produced by the chip with respect the conventional sensor while keeping the structure
 325 compact.

326 BelleII

327 Due to the high background level coming from the nanobeam used at SuperKEKB in
 328 order to achieve a such high luminosity ($4.7 \times 10^{34} 1/\text{cm}^2/\text{s}$), silicon strip cannot be used
 329 in the inner layer of the tracker. The occupancy is too high to allow the usage of strips up
 330 to 40 mm from the beam pipe. Moreover for a precise reconstruction of B-decay vertices,
 331 the usage of thin detector is mandatory at the low energy (4 GeV to 7 GeV) of the beam,
 332 in order to minimize the multiple scattering of particles. The current vertex detector of

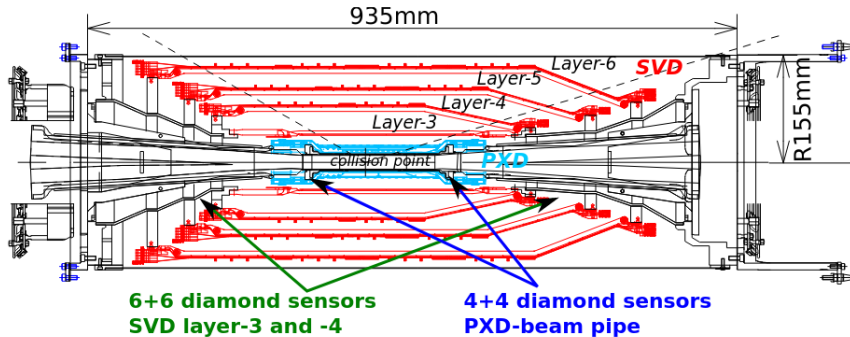


Figure 1.4: Belle2 vertex detector. Since an accidental beam background enhancement can damage the VXD, diamond detectors are installed in order to monitoring it.

332
 333 BelleII, VXD, is made of a pixel detector (PXD), fabricated with 2 layers of DEPFET-
 334 based pixels, and 4 layers of a double-sided silicon strip detectors (SVD)[5]. Due to the
 335 small capacitance of the collection node, DEPFET presents a high signal-to-noise ratio
 336 (in 30-50) thanks to the low intrinsic noise and to the large signal achieved with the fully
 337 depleted bulk: pixels are thinned to 75 μm in the active region, then a MIP is supposed
 338 to create a signal of $\sim 6000 \text{ e}^-$, while the typical noise of DEPFET is around 200 e^- . The
 339 ASIC read out is still based on a rolling shutter logic, with an integration time of 20 μs .
 340 In order to reduce the data-storage memory PXD hits are only used to improve spatial
 341 resolution of tracks: the SVD informations are used by the High Level Trigger (HLT) to
 342 look for regions of interest in the pixel ladders just by extrapolating back the tracks found
 343 in the tracker detector, and this method allows to store only data belonging to these areas;
 344 the PXD hits are then used in offline track fit to improve the vertex resolution.

345 MAPS have been proposed for the replacement of VXD during the Long Shut Down
 346 2 (LS2) foreseen around 2026-27; the new vertex detector, VTX, should be made of 5
 347 layers fabricated with the optimized Belle II pixel sensor (OBELIX), a detector based on
 348 TJ-Monopix (see at chapter 3). The main advantages VTX should bring are a significant
 349 improvement in the track and vertex resolution (14 μm before upgrade, $\lesssim 10 \mu\text{m}$ expected
 350 after upgrade), a reduction in the material budget, a higher background tolerance because
 351 of the smaller sensor than strips dimension.

352 1.2 Other applications

353 Pixel detectors are widely used also for photon detection: they can be used as single photon
354 counter or integrating and collecting the charge released by more impinging particles. The
355 utilisation in the first case is similar to the tracking one, except that the requirements are
356 less tight, so much that two noteworthy of microchips originally meant for detectors in
357 particle physics at the LHC, and later employed in other fields are Medipix and Timepix.
358 They are read-out chips developed by the Medipix Collaborations since early 1990s. For
359 two decades, different Medipix generations have been produced, having a rough correlation
360 with the feature size used: Medipix2 (1999) used 250 nm feature size CMOS while Medipix3
361 (2005) 130 nm. For photons imaging other materials with higher atomic charge than silicon
362 could be preferred, as a high photon absorption efficiency is needed: it was for this reason
363 that Medipix2 was bump bonded to identically segmented sensors of both silicon and
364 GaAs.

365 The applications in scientific imaging vary from astrophysics and medical imaging and
366 dosimetry to more exotic domains as studies of protein dynamics, material science, art
367 authentication and archaeology. One of the most important employment of Medipix is as
368 X-ray single photon counting in industrial and medical radiography and in 3D computed
369 tomography². Thanks to a New-Zealand company, the MARS Bioimaging detector has
370 been fabricated, which is capable of resolving the photons energy and produce 3D coloured
371 images. Besides tracking in HEP (I have already cited the use of Timepix3 is in the beam
372 telescope of the LHCb VELO), an important use of Timepix is in dosimetry. [Timepix](#)
373 [Detector for Imaging in Ion Beam Radiotherapy- articolo e qualche info](#). A small-Timepix
374 detector with the dimension of a USB can also be found at the International Space Station,
375 where it is exploited for radiation, principally made of heavy-ion, monitoring.

376 1.2.1 Applicability to FLASH radiotherapy

377 A possible new application of pixels detector is dosimetry or beam monitoring of charged
378 particles in high intensity radiography. Recently³ a promising method for RT at ultra high
379 dose rate (at least 40 Gy/s) and for this reason called FLASH-RT[9], instead of CONV-RT
380 (0.03 Gy/s), came out. However, finding dosimeters suitable at ultra high dose rate is still
381 an open issue since almost all standard online dosimeters have shown saturation problems.

382 Radiotherapy

383 The radiological treatment is a common method used in 60% of tumors both as palliative
384 care and as treatment. It can be given before, after or during a surgery, (Intra-operative
385 radiation therapy-IORT) and many different types of radiations (photons, electrons,
386 protons and ions, which mainly are hydrogen and carbon) can be used to irradiate the
387 affected tissues. Exploiting the ionizing energy loss, that can be parametrized by the
388 Linear Energy Transfer (LET), a biological damage can be delivered to the tissue: while α
389 and β particles are high LET radiations with values in 100 keV/ μ m to 200 keV/ μ m, x-rays
390 and gamma-rays are low LET radiations with values in range 0.2 keV/ μ m to 2 keV/ μ m. If

²The analysis of the direction dependence of X-ray absorption is performed, for example, in order to obtain an image in Computed Tomography (CT)

³The first evidences have been observed on mice experiments in 1966 and in 2014 by the group of Favaudon and Vozenin. After this, many tests on cats and pigs have been performed, and also there has been a clinical trial on a cutaneous tumor-patient

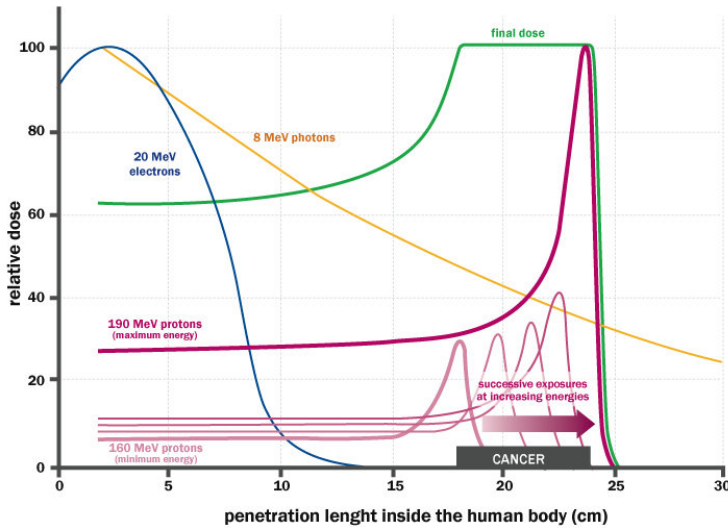


Figure 1.5: The Spread Out Bragg Peak (SOBP) curve (green), which is a constant dose distribution, is obtained from the superposition of many Bragg peak of hadrons with different energy.

	CONV-RT	FLASH-RT
Dose rate	0.03 Gy/s	40 Gy/s
Intra pulse dose rate	100 Gy/s	106 Gy/s
Treatment duration	~minutes	\lesssim 500 ms
Dose Per Pulse	0.3 mGy	1 Gy to 10 Gy
Pulse width	3 μ s	\sim 2 μ s

Table 1.1: Typical value of treatment parameters

391 x-ray photons, with energy in 4 MeV to 25 MeV are used, the ionization is caused by the
 392 Compton electrons and is more in the superficial layers of the tissue due to the exponential
 393 attenuation of the beam. The hardrons energy loss, instead, is strongly localized in
 394 the last region of the track, that is the Bragg peak, such as the the treatement typically
 395 requires the scanning of the target. The Relative Biological Effectiveness (RBE) of ions
 396 near th Bragg peak depends on their mass, and in particular it increases with the ion's
 397 mass; even though, too heavy ions generally increases the damage produced also in the
 398 entrance region. Carbon is considered the optimum between the two trends.

399 Electrons, instead, of energy in range of a dozen of MeV tend to spread out on a
 400 bigger region of a few centimeters in both the diameter and thickness. Using Very High
 401 Energy Electrons (VHEE) has been taken into account for irradiation of deeper tissues,
 402 however, to date, the FLASH effect has been tested and demostrated only using low-energy
 403 electrons.

404 **FLASH effect**

405 This treatment takes advantages of biological differences between tumors and healthy
 406 tissues: it is characterized by reducing normal tissue toxicity and maintaining equivalent

407 tumor damage. The response to dose can be described by the survival fraction probability,
 408 describing the fraction of surviving cell as a function of the dose:

$$S(D) = S(0) e^{-(\alpha D + \beta D^2)} \quad (1.1)$$

409 where α and β respectively represents the rate of cell killing by single ionizing events and
 410 by double hits. Hence, at high doses the density of damages increases and the cells repair
 411 becomes more difficult. Even if the FLASH effect is not yet completely understood and
 412 the underlying mechanisms are not clear, it looks like there are two different recipes which
 413 are involved:

- 414 • **The dose rate:** higher dose rate produce bigger damages (fig. 1.6(a)) since this
 415 prevent cells from sparing.
- 416 • **The presence or absence of oxygen:** while hypoxic cells are very resistant to radi-
 417 ation, normal oxygenated cells are highly radiosensitive. This is because if molecules
 418 containing O_2 break due to the impinging radiation, then the oxygen can build Re-
 419 active Oxygen Species (ROS) (fig.1.6(b))

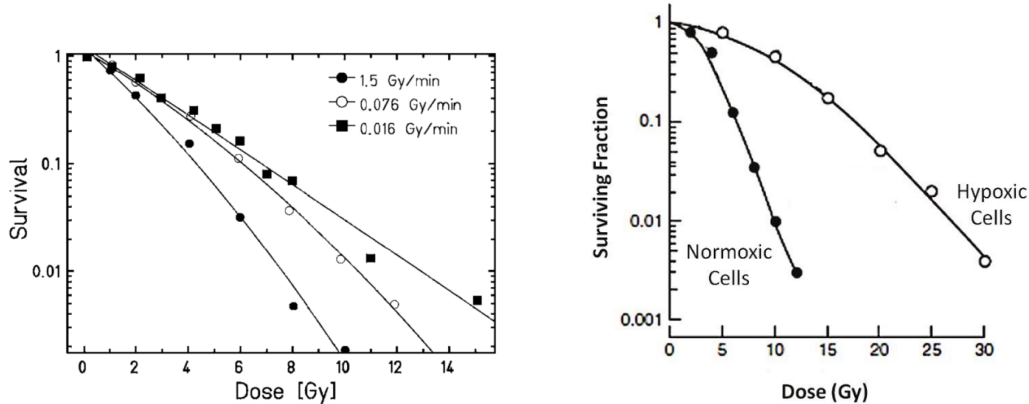


Figure 1.6: (a) Survival curve for different dose rate and (b) for different oxygen cell content

420 The Tumor Control Probability (TCP) and the Normal Tissue Complication (NTC) func-
 421 tions parametrize respectively the efficiency of damaging on the tumor after having released
 422 a certain dose and the probability of not affecting the healthy tissues. The intermediate
 423 zone between the increase of the TC and of the NTC is called therapeutic window, and
 424 the wider it is and the more effective the treatment is.

425 Dosimetric problems

426 Up to now, all online dosimeters have shown saturation problems at high Dose Per Pulse,
 427 differently from radiochromic films, which are the standard passive dosimeters and have
 428 shown a dose-rate independence up to 100 Gy/s. In spite of the linear response in wide
 429 dynamic range, they do not provide any online dosimetric informations, since the time
 430 required to extract the physical value from the reading is not long, requiring a measurement
 431 of the film density⁴.

⁴The radiation produces a polymerization of an active layer, resulting in a different density of coloration.

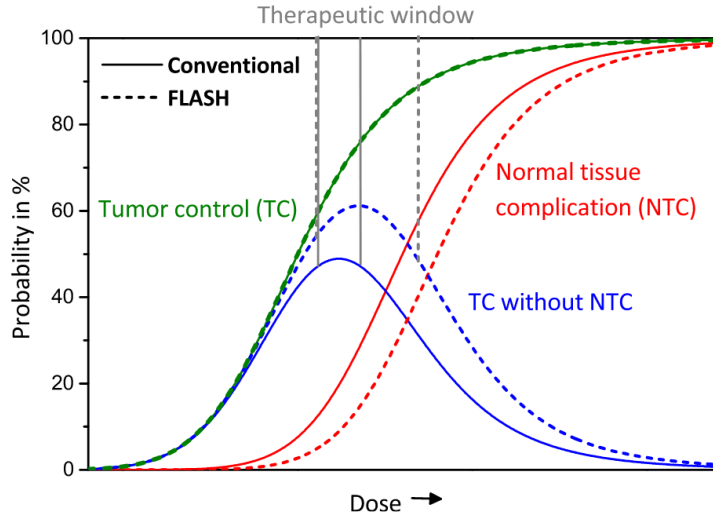


Figure 1.7: Illustration of dependence of TCP, NTCP and therapeutic window on dose, for CONV-RT ad FLASH-RT.

432 Ionization Chambers (ICs), which are the online reference dosimeter also according
 433 to law protocols, at high level of radiation (already at dose per pulse two orders of mag-
 434 nitude lower than the ones used for FLASH-RT) show both problems of saturation and
 435 recombination. When a high density of ions and electrons is produced in the gas, a high
 436 counter electric field opposed to the drift one might be generated; if a neutral region build
 437 up, both the recombination of i/e pairs, with a subsequent photoemission and abrupt dis-
 438 charge can happen. A correction factors, k_{sat} , can be introduced for sufficient low level of
 439 radiation and in this case a precise dose measurement can still be done: under conventional
 440 operation, with Dose Per Pulse lower than 1 mGy the correction factor is <5%.

441 Concerning the conventional semiconductor, if exposed to high dose rate, they suffer of
 442 saturation problems just as the ICs, but the development of fast MAPS devices, with rate
 443 capability of $100\text{ MHz}/\text{cm}^2$ or more, might open the possibility of using these detectors as
 444 dosimeters at high dose rates. The idea is to use the high readout speed to split the dose
 445 per pulse in many buckets to reduce the saturation effect. Indeed a thin planar sensor
 446 could allow for the preservation of an enough strong electric field even at high dose rate
 447 which, together with the short mean path the e/h must cover to get the electrode (the
 448 epitaxial layer typically is $\sim 30\text{ }\mu\text{m}$), could result in a fast collection of electrons by drift
 449 and in a non-saturated response. Besides the thinness, also the small capacity typical of
 450 MAPS is beneficial for reducing the readout time: a reduced C_d enables for a fast discharge
 451 and then for a fast readout. Finally, MAPS devices would provide good time and space
 452 resolutions compared to other dosimeter technologies, and since they can be thinned down
 453 to about $50\text{ }\mu\text{m}$, could also be employed in monitoring the beam position with minimal
 454 disturbance.

455 Among other detectors, optical fiber and alanine dosimeters have been proposed for
 456 high dose environments and many groups are going on studies on their applicability on
 457 FLASH-RT. In reference [10] are presented some results related with saturation problems
 458 at high DDP of different types of detectors. The dosimeters tested and their value at
 459 which saturation becomes are reported in table 1.2, while in figure 1.8 are reported the
 460 measurements. The DrR is then defined as the ratio between the signal response of each

Commercial detector	Detector type	saturation [Gy/p]
PTW TW34045 Advanced Markus EC	ionization chamber	0.3
PTW TM60017 Dosimetry Diode E	silicon diode	0.15
PTW TW60019 microDiamond	diamond	0.15
DoseVue DoseWireTM Series 100	scintillator fiber	11-26

Table 1.2: Results obtain in [10]

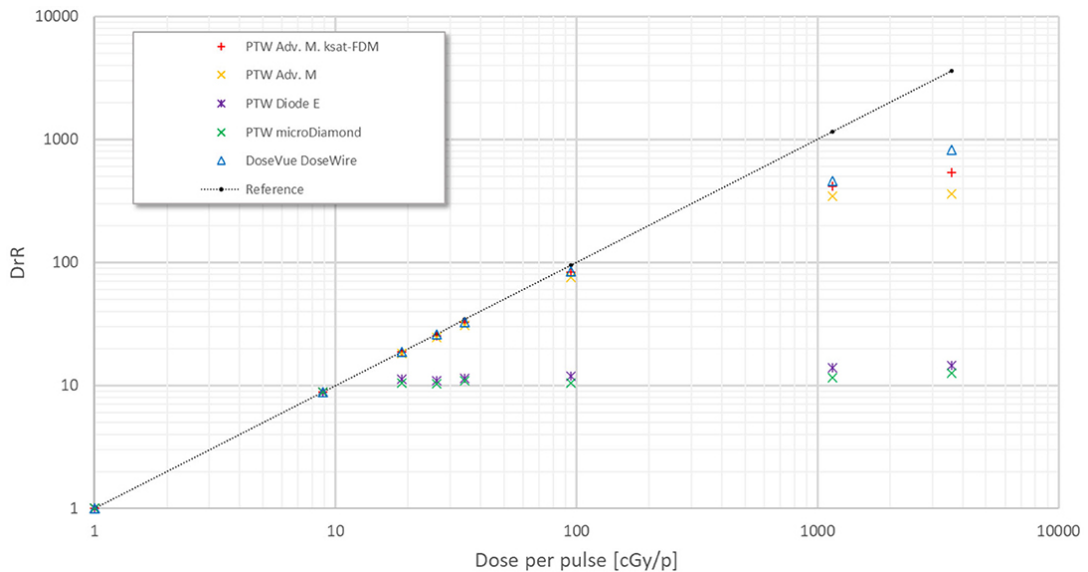


Figure 1.8: Saturation problems underlyed in [10].

⁴⁶¹ dosimeters at a fixed DDP of 1 cGy/p and is called dosimeter reading ratio (DrR):

$$DrR = \frac{R}{R|_{Dp=1cGy/p}} = \frac{R}{R_{ref}} \quad (1.2)$$

⁴⁶² Then, for a saturation not affected by saturation problems DrR should be a straight line
⁴⁶³ with a slope equal to 1; since the reference measurements of dose has been performed with
⁴⁶⁴ radiochromic films (GAFCHROMIC EBT-XD), whose dose independence has been tested⁵
⁴⁶⁵ in range from 0 Gy to 15 Gy, the dotted black line in figure 1.8 represents the reference
⁴⁶⁶ measurement done with it.

⁵The radiochromic films calibration has been obtained by irradiating the films with dose values in range from 0 Gy to 15 Gy, by positioning the films in a polymethylmethacrylate (PMMA) phantom at R₁₀₀ depth, corresponding to 10 cm

467 **Chapter 2**

468 **Pixel detectors**

469 Pixel detectors are semiconductor detectors which are segmented in two dimensions: this
470 distinguish them from the strip detectors, such that a single plane of detector already
471 provides both the coordinates of impact of the detected particle. Their operation is based
472 on the p-n junction (fig. 2.1). A p-n junction is built by bringing in contact two n
473 and p doped silicon crystals. At the boundary, recombination of both charge carriers
474 occurs forming a region, the depletion zone, which is free of charge carriers. The charged
475 donors⁺ and acceptor⁻, that remain ionised in the n-type and p-type regions, features a
476 space charge and create an electric field across the junction, causing a drift current in the
477 opposite direction to the diffusion one, through which the junction reaches an equilibrium
478 state. Assuming a constant space change, the electric field is linear and reach a maximum
479 at the boundary of the *p* and *n* layers.

480 **2.1 Signal formation**

481 When a charged particle passes through a pixel and loses energy by ionization only a
482 part of that energy is used to generate electron-hole pairs, since another part is used for
483 other processes, as lattice excitation. The average energy needed to create a pair at 300 K
484 in silicon is $w_i = 3.65 \text{ eV}$, that is more than the mean ionization energy because of the
485 interactions with phonon, since for a minimum ionizing particle (MIP) the most probable
486 value (MPV) of charge released in the semiconductor is $0.28 \text{ keV}/\mu\text{m}$, hence the number
487 of electrons-vacuum pairs is:

$$\langle \frac{dE}{dx} \rangle \frac{1}{w_i} \sim 80 \text{ e/h} \sim \frac{1.28 \cdot 10^{-2} fC}{\mu\text{m}} \quad (2.1)$$

488 Because of the splitting of the energy depositon between the two different processes, the
489 number $N_{e/h}$ of couples generated undergoes fluctuations that usually follow a Poisson
490 distribution; thus the fluctuations of $N_{e/h}$ is equal to $\sigma_{e/h} = \sqrt{N_{e/h}}$. Under the constraint
491 of complete absorption of a particle, the energy resolution improves of a factor \sqrt{F} , where
492 F is called the Fano factor and determines the ultimate limit of energy resolution for
493 semiconductors. F is a function of the material and temperature and for silicon is equal
494 to ~ 0.115 .

495 In order to avoid a loss signal, it is fundamental that pairs e/h are produced in the
496 depleted region of the semiconductor, where the probability of recombination with charge
497 carriers is low. For this reason pixel detectors are commonly reverse biased: a positive
498 bias is given to the *n* electrode and a negative to the *p* in order to grow the depletion zone

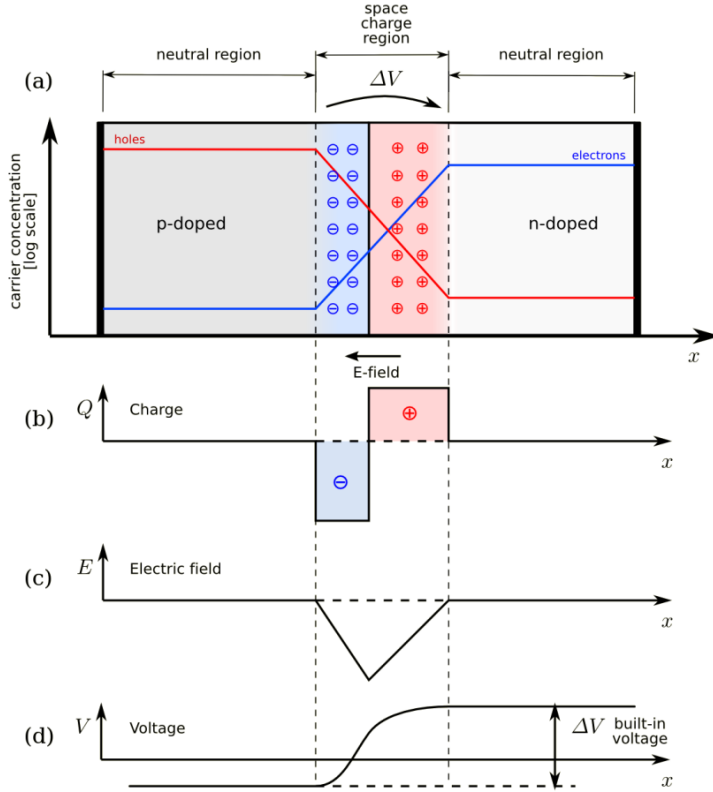


Figure 2.1: The structure of a p-n junction. (a) structure, (b) space charge density, (c) electric field distribution and (d) potential distribution.

in the epitaxial layer within the bulk. The width of the depletion region depends on the external bias V_{ext} , the resistivity ρ and also with the dopant:

$$d_n \sim 0.55 \sqrt{\frac{\rho}{\Omega cm} \frac{V_{ext}}{V}} \mu m \quad d_p \sim 0.32 \sqrt{\frac{\rho}{\Omega cm} \frac{V_{ext}}{V}} \mu m \quad (2.2)$$

Thus, high resistivity wafers ($100 \Omega cm - k\Omega cm$) are typically preferred because they allow bigger depletion zone with smaller voltage bias.

The charges created within the sensor are separated by an electric field and collected at their respective electrodes (p for holes and n for electrons)¹; by the drift of these charges, a signal i_e is generated on the electrode e as stated by the Shockley-Ramo's theorem:

$$i_e(t) = -q v(t) E_{WF,e} \quad (2.3)$$

where $v(t)$ is the instantaneous velocity of the charge q and E_{WF} is the weighting field, that is the field obtained biasing the electrode e with 1V and all the others with 0V. The drift velocity of the charge depends on the electric field and on the mobility of the particle:

$$v = \mu(E) E \quad (2.4)$$

where $\mu(E)$ is a function of the electric field and is linear in E only for small E : at higher values the probability of interactions with optical phonons increases, the mobility drops

¹Even if in principle both the electrode can be used to read the signal, for pixel detectors, where the number of channel and the complexity of readout are high, only one is actually used. In strip and pad detectors, instead, is more common a dual-side readout

511 and this leads to a saturation of the velocity (fig. 2.2). Typical values for electrons and
512 holes mobility in silicon at room temperature are $\mu_n \sim 1450 \text{ cm}^2/\text{Vs}$, $\mu_h = 500$.

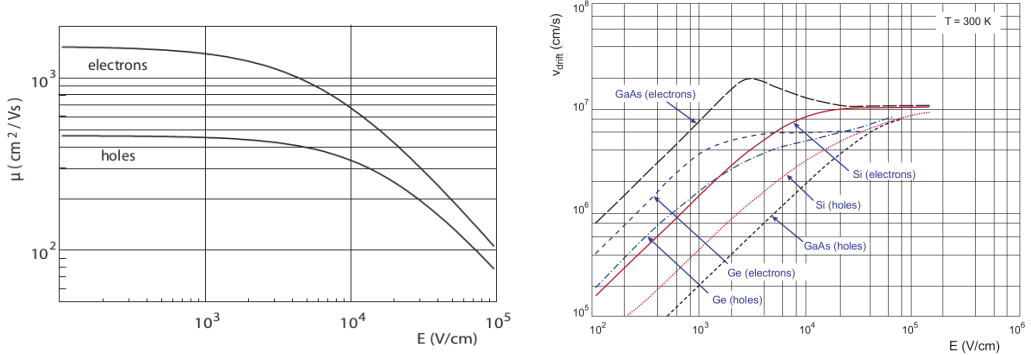


Figure 2.2: (a) Dependence of the mobility on the electric field. (b) Drift velocity at room temperature in different semiconductors

513 2.2 Charge Coupled Devices

514 In CCDs the charge is created in a very thin active epitaxial layer (typically 10 μm ,
515 maximally about 30 μm) and then locally stored in a potential minimum which is created
516 by a MOS structure. The size of the CCD cells is typically in the range 10 μm to 20 μm
517 such that spatial resolutions are of the order of a few micrometres. The collected charges
518 are moved stepwise from electrode to electrode (thus so called 'bucket chain') by applying a
519 potential with a clock with frequency of \sim MHz; despite of such high frequency, the readout
520 chain is completely sequential and this makes the entire process comparatively slow (tens
521 of ms). A particular type of CCD, the pnCCDs, are typically used to detect low energy
522 (< 10 keV) x-ray photons for their homogeneous spatial detection efficiency of photons.
523 The pnCCDs have a sideward depletion similar to silicon drift chambers that makes the
524 electric field stronger, compared with the normal CCDs. The pnCCDs designed for photon
525 imaging are often fabricated with high Z materials, to increase absorption efficacy.

526 2.3 Hybrid pixels

527 Hybrid pixels, which currently are the state-of-art technology for large scale pixel detectors
528 in most particle physics experiments, are made of two parts welded together through
529 microconnection (bump bond): the sensor and the electronics (fig. 2.3a). They provide a
530 practical system where the sensor and the ASIC (application specific integrated circuit)
531 can be optimized separately, which makes them really fast, capable of handling with rate
532 up to GHz. However a disadvantage of hybrid pixels is that they must be connected before
533 testing. For reasons related with the historical development, the n⁺-in-n sensors were the
534 first to be used; they demanded double-sided processing which guarantees the detector
535 functionality both before and after the type inversion of the n⁻ doped bulk into p-type
536 after high quantity of radiation. The pn-diode is initially on the unstructured backside
537 of the sensor, while after, the depletion zone grows from the electrode side into the bulk.
538 This ensures that the signal can be sensed on the pixels even if the substrate is no longer
539 fully depleted, even though the bias voltage required for a sufficient depletion increases,

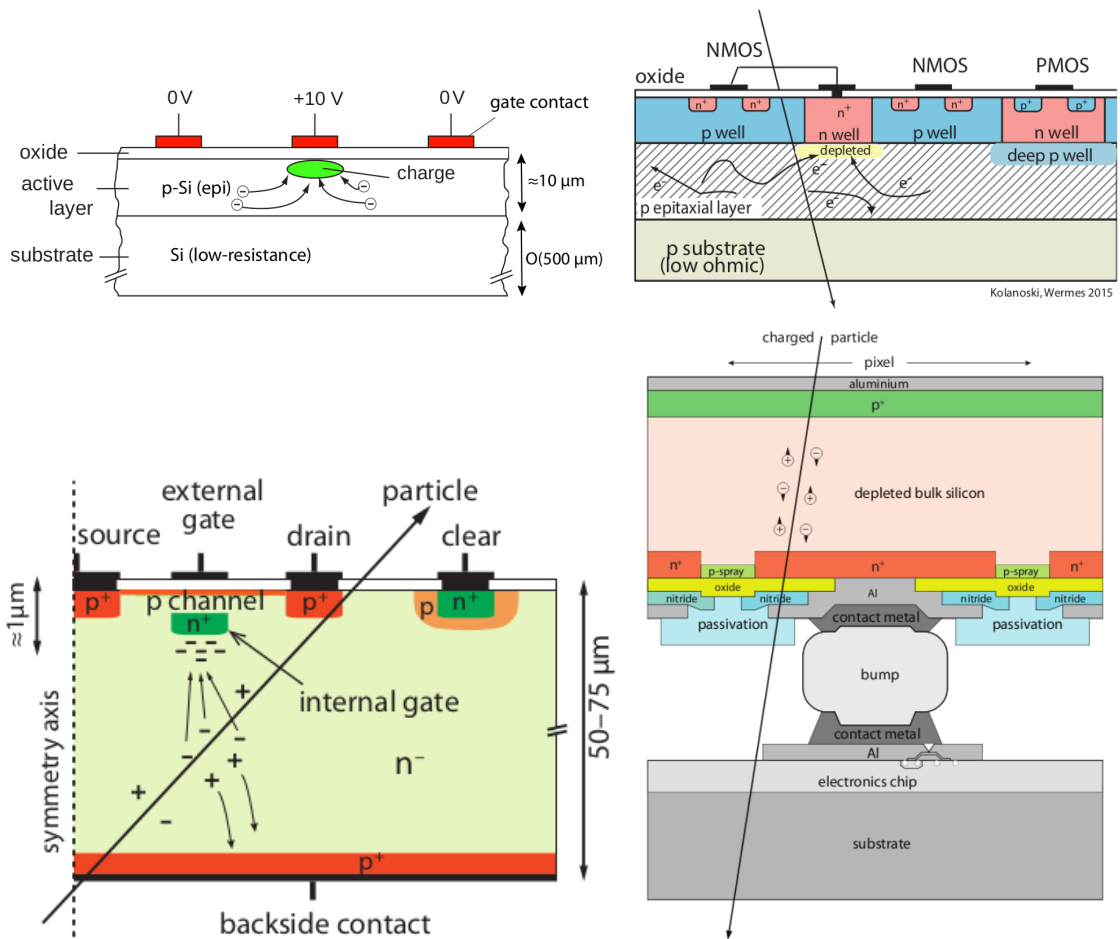


Figure 2.3: Concept cross-section of hybrid pixel (a) and of a DEPFET (b)

540 liming the detector lifetime up to a few years. With the availability of high quality p-
541 substrate material ($\gtrsim 2 \text{ k}\Omega\text{cm}$) the fabrication of n-in-p type sensors, which does not invert
542 anymore, became the preferred choise leading also a huge advance in cost reduction due
543 to no more need of double sided. However, the particular and sophisticated procedure to
544 bond sensor and ASIC makes them difficult to produce, delicate (especially when exposed
545 to high levels of radiation) and also expensive.

546 DEPFET are the first attempt towards the integration of the front end (FE) on the
547 sensor bulk: they are typically mounted on a hybrid structure but the sensor also in-
548 tegrates the first amplification stage. Each pixel implements a MOSFET (metal-oxide-
549 semiconductor field-effect transistor) transistor (a p-channel in fig. 2.3b): a hole current
550 flows from source to drain which is controlled by the external gate and the internal gate
551 together. The internal gate is made by a deep $n+$ implant towards which electrons drift
552 after being created in the depletion region; the accumulation of electrons in the region
553 underneath the n implant changes the gate potential and controls the transistor current;
554 the removal of the signal charge from the internal gate is called "Clear". DEPFET typ-
555 ically have a good S/N ratio: this is principally due to the amplification on-pixel, which
556 guarantees any charge losses, and to the large depletion region. They can be operated in-
557 dividually or integrated in the readout nodes of other detectors, as for example silicon drift
558 chambers, but they always need to be connected to an ASIC with a readout circuit on it.
559 In recent years, the sensor development was driven by an intensive R&D and prototyping
560 for x-ray imagers and the ILC vertex detector.

561 2.4 CMOS MAPS and DMPAS

562 Monolithic active pixels accommodate on the same wafer both the sensor and the FE
563 electronics, with the second one implanted on top within a depth of about $1 \mu\text{m}$ below
564 the surface. MAPS have been first proposed and realized in the 1990s and their practical
565 usage has been enabled by the development of the electronic sector, which guarantees the
566 halving of CMOS transistors dimension at least every two years, as stated by the Moore's
567 law. As a matter of fact the dimension of components, their organization on the pixel
568 area and logic density are important issues for the design and for the layout. Compared
569 to CCDs, the readout time is dramatically reduced by the in-pixel amplification and
570 discrimination, typically followed by a sparsified readout not requiring the signal to be
571 transported anymore over thousands of pixels; as aside effect, the radiation tolerance is
572 also greatly increased by sensing the signal charge directly within its own pixel.

573 A critical parameter for accelerator experiments is the material budget, which repre-
574 sents the main limit factor for momentum measurement resolution in a magnetic field;
575 since hybrid pixels are thicker (\sim hundreds of μm) than monolithic ones (even less than
576 $100 \mu\text{m}$). Using the latter the material budget can be down by a third: typical values for
577 hybrid pixels is $1.5 \% X_0$ per layer, while for monolithic $0.5 \% X_0$. Compared to MAPS,
578 among other disadvantages of hybrid pixels there is the bigger power consumption, that
579 requires also a bigger cooling system, leading to a futher increase of material.

580 Monolithic active pixel can be distinguished between two main categories: MAPS and
581 depleted MAPS (DMAPS). MAPS (figure a ??) have typically an epitaxial layer in a from
582 range $1 \mu\text{m}$ to $20 \mu\text{m}$ and, since they are not depleted, the charge is mainly collected by
583 diffusion rather than by drift. This makes the path of charges created in the bulk longer
584 than usual, making them slow (of order of 100 ns). Moreover, the collection can be partial,

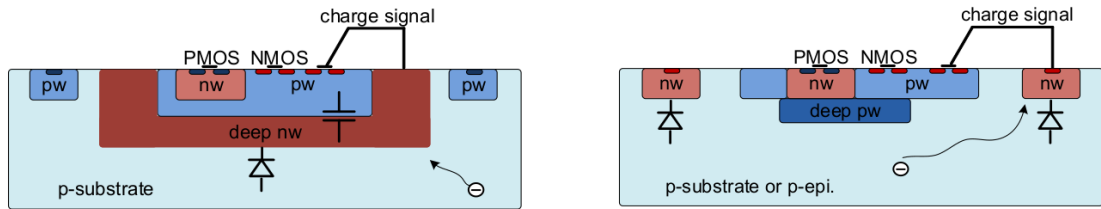


Figure 2.4: Concept cross-section with large and small fill factor

especially after irradiation of the detector (look at ?? for radiation damages), when the trapping probability becomes higher. In figure ?? it is shown as example of CMOS MAPS: the sensor implements an n well as collection diode; to prevent the others n wells (which contain PMOS transistor) of the electronic circuit competing in charge collection and to shield the CMOS circuit from the substrate, additional underlying deep p well are needed. DMAPS are instead MAPS depleted with d typically in $\sim 25 \mu\text{m}$ to $150 \mu\text{m}$ (eq. 2.2) which extends from the diode to the deep p-well, and sometimes also to the backside (in this case if one wants to collect the signal also on this electrode, additional process must be done).

2.4.1 DMAPS: large and small fill factor

There are two different sensor-design approaches (figure 2.4) to DMAPS:

- large fill factor: a large collection electrode that is a large deep n-well and that host the embedded electronics
- small fill factor: a small n-well is used as charge collection node

To implement a uniform and stronger electric field, DMAPS often uses large electrode design that requires multiple wells (typically four including deep n and p wells); with this layout the total capacity of the sensor increases because of the addition of a new term (fig. 2.5), which contributes to the total amplifier input capacity ($\sim 100 \text{ fF}$). In addition to the capacity between pixels (C_{pp}) and between the pixel and the backside (C_b), a non-negligible contribution comes from the capacities between wells (C_{SW} and C_{WW}) needed to shield the embedded electronics. These capacities affect the thermal and 1/f noise of the charge amplifier and the τ_{CSA} too:

$$ENC_{thermal}^2 \propto \frac{4}{3} \frac{kT}{g_m} \frac{C_D^2}{\tau_{sh}} \quad \tau_{CSA} \propto \frac{1}{g_m} \frac{C_D}{C_f} \quad (2.5)$$

where g_m is the transconductance, τ_{sh} is the shaping time. Among the disadvantages coming from this large input capacity there is a coupling between the sensor and the electronics resulting in cross talk noise on neighbouring electrodes; indeed, since digital switching in the FE electronics does a lot of oscillations, this problem is especially connected with the intra wells capacities. So, larger charge collection electrode sensors provide a uniform electric field in the bulk that results in short drift path and so in good collection properties, especially after irradiation, when trapping probability can become an issue.

The small fill-factor variant, instead, benefits from a small capacity (5 fF to 20 fF), but suffers from a non uniform electric field and from all the issue related to that (slowness and high trapping probability). As we'll see these two different types of sensor require

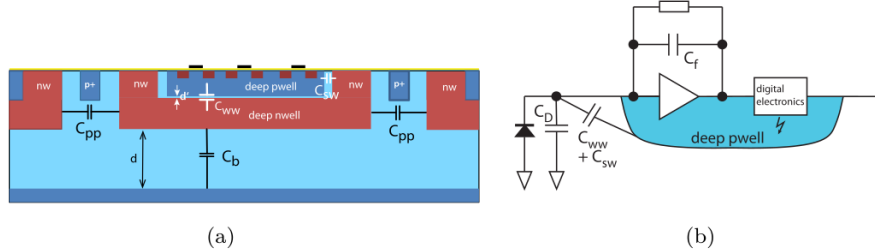


Figure 2.5: C_{pp} , C_b , C_{WW} , C_{SW}

	small fill factor	large fill factor
small sensor C	✓ (< 5 fF)	✗ (~ 100 200 fF)
low noise	✓	✗
low cross talk	✓	✗
velocity performances	✓	✗ (~ 100 ns)
short drift paths	✗	✓
radiation hard	✗	✓

Table 2.1: Small and large fill factor DMAPS characteristics

617 different amplifier: the large electrode one is coupled with a charge sensitive amplifier,
618 while the small one with a voltage amplifier (sec 2.5.1).

619 2.4.2 A modified sensor

620 A process modification, developed by CERN in collaboration with the foundries, which
621 has become the standard solution to combine the characteristics of a small fill factor
622 sensor (small input amplifier capacity) and of a large fill factor sensor (uniform electric
623 field), is the one carried out for ALICE upgrade about ten years [1]. A compromise
624 between the two sensors could also be making smaller pixels, but this solution requires
625 reducing the electronic circuit area, so a completely new pixel layout should be though.
626 The modification consists in inserting a low dose implant under the electrode and one of
627 its advantage lies in its versatility: in fact, both standard and modified sensor are often
628 produced for testing.

629 Before the process modification, the depletion region extends below the diode towards
630 the substrate, and it does not extend much laterally, even if a high bias is applied to the
631 sensor (fig. 2.6). After the modification, two distinct pn junctions are built: one between
632 the deep p well and the n⁻ layer, and the other between the n⁻ and the p⁻ epitaxial
633 layer, extending to the whole area of the sensor. Since deep p well and the p-substrate are
634 separated by the depletion region, the two p electrodes can be biased separately² and this
635 is beneficial to enhance the vertical electric field component. The doping concentration is
636 a trimmer parameter: it must be high enough to be greater than in the epitaxial layer in
637 order to prevent the punchthrough between p-well and the substrate, but it must also be
638 low enough to allow the depletion for reasonable bias values.

²This is true in general, but it can be denied if other doping characteristics are implemented, and we will see that this is the case of TJ-Monopix1

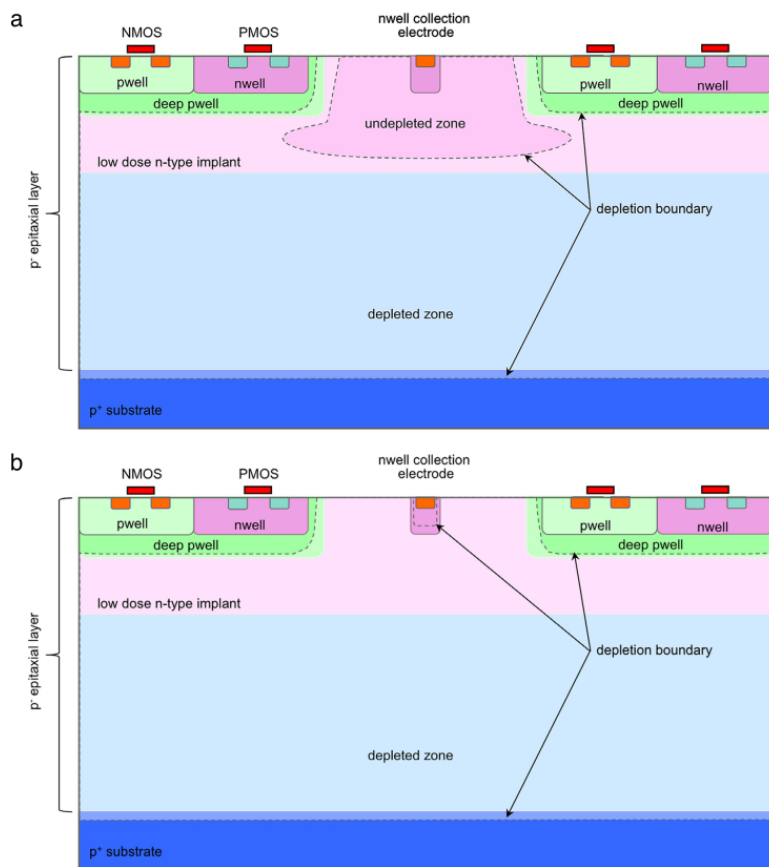


Figure 2.6: A modified process for ALICE tracker detector: a low dose n implant is used to create a planar junction. In (a) the depletion is partial, while in (b) the pixel is fully depleted.

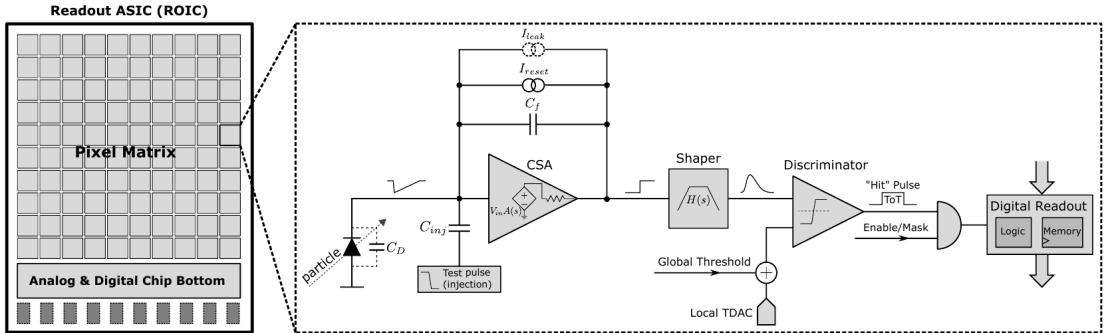


Figure 2.7: Readout FE scheme: in this example the preamplifier is a charge sensitive one (CSA) but changing the capacitive feedback into a resistive one, this can be converted in a voltage or current amplifier.

639 2.5 Analog front end

640 After the creation of a signal on the electrode, the signal enters the front end circuit
 641 (fig.2.7), ready to be molded and transmitted out of chip. Low noise amplification, fast
 642 hit discrimination and an efficient, high-speed readout architecture, consuming as low
 643 power as possible, are the goal of the readout integrated electronics (ROIC). The main
 644 parts of the analog front end chain are a preamplifier (that often is the only amplification
 645 stage) with a reset to the baseline mechanism and a leakage current compensation, a shaper
 646 (a band-pass filter) and finally a discriminator. The whole chain must be optimized and
 647 tuned to improve the S/N ratio. It is very important both not to have a large noise
 648 before the amplification stage in order to not multiply that noise, and chose a reasonable
 649 threshold of the discriminator to cut noise-hits much as possible.

650 2.5.1 Preamplifier

651 Even if circuits on the silicon crystal are only constructed by CMOS, a preamplifier can
 652 be processed as an operational amplifier (OpAmp) where the gain is determined by the
 653 input and feedback impedance (first step in figure 2.7):

$$G = \frac{v_{out}}{v_{in}} = \frac{Z_f}{Z_{in}} \quad (2.6)$$

654 Depending on whether a capacity or a resistance is used as feedback, respectively a
 655 charge or a voltage amplifier is used: if the voltage input signal is large enough and has
 656 a sharp rise time, the voltage sensitive preamplifier is preferred. Consequently, this flavor
 657 doesn't suit to large fill factor MAPS whose signal is already high enough: $v_{in} = Q/C_D \approx 3\text{ fC}/100\text{ pF} = 0.03\text{ mV}$, but it's fine for the small fill factor ones: $v_{in} = Q/C_D \approx 3\text{ fC}/3\text{ pF} = 1\text{ mV}$.

660 In the case of a resistor feedback, if the signal duration is longer than the discharge
 661 time ($\tau = R_S C_D$) of the detector the system works as current amplifier, as the signal
 662 is immediately transmitted to the amplifier; in the complementary case (signal duration
 663 longer than the discharge time) the system integrates the current on the C_D and operates
 664 as a voltage amplifier.

665 2.6 Readout logic

666 The readout logic includes the part of the circuit which takes the FE output signal, pro-
 667 cesses it and then transmit it out of pixel and/or out of chip; depending on the situation
 668 of usage different readout characteristics must be provided. To store the analogical in-
 669 formation (i.e. charge collected, evolution of signal in time, ...) big buffers and a large
 670 bandwidth are needed; the problem that doesn't occur, or better occur only with really
 671 high rate, if one wants record only digital data (if one pixel is hit 1 is recorded, and if not
 672 0 is recorded).

673 A common compromise is to store the time over threshold (ToT) of the pulse in clock
 674 cycle counts; this needs of relatively coarse requirement as the ToT can be trimmed down
 675 to use only a dozen bits but, being correlated (and hopefully linear) with the deposited
 676 charge, it provides a sufficient information. The ToT digitalization usually takes advantage
 677 of the distribution of a clock (namely BCID, bunch crossing identification) on the pixels'
 678 matrix. The required timing precision is better than ~ 25 ns, that corresponds to the period
 679 between bunch collisions at LHC; for such reason a reasonable BCID-clock frequency for
 pixels detector is 40 MHz.

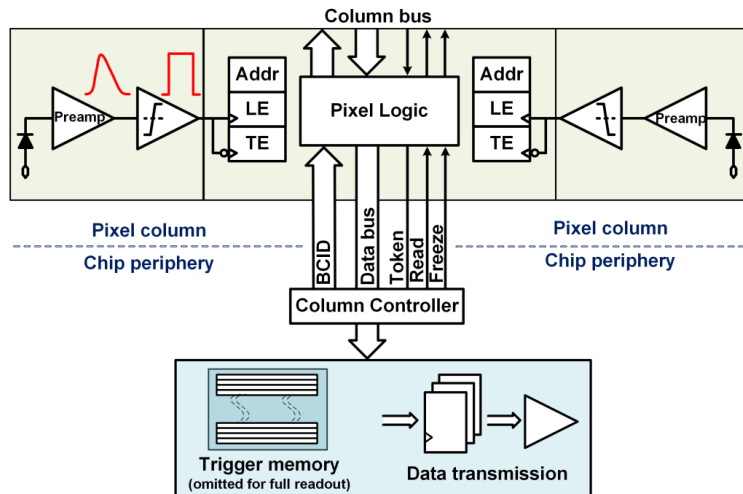


Figure 2.8: Column drain R/O scheme where ToT is saved

680
 681 Moreover, the readout architecture can be full, if every hit is read, or triggered, if a
 682 trigger system decides if the hit must be stored or not. On one hand the triggered-readout
 683 needs buffers and storage memories, on the other the full readout, because there is no
 684 need to store hit data on chip, needs an high enough bandwidth. A triggered readout is
 685 fundamental in accelerator experiments where the quantity of data to store is very large
 686 and some selection has to be applied by the trigger: to give an order of magnitude, at LHC
 687 more than 100 TBit/s of data are produced, but the storage limit is about 100 MBit/s
 688 [2](pag. 797). Typically, the trigger signal is processed in a few μs , so the pixel gets it
 689 only after a hundred clock cycles from the hit arrival time: the buffer depth must be able
 690 to handle such high trigger latency.

691 After having taken out the data from the pixel, it has to be transmitted to the end
 692 of column (EoC) where a serializer delivers it out of chip, typically to an FPGA. There
 693 are several ways of transmitting data from a pixel to the EoC: one of the most famous
 694 is the column-drain read out, developed for CMS and ATLAS experiments [3]. All the

695 pixels in a double-column share a data bus and only one pixel at a time, according to
 696 a priority chain, can be read. The reading order circuit is implemented by shift register
 697 (SR): when a hit arrives, the corresponding data, which can be made of timestamp and
 698 ToT, is temporarily stored on a RAM until the SR allows the access to memory by data
 699 bus. Even if many readout architectures are based on the column-drain one, it doesn't suit
 700 for large size matrices. The problem is the increasing number of pixels on a column would
 701 also raise the number of pixels in the priority chain, which would result in a slowdown of
 702 the readout.

703 If there isn't any storage memory, the double-column behaves as a single server queue
 704 and the probability for a pixel of waiting a time T greater than t , with an input hit rate
 705 on the column μ and an output bandwidth B_W is [4]:

$$P(T > t) = \frac{\mu}{B_W} e^{-(B_W - \mu)t} \quad (2.7)$$

706 To avoid hit loss (let's neglect the contribution to the inefficiency of the dead time τ due
 707 to the AFE), for example imposing $P_T > t \sim 0.001$, one obtains $(B_W - \mu) t_t \sim 6$, where
 708 t_t is the time needed to transfer the hit; since t_t is small, one must have $B_W \gg \mu$, that
 means a high bandwidth [4].

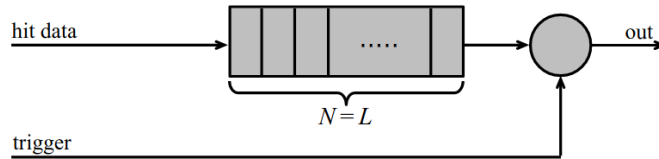


Figure 2.9: Block diagram of a pipeline buffer: N is the dimension of memory buffer and L is the trigger latency expressed in BCID cycles

709 Eq.2.7 is actually an approximation, since each pixel sees a different bandwidth de-
 710 pending on the position on the queue: the first one sees the full bandwidth, while the next
 711 sees a smaller one because it can be occasionally blocked by the previous pixel. Then,
 712 the bandwidth seen by the pixel i is $B_i = B - \sum_j \mu_j$, where μ_j is the hit rate of the j th
 713 pixel. The efficiency requirement on the bandwidth and the hit rate becomes: $B_{W,i} > \mu_i$,
 714 where the index i means that the constraint is for a single pixel; if all the N pixels on a
 715 column have the same rate $\mu = N\mu_i$, the condition reduces to $B_W > \mu$. The bandwidth
 716 must be chosen such that the mean time between hits of the last pixel in the readout chain
 717 is bigger than that. In order to reduce the bandwidth, a readout with zero suppression
 718 on pixel is typically employed; this means that only information from channels where the
 719 signal exceeds the discriminator threshold are stored.

721 If, instead, the signal is locally stored until a trigger signal arrives, the input rate to
 722 column bus μ' is reduced compared to the hit rate μ as: $\mu' = \mu \times r \times t$, where r is the
 723 trigger rate and t is the bunch crossing period. In this situation there is a more relaxed
 724 constraint on the bandwidth, but the limiting factor is the buffer depth: the amount of
 725 memory designed depends both on the expected rate μ and on the trigger latency t as
 726 $\propto \mu \times t$, which means that the higher the trigger latency the lower the hit rate to cope
 727 with.

728 In order to have an efficient usage of memory on pixels' area it's convenient grouping
 729 pixels into regions with shared storage. Let's compare two different situations: in the first
 730 one a buffer is located on each pixel area, while in the second one a core of four pixels

⁷³¹ share a common buffer (this architecture is commonly called FE-I4).

Consider a 50 kHz single pixel hits rate and a trigger latency of 5 μs , the probability of

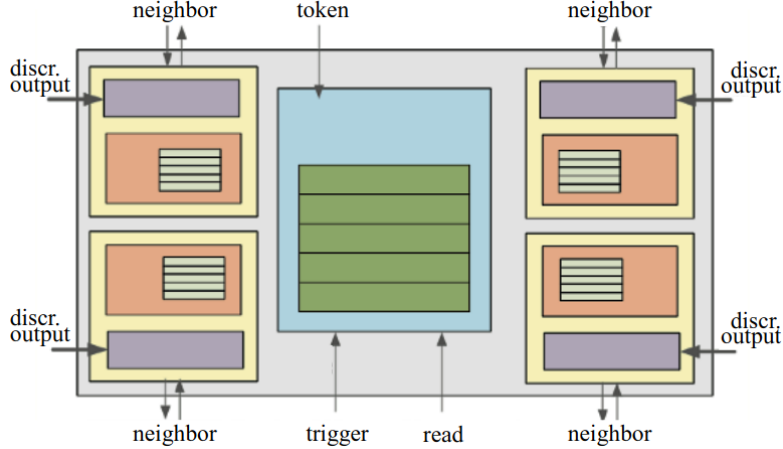


Figure 2.10: Block diagram of the FE-I4 R/O. Read and memory management section is highlighted in light blue; latency counters and trigger management section are highlighted in green; hit processing blocks are highlighted in purple; ToT counters and ToT management units are highlighted in orange

⁷³²

⁷³³ losing hits is:

$$P(N > 1|\nu) = 1 - P(N = 0|\nu) - P(N = 1|\nu) = 1 - e^{-\nu}(1 + \nu) \approx 2.6\% \quad (2.8)$$

⁷³⁴ where I have assumed a Poissonian distribution with mean $\nu = 0.25$ to describe the counts
⁷³⁵ N.

⁷³⁶ To get an efficiency ϵ greater than 99.9 % a 3 hit depth buffer is needed:

$$P(N > 3|\nu) = 1 - \sum_{i=0}^3 P(N = i|\nu) < 0.1\% \quad (2.9)$$

⁷³⁷ Consider the second situation: if the average single pixel rate is still 50 kHz, grouping four
⁷³⁸ pixels the mean number of hits per trigger latency is $\nu = 0.25 \times 4 = 1$. To get an efficiency
⁷³⁹ of 99.9% (eq. 2.9) a buffer depth of 5 hits in the four-pixels region, instead of 3 per pixels,
⁷⁴⁰ is needed.

⁷⁴¹ **Chapter 3**

⁷⁴² **MAPS devices description**

⁷⁴³ TJ-Monopix1 is a small electrode DMAPS with fast R/O capability, fabricated by Tow-
⁷⁴⁴ erJazz foundry in 180 nm CMOS imaging process. It is part, together with prototypes
⁷⁴⁵ from other series such as TJ-MALTA, of the ongoing R&D efforts aimed at developing
⁷⁴⁶ DMAPS in commercial CMOS processes, that could cope with the requirements at ac-
⁷⁴⁷ celerator experiments. Both TJ-Monopix and TJ-MALTA series [11], produced with the
⁷⁴⁸ same technology by TowerJazz (the timeline of the foundry products is shown in figure
⁷⁴⁹ 3.1), are small electrode demonstrators and principally differ in the readout design: while
⁷⁵⁰ Monopix implements a column-drain R/O, an asynchronous R/O without any distribution
⁷⁵¹ of BCID has been used by TJ-Malta in order to reduce power consumption.



Figure 3.1: Timeline in TowerJazz productions in 180 nm CMOS imaging process

⁷⁵² Another Monopix series, but in 150 nm CMOS technology, has been produced by
⁷⁵³ LFoundry [12]. The main differences between the LF-Monopix1 and the TJ-Monopix1
⁷⁵⁴ (summarized in table 3.2), lay in the sensor rather than in the readout architecture, as
⁷⁵⁵ both chips implements a fast column drain R/O with ToT capability [13][14]. Concerning
⁷⁵⁶ the sensors, either are based on a p-type substrate, but with slightly different resistivities;
⁷⁵⁷ in addition LFoundry pixels are larger, thicker and have a large fill factor (the very deep n-
⁷⁵⁸ well covers ~55% of the pixel area). The primary consequence is that LF-Monopix1 pixels
⁷⁵⁹ have a higher capacity resulting in higher consumption and noise. As I discussed in section
⁷⁶⁰ 2.4.1, the fact that LF-Monopix has a large fill factor electrode is expected to improve its
⁷⁶¹ radiation hardness. Indeed, a comparison of the performance of the two chips showed that
⁷⁶² TJ-Monopix suffers a comparatively larger degradation of efficiency after irradiation, due
⁷⁶³ to the low electric field in the pixel corner; on the other hand, a drawback of the large fill
⁷⁶⁴ factor in LF-Monopix is a significant cross-talk.

	LF-Monopix1	TJ-Monopix1
Resistivity	$>2 \text{ k}\Omega\text{cm}$	$>1 \text{ k}\Omega\text{cm}$
Pixel size	$50 \times 250 \mu\text{m}^2$	$36 \times 40 \mu\text{m}^2$
Depth	$100\text{-}750 \mu\text{m}$	$25 \mu\text{m}$
Capacity	$\sim 400 \text{ fF}$	$\sim 3 \text{ fF}$
Preamplifier	charge	voltage
Threshold trimming	on pixel (4-bit DAC)	global threshold
ToT	8 bits	6 bits
Consumption	$\sim 300 \text{ mW/cm}^2$	$\sim 120 \text{ mW/cm}^2$
Threshold	$1500 e^-$	$\sim 270 e^-$
ENC	$100 e^-$	$\sim 30 e^-$

Table 3.1: Main characteristics of Monopix1 produced by TowerJazz and LFoundry [13][14]

765 The TJ-Monopix1 chip contains, apart from the pixels matrix, all the required support
 766 blocks used for configuration and testing:

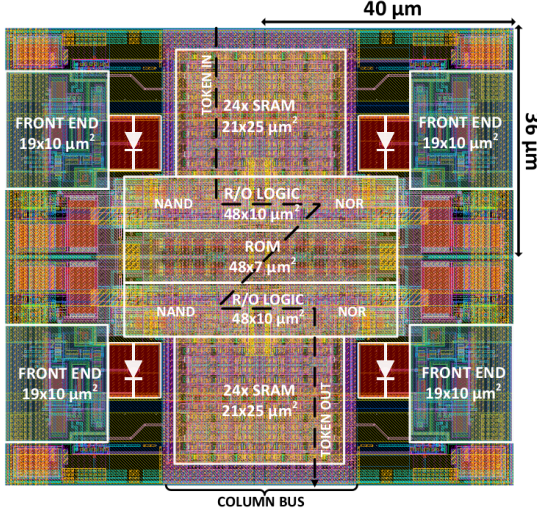
- 767 • the whole matrix contains 224×448 pixels, yielding a total active area approximately
 768 equal to 145 mm^2 over a total area of $1 \times 2 \text{ cm}^2$;
- 769 • at the chip periphery are placed some 7-bit Digital to Analog Converter (DAC), used
 770 to generate the analog bias voltage and current levels and to configuire the FE;
- 771 • at the EoC is placed a serializer to transferred datas immediately, indeed no trigger
 772 memory is implemented in this prototypes;
- 773 • the matrix power pads are distributed at the sides
- 774 • four pixels which have analog output and which can be monitored with an oscillo-
 775 scope, and therefore used for testing

776 Pixels are grouped in 2×2 cores (fig. 3.2a): this layout allows to separate the analog
 777 and the digital electronics area in order to reduce the possible interference between the
 778 two parts. In addition it semplifies the routing of data as pixels on double column share
 779 the same column-bus to EoC. Therefore pixels can be addressed through the physical
 780 column/row or through the logical column/row, as shown in fig. 3.2b: in figure is also
 781 highlighted the token propagaion path, whose I will discuss later.

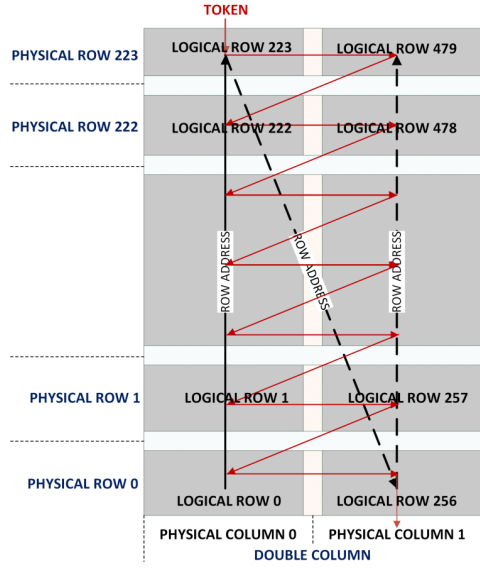
782 Concerning the integration1.3 of the chip in a readout path, TJ-Monopix1 chips have
 783 been wire-bonded on a dedicated carrier board , the Printed Circuit Board (PCB). Two
 784 other board between the DAQ and the chip: the General Purpose Analog Card (GPAC),
 785 which provides power supply channels, current/voltage bias sources and I/O buffer, and
 786 the MIO3 FPGA, which strictly interacts with the DAQ.

787 3.1 The sensor

788 As already anticipated, TJ-Monopix1 has a p-type epitaxial layer and a n doped small
 789 collection electrode ($2 \mu\text{m}$ in diameter); to avoid the n-wells housing the PMOS transistors
 790 competing for the charge collection, a deep p-well substrate, common to all the pixel FE



(a) Layout of a core containing 4 pixels. The analog FE and the digital part are separated in order to reduce cross-talk be



(b)

Parameter	Value
Matrix size	$1 \times 2 \text{ cm}^2$
Pixel size	$36 \times 40 \mu\text{m}^2$
Depth	$25 \mu\text{m}$
Electrode size	$2 \mu\text{m}$
BCID	40 MHz
ToT-bit	6
Power consumption	$\sim 120 \text{ mW/cm}^2$

Table 3.2

area, is used. TJ-Monopix1 adopts the modification described in section 2.4.2 that allows to achieve a planar depletion region near the electrode applying a relatively small reverse bias voltage. This modification improves the efficiency of the detector, especially after irradiation, however a simulation of the electric field in the sensor, made with the software TCAD (Technology Computer Aided Design), shows that a nonuniform field is still produced in the lateral regions of the pixel compromising the efficiency at the corner. Two variations to the process have been proposed in order to further enhance the transversal component of electric field at the pixel borders: on a sample of chip, which includes the one in Pisa, a portion of low dose implant has been removed, creating a step discontinuity in the deep p-well corner (fig. 3.3); the second solution proposed[MOUSTAKAS THESY, PAG 58] consists in adding an extra deep p-well near the pixel edge. A side effect of the alteration in the low dose implant is that the separation between the deep p-well and the p-substrate becomes weak to the point that they cannot be biased separately to prevent the punchthrough.

Moreover, to investigate the charge collection properties, pixels within the matrix are split between bottom top half and bottom half and feature a variation in the coverage of the deep p-well: the electronics area can be fully covered or not. In particular the pixels

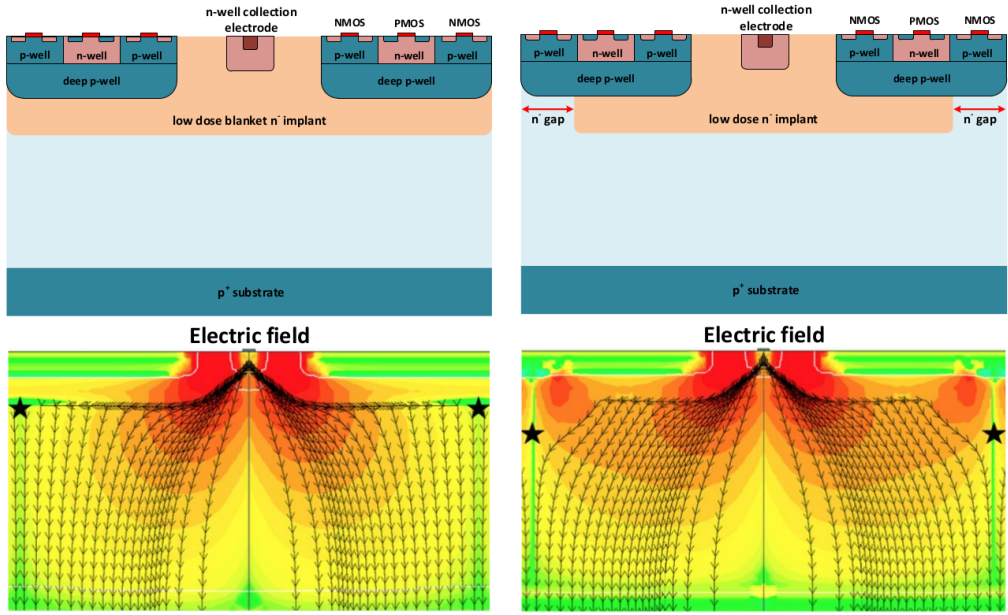


Figure 3.3: (a) The cross-section of a monolithic pixel in the TJ-Monopix with modified process; additionally in (b) a gap in the low dose implant is created to improve the collection of charge due to a bigger lateral component of the electric field. this point in figure is indicated by a star . transversal component of the electric field drops at the pixel corner

808 belonging to rows from 0 to 111 are fully covered (FDPW) and pixels belonging to rows
 809 from 112 to 223 have a reduced p-well (RDPW), resulting in a enhancement of the lateral
 810 component of the electric field.

811 3.2 Front end

812 One of the main advantage of this chip is the small collection electrode, which results in a
 813 small capacitance ($C_{in}=3\text{ fF}$) allowing for high input signal amplitude and single stage of
 814 amplification, which obviously improves the signal to noise ratio performance of the FE.
 815 Assuming a fully depleted epitaxial layer of $25\text{ }\mu\text{m}$, which corresponds approximately to
 816 a $20\text{ }\mu\text{m}$ of deep sensing volume, a MIP should produce $\sim 1600\text{ e}^-$, then:

$$V_{in} = \frac{1600\text{ e}^- \times 1.6 \cdot 10^{-19}\text{ C}}{3\text{ fF}} = 85\text{ mV} \quad (3.1)$$

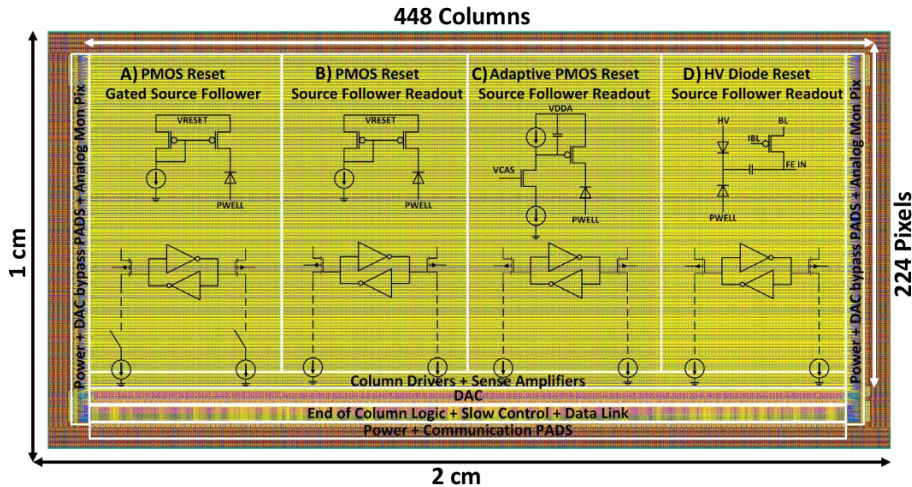
817 Secondly, a reset mechanism which slowly discharges the detector capacitance must be
 818 included in the circuit:

$$V_{in} = \frac{Q_s}{C_{in}} e^{-t/R_b C_{in}} \quad (3.2)$$

819 where R_b is the equivalent reset element. The general constraint which must be satisfied
 820 is that the discharge time $\tau = R_b C_{in}$ must be slower than the characteristic time of
 821 the amplifier, otherwise a signal loss could occurs. Traditionally the reset can be
 822 implemented in two different way: with a forward biased diode, that might be implemented
 823 by a simple p+ diffusion inside the well of the collection electrode n, or with a PMOS
 824 transistor. Despite of the semplicity of the diode reset, since it is a non-linear element,
 825 the discharge would depend on the quantity of charge Q generated on the n electrode,

826 prejudicing the linearity of the analog output (Q-ToT). To solve the issue, a PMOS reset
 827 is the method preferred in design such TJ-Monopix1 with analog output; the PMOS
 828 transistor, indeed, can acts as a constant current source and then used to discharge the
 829 sensor. Although the PMOS reset is capable of providing a constant current, it has to be
 830 manually re-tuned every time in order to restore the input DC baseline voltage; to do that
 831 a low-frequency feedback is used.

832 The matrix is split in four sections, each one corresponding to a different flavor of the
 833 FE, implemented in order to test more options.



834 Figure 3.4: TJ-Monopix1 has been developed in four different flavor. The flavor PMOS
 835 reset (B) is considered as the reference one.

836 All the flavors implement a source-follower double-column bus readout: the standard
 837 variation is the flavor B, that features a PMOS input reset (refered as "PMOS reset").
 838 Flavor A is identical to flavor B except for the realization of the source follower (it is a
 839 gated one): in the circuit of the gated versione there is a transistor more that operates on
 840 the baseline and on the feedback mechanism; this aim to reduce the power consumption
 841 and results in a higher signal baseline, and then in a lower effective threshold. C instead
 842 implements a novel leakage compensation circuit, with a PMOS reset configuration. More-
 843 over the collection electrode can be either DC-coupled to the readout electronics, as in
 844 flavors A, B, C, or AC-coupled through a metal-oxide-metal (MOM) capacitor, as in D
 845 is AC-coupled. The latter one allows applying a high bias voltage to the electrode n and
 846 for this reason the flavor D is also called "HV flavor". Unfortunately the "HV" suffer
 847 from a signal loss, which can achieve even the 50%, due to the additional parasitic capac-
 848 ity introduced at the input node. The HV voltage above which the breakdown begins is
 849 ~ 50 V; however at values bigger than 20 V, the gain does not increase anymore, since the
 depletion zone is already fully depleted.

849 3.2.1 ALPIDE-like

850 ALPIDE chips, developed by the ALICE collaboration, implemented a standard FE to the
 851 point that many CMOS MAPS detectors used a similar FE and are called "ALIPDE-like".
 852 Considering that both TJ-Monopix1 and ARCADIA-MD1 have an ALPIDE-like FE, I am
 853 going to explain the broad principles of the early FE stage. The general idea is of the
 854 amplification to transfer the charge from a bigger capacity[15], C_{source} , to a smaller one,

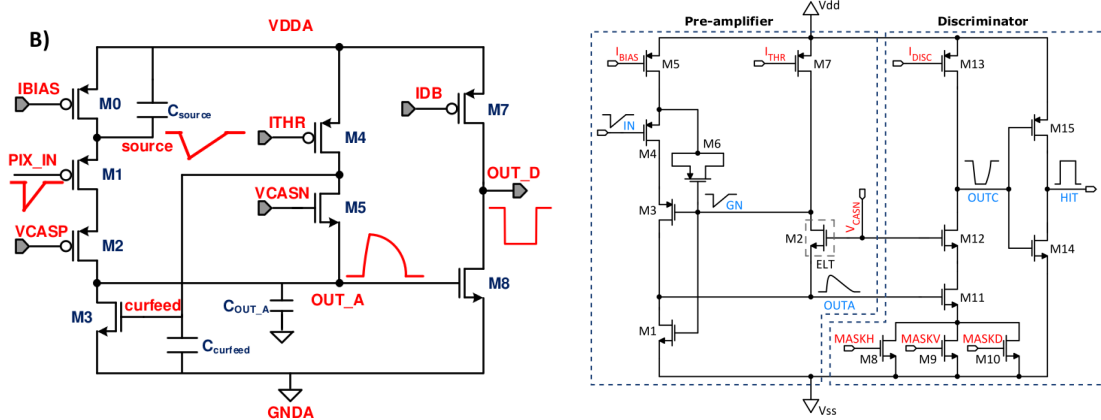


Figure 3.5

855 C_{out} : the input transistor M1 with current source IBIAS acts as a source follower and this
 856 forces the source of M1 to be equal to the gate input $\Delta V_{PIX_IN} = Q_{IN}/C_{IN}$.

$$Q_{source} = C_{source} \Delta V_{PIX_IN} \quad (3.3)$$

857 The current in M2 and the charge accumulates on C_{out} is fixed by the one on C_{source} :

$$\Delta V_{OUT_A} = \frac{Q_{source}}{C_{OUT_A}} = \frac{C_{source} \Delta V_{PIX_IN}}{C_{OUT_A}} = \frac{C_{Source}}{C_{OUT_A}} \frac{Q_{IN}}{C_{IN}} \quad (3.4)$$

858 A second branch (M4, M5) is used to generate a low frequency feedback, where VCASN
 859 and ITHR set the baseline value of the signal on C_{OUT_A} and the velocity to goes down
 860 to the baseline. **IL RUOLO DI CURVFEED NON L'HO CAPITO.** Finally IDB defines
 861 the charge threshold with which the signal OUT_A must be compared: depending on if
 862 the signal is higher than the threshold or not, the OUT_D is high or low respectively.

863 The actual circuit implemented in TJ-Monopix1 is shown in figure 3.5: the principal
 864 difference lays in the addition of disableing pixels' readout. This possibility is uttermost
 865 important in order to reduce the hit rate and to avoid saturating the bandwidth due to the
 866 noisy pixels, which typically are those with manufacturing defects. In the circuit transis-
 867 tors M8, M9 and M10 have the function of disabling registers with coordinates MASKH,
 868 MASKV and MASKD (respectively vertical, orizontal and diagonal) from readout: if all
 869 three transistors-signals are low, the pixel's discriminator is disabled. Compared with a
 870 configurable masking register which would allow disableing pixels individually, to use a
 871 triple redundancy reduces the sensistivity to SEU but also gives amount of intentionally
 872 masked ("ghost") pixels. This approach is suitable only for extremely small number N of
 873 pixel has to be masked: if two coordinate projection scheme had been implemented, the
 874 number of ghost pixels would have scale with N^2 , if instead three coordinates are used,
 875 the N's exponential is lower than 2 (fig. 3.6)

876 Foto dell'oscilloscopio per far vedere cosa fanno i parametri

877 3.3 Readout logic

878 TJ-Monopix1 has a triggerless, fast and with ToT capability R/O which is based on a
 879 column-drain architecture. On the pixel are located two Random Access Memory (RAM)
 880 cells to store the 6-bit LE and 6-bit TE of the pulse, and a Read-Only Memory (ROM)

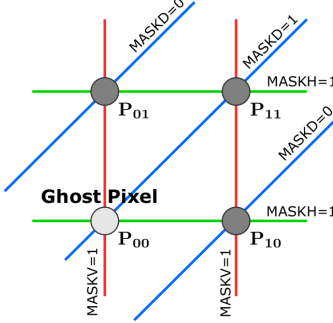


Figure 3.6

Parameter	Meaning	
IBIAS	mainly controls the rise time	yes
IDB	sets the discriminator threshold	yes
ITHR	sets the velocity of the return to the baseline	yes
ICASN	sets the baseline of the signal	yes
VRESET	sets the gain of the preamplifier	yes
IRESET	sets the gain of the preamplifier	no

Table 3.3: FE parameters which must be setted through the DAQ. "Function" means that higher parameter implies higher value

881 containing the 9-bit pixel address. Excluded these memories, TJ-Monopix1 hasn't any
 882 other buffer: if a hit arrives while the pixel is already storing a previous one, the new
 883 data get lost. After being read, the data packet is sent to the EoC periphery of the
 884 matrix, where a serializer transfers it off-chip to an FPGA (3.7). There a FIFO is used
 885 to temporarily stored the data, which is transmitted to a computer through an ethernet
 886 cable in a later time.

887 The access to the pixels' memory and the transmission of the data to the EoC, following
 888 a priority chain, is managed by control signals and is based on a Finite State Machine
 889 (FSM) composed by four state: no-operation (NOP), freeze (FRZ), read (RD) and data
 890 transfer (DTA). The readout sequence (??) starts with the TE of a pulse: the pixel
 891 immediately tries to grab the column-bus turning up a hit flag signal called *token*. The
 892 token is used to control the priority chain and propagates across the column indicating
 893 what pixel that must be read. To start the readout and avoid that the arrival of new hits
 894 disrupt the priority logic, a *freeze* signal is activated, and then a *read* signal controls the
 895 readout and the access to memory. During the freeze, the state of the token for all pixels
 896 on the matrix remains settled: this does not forbid new hits on other pixels from being
 897 recorded, but forbids pixels hit from turning on the token until the freeze is ended. The
 898 freeze stays on until the token covers the whole priority chain and gets the EoC: during
 899 that time new token cannot be turned on, and all hits arrived during a freeze will turn
 900 on their token at the end of the previous freeze. Since the start of the token is used to
 901 assign a timestamp to the hit, the token time has a direct impact on the time resolution
 902 measurement; this could be a problem coping with high hits rate.

903 The analog FE circuit and the pixel control logic are connected by an edge detector
 904 which is used to determine the LE and the TE of the hit pulse(fig. 3.9): when the TE

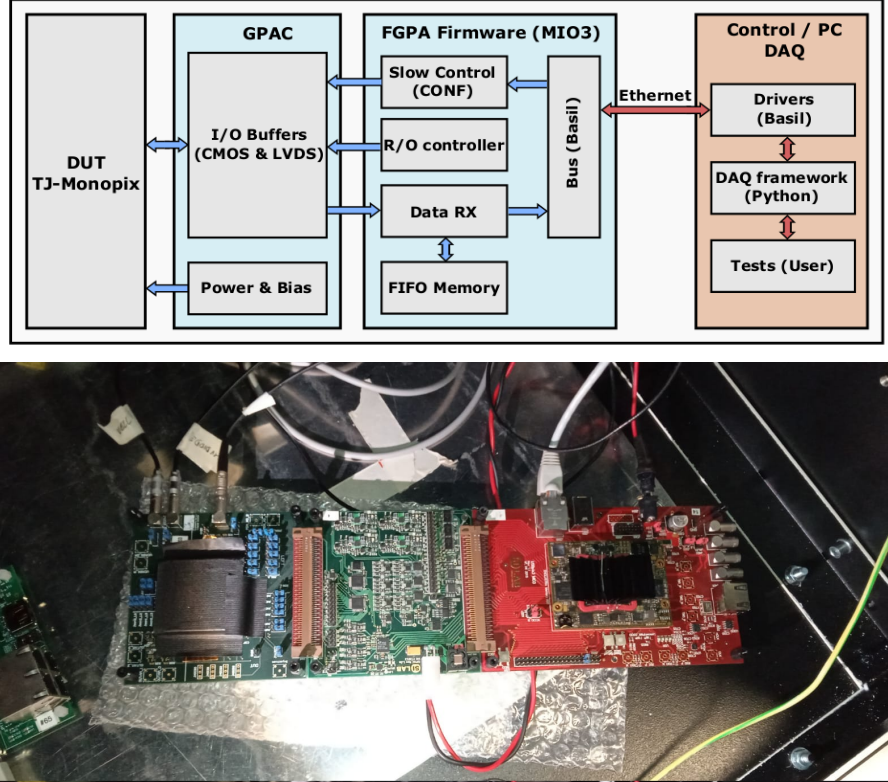


Figure 3.7: Main caption

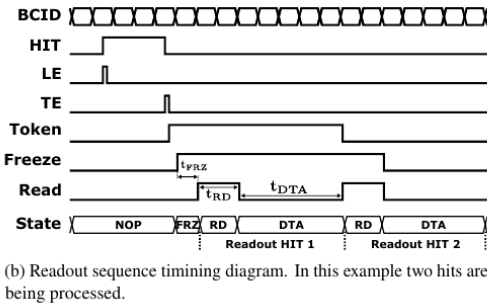


Figure 3.8: Readout timing diagram: in this example two hits are being processed

is stored in the first latch the edge detector is disabled and, if the **FREEZE** signal is not set yet, the readout starts. At this point the **HIT** flag is set in a second latch and a **Token** signal is produced and depending on the value of **Token** in the pixel can be read or must wait until the **Token in** is off. In figure an OR is used to manage the token propagation, but since a native OR logic port cannot be implemented with CMOS logic, a sum of a NOR and of an inverter is actually used; this construct significantly increases the propagation delay (the timing dispersion along a column of 0.1-0.2 ns) of the token and to speed up the circuit optimized solution are often implemented. When the pixel become the next to be read in the queue, and at the rising edge of the **READ** signal, the state of the pixel is stored in a D-latch and the pixel is allowed to use the data bus; the **TE** and the **HIT** flag latches are reset and a **READINT** signal that enable access of the RAM and ROM cells is produced.

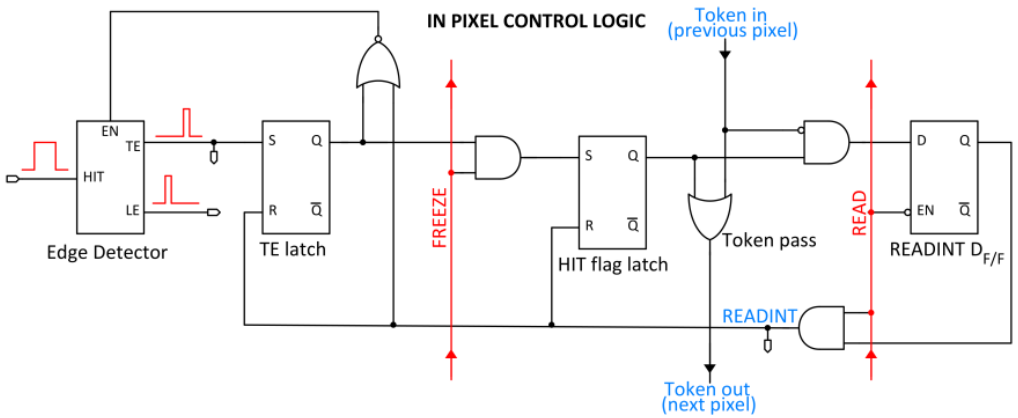


Figure 3.9

917 The final data must provide all the hits' information: the pixel address, the ToT and
 918 the timestamp. All those parts are assigned and appended at different time during the
 919 R/O chain:

- 920 • **Pixel address:** while the double column address (6-bit) is appended by the EoC
 921 circuit, the row address (8-bits for each flavor) and the physical column in the doublet
 922 (1-bit) are assigned by the in-pixel logic
- 923 • **ToT:** is obtained offline from the difference of 6-bits TE and 6-bits LE, stored by
 924 the edge detector in-pixel; since a 40 MHz BCID is distributed across the matrix,
 925 the ToT value is range 0-64 clock cycle which corresponds to 0-1.6 μ s
- 926 • **Timestamp:** The timestamp of the hit correspond to the time when the pixel set
 927 up the token; it is assigned by the FPGA, that uses the LE, TE and a 640 MHz
 928 clock to derive it. For all those hits which arrived while the matrix is frozen, the
 929 timestamp is no more correlated with the time of arrival of the particle

930 When the bits are joined up together the complete hit data packet is 27-bit. [16] [17]

931 ARCADIA (Advanced Readout CMOS Architectures with Depleted Integrated sensor
 932 Arrays) and SEED (Sensor with Embedded Electronic Developement) are both groups
 933 involved in the development of MAPS sensors based on the CMOS technology and both
 934 having LFoundry as industrial partner. Many concept and performances studies have been
 935 carried out with simulations and small-scale test structure by SEED, before ARCADIA,
 936 applying the experience developed with SEED to a full chip prototype, the MD1. MA-
 937 TISSE is an example of small-scale prototypes produced for testing: it is made by 24×24
 938 pixels organised in 4 columns; each pixel has an analog output, which allows for energy
 939 loss measurements, and a shutter snapshot readout with a speed that can reach 5 MHz.

940 The ARCADIA target are the development of a novel CMOS sensor platform allowing
 941 for fully depleted active sensors with thickness in range $50 \mu\text{m}$ to $500 \mu\text{m}$. A small charge
 942 collecting electrode to achieve a good signal to noise ratio, a high time resolution (the
 943 lower bound is set at $O(\mu\text{m})$ but more advanced solutions are investigating for a $O(10 \text{ ns})$)
 944 and a scalable readout architecture with low power consumption are the main requirement
 945 imposed by ARCADIA; the Main Demonstrator 1, has been submitted in 2020, and its
 946 characteristic are shown in table 3.4. A second main demonstrator (ARCADIA-MD2) has
 947 been submitted in Summer 2021, featuring a similar design of MD1 and which is expected

Parameter	Value
Matrix size	$\times \text{ cm}^2$
Pixel size	$25 \times 25 \mu\text{m}^2$
Depth	48/100/200 μm
Electrode size	$9 \times 9 \mu\text{m}^2$
Power consumption	$\sim 10 \text{ mW/cm}^2$

Table 3.4

948 to be faster and to have a lower power consumption thanks to a logic and buffering
 949 optimisation.

950 3.4 The sensor and the front end

951 ARCADIA-MD1 is an LFoundry chip which implements the CMOS technology in 110 nm
 952 **??. The standard p-type substrate is replaced by a n-type ?**

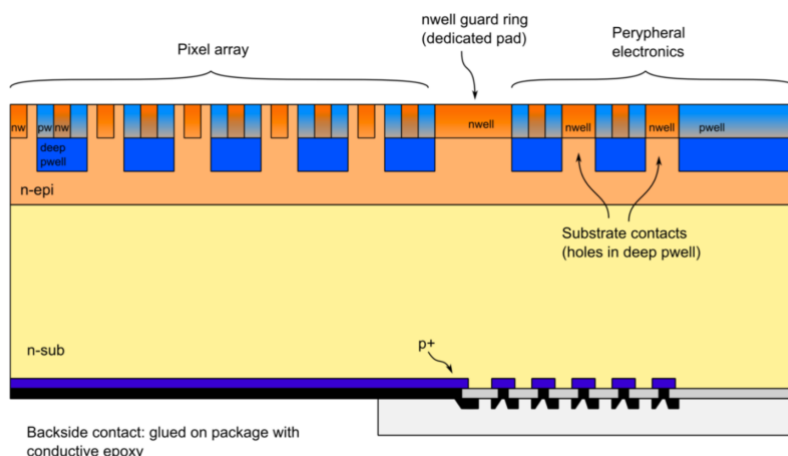


Figure 3.10: Cross section of the ARCADIA MD1 sensor

953 The sensor is made by a *p* substrate and an *n* doped diode within a *n* epitaxial layer.
 954 Being part of DMAPS category, it is operated in fully depletion and the charge is then
 955 fastly collected by drift. Up to now the sensor has been implemented in three different
 956 variant: 48 μm , 100 μm and 200 μm thick, each with the same FE and readout logic but
 957 requiring a diffent biasing.

958 MD1 chips have been submitted in two different front end options: they are commonly
 959 called ALIPDE-like and bulk-driven. The differences between them are in the FE circuit
 960 and in the biasing current of the registers, while the underlying readout is the same.
 961 The main difference is in the amplification stage, while in the ALPIDE-like flavor the
 962 amplification is implemented as explained in section 3.2.1, in the bulk-driven flavor the
 963 gain is adjusted by the ratio of two transconduttances. Consequently, some of the biasing
 964 registers, whose current is settable externally by the DAQ, have different default values
 965 and they might not be available at all in one of the flavor. An example is the ICLIP
 966 register, which is available only in the bulk driven flavor despite the transistor to which

967 refers is implemented in both the flavor; its function is similar to the *curfeed* capacitor in
 968 figure 3.5(a), which controls the current in the input branch of the FE and also influences
 969 the value of tha baseline at the discriminator input.

970 There are three types of configuration registers which are used to configure the matrix:

971 • the Pixel Configuration Register, which is a 2-bits word used for enableing respec-
 972 tively the masking and injection functionalities. The on pixel Pixel Configuration
 973 Register circuit and how the mask/injection can be enable/disable is shown in figure
 974 3.11.

975 • the Internal Configuration Register, which are used for the communication with the
 976 FPGA, for example to send a pulse, reset or configure the whole matrix.

977 • the Global Configuration Registers, which are used to set the configuration of the
 978 FE parameters are similar to the one of the TJ-Monopix1 circuit.

979 Their bias with the one of the sensors are supplied by padframes (a top, a bottom and a
 980 side one) placed aside the matrix, which also provide the clock, the reset, the test pulse
 981 for the injection circuit and the comunication signals.

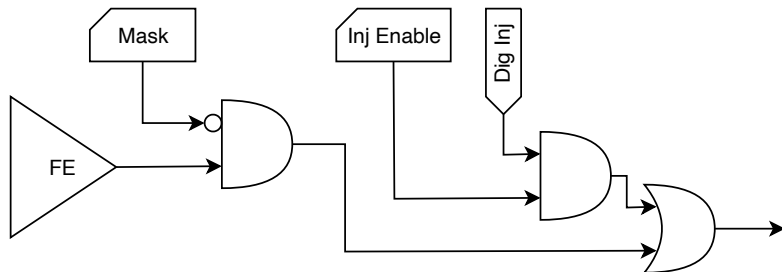


Figure 3.11: Logic used for each pixel to implement the injection and the masking.

981

982 3.5 Readout logic and data structure

983 3.5.1 Matrix division and data-packets

984 One of the main ambition of the MD1 is to achieve the lowest possible power consumption,
 985 hopefully less than 20 mW/cm^2 ; this is pricipally due to the hope of application also in
 986 space experiment field, where the power consumption and the cooling are for sure an
 987 issue. In order to undergo that requirement, the matrix is clockless and the readout is
 988 triggerless; moreover the chip can be operated both in the high rate mode and low rate
 989 depending on if only one or all serializers, which are placed at the periphery of the matrix
 990 are enabled or only one is shared between the sections; in addition, to save as much area
 991 as possible, no buffer have been included on the matrix at the expense of the maximum
 992 hit rate sustainable. The readout then is completely data push and when a hit is received
 993 immediately starts the readout mechanism to trasmit it off chip.

994 The board hosting the chip is connected with a breakout board, which is connected to
 995 the FPGA; a data packet sent to the EoS, is then encoded and trasmitted to the FPGA
 996 using a 320 MHz DDR serializers and then trasmitted by ethernet to the PC. A photo of
 997 the experimental setup is shown in figure ??.

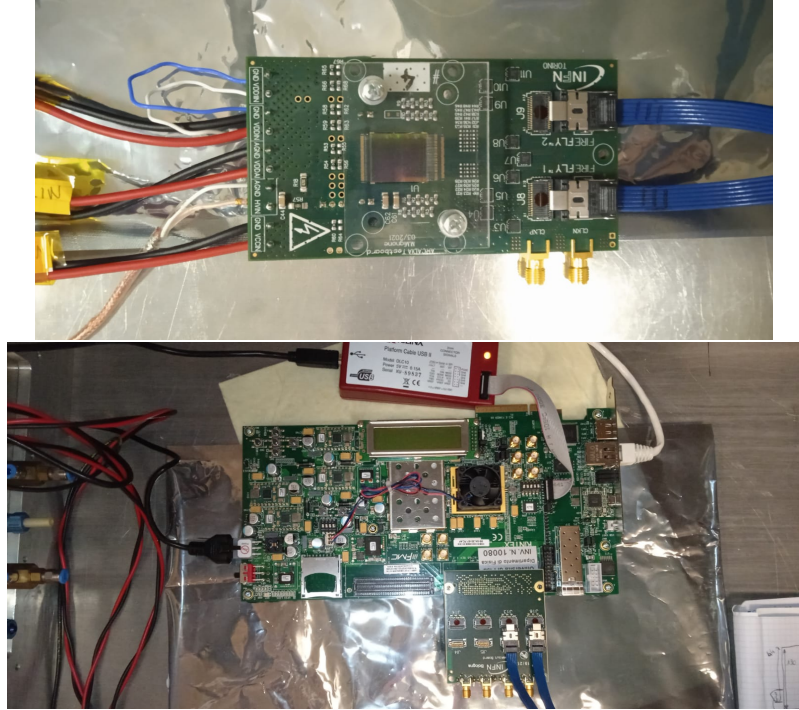


Figure 3.12: (a) Board hosting the MD1 chip. (b) FPGA and breakout board. The chip and breakout boards must be connected with the blue cables

998 3.5.2 Matrix division and data-packets

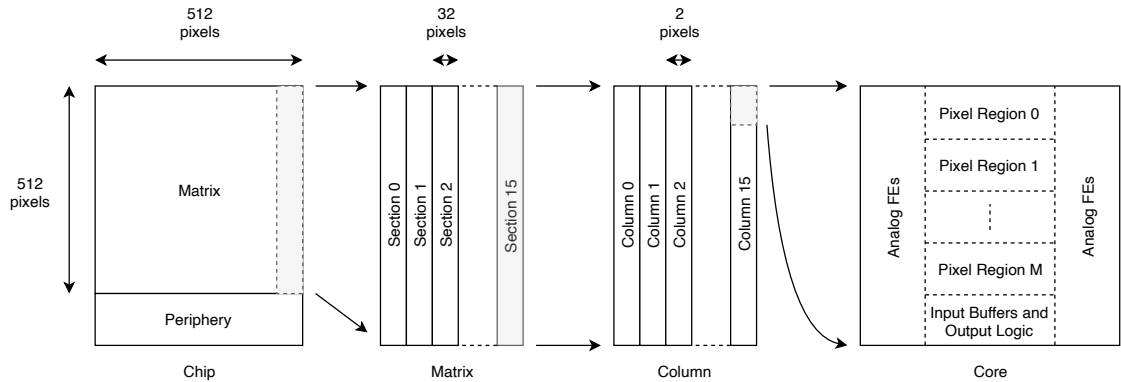


Figure 3.13: Hierarchy of the matrix division

999 Also the chip structure is meant to optimize the power consumption and the scalability
1000 for future up-scaling; in particular it is divide into a physical and logical hierarchy, which
1001 also reflects in the way the data pakets are built (tab.3.5). First of all, the 512 columns
1002 are split in 16 sections each one containing 512×32 pixels and having its own biasing lines
1003 and serializers at the matrix periphery. Each section is is devided 512×2 double-column
1004 mirrored, which just as in TJ-Monopix1, share the same readout buses placed between
1005 them and having analog logic on the sides. The rows, then, are divided in group of 32,
1006 resulting in core with 32×2 pixels. Finally each core is sub-divided in regions, each one
1007 containing 4×2 pixels.

1008 The readout has been designed with the constraints of being capable of handle with
1009 hit rate of $100 \text{ MHz}/\text{cm}^2$, then it has been optimized to minimize the amount of logic and

Bits	Meaning
31:24	timestamp
23:20	section index
19:16	column index
15:9	pixel region
8:0	bitmap

Table 3.5: Data packet structure implemented by the MD1 readout logic.

1010 to have a high bandwidth of transmission of the data to the periphery. For this reason not
 1011 all pixels have been provided by the readout logic. In particular, each pixel region can
 1012 either be Master or Slave, depending on if has or has not the readout capability. The
 1013 Master's data packets are therefore composed of two parts: the bitmap of the Master
 1014 itself and the one of Slave. Moreover, the pioneer idea of ARCADIA-MD1, which has as
 1015 finally goal the test of a readout capable of transmit cluster data in as few data packets
 1016 as possible, is the possibility of the Master to decide what Slave (top or bottom) read; the
 1017 information of what Slave has been selected is represented by a bit, often called *hot bit*, in
 1018 the data-packet. Every pixel has an associated status register, that essentialy is a flip flop
 1019 (FF), which is set to 1 when the pixel stores a hit; an OR of the FF whithin the Master
 1020 or the Slave region generates an active flag which is used to require a readout by the EoS.
 In figure 3.14 is shown the circuit with the logic of assignment of the Slave to the Master.

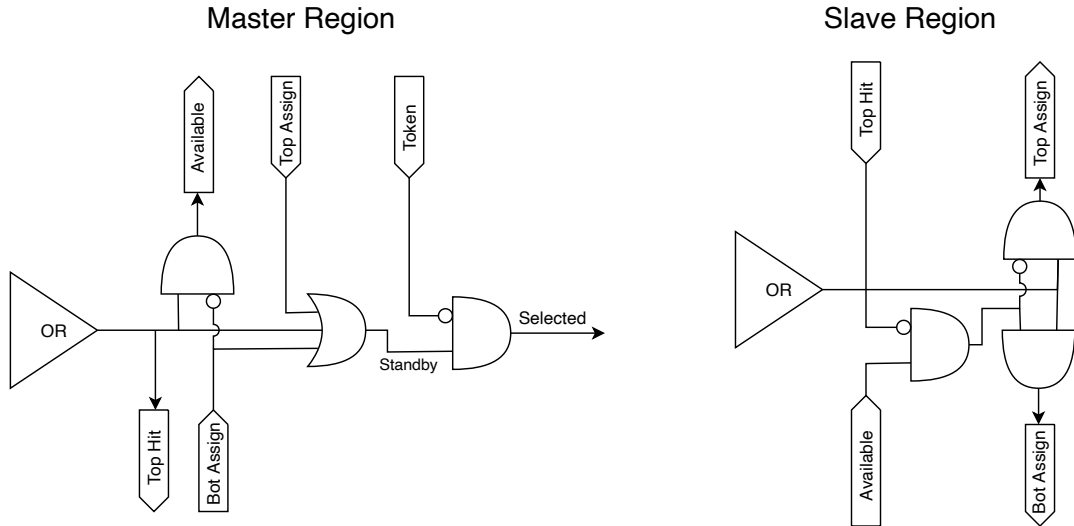


Figure 3.14: Logic of the circuit to implement the online clustering and deciding if to assign the Slave to the top or bottom Master.

1021
 1022 Depending on the active flags of the neighbouring Masters, the Slave bitmap is assigned
 1023 to the one at the top or bottom. If both the Masters have an active flag, the Slave
 1024 is assigned to the top one. In the example in figure 3.15 two Master-Slave regions are
 1025 considered: the bitmaps of the Master (red colored in the example) and Slave (blue colored)
 1026 are joined together within a unique data packet and a bit (green colored) is used to specify
 1027 the Slave.

1028 The data packets are transmitted to the End of Section (EoS) with a priority chain

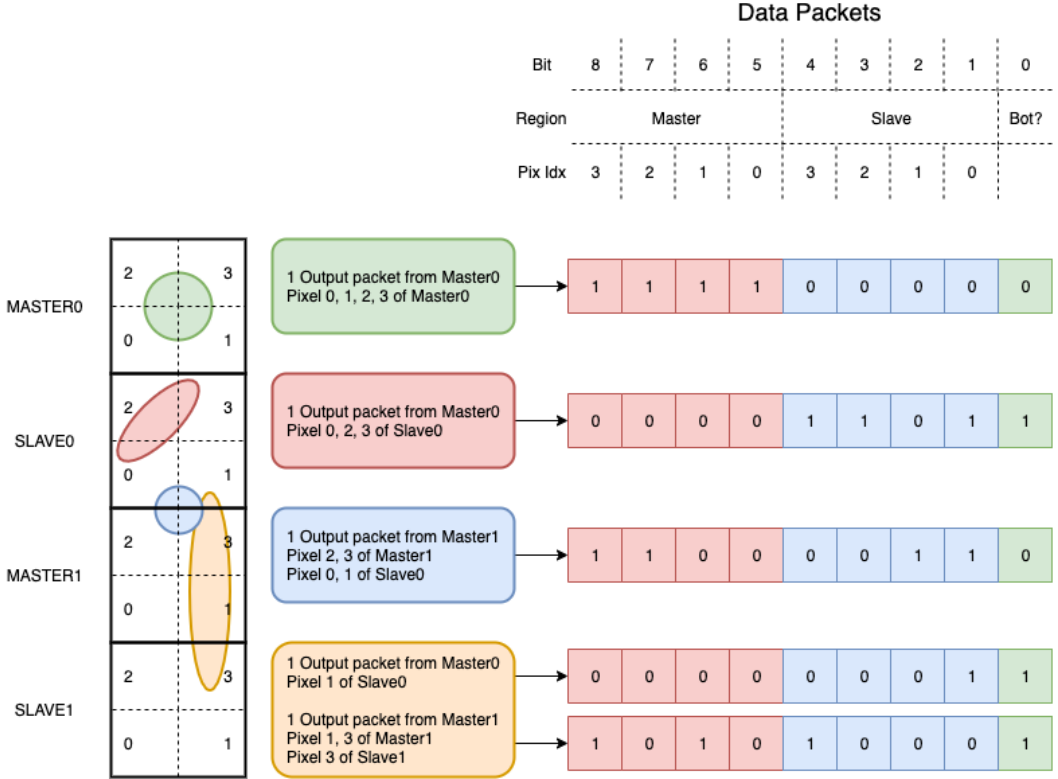


Figure 3.15: Different cluster structures and the data packet produced by them are shown in the example.

similar to what happens in TJ-Monopix1. If at least one Master set a high flag, a **Token** signal is generated and is assigned to the high priority Master in the column, together with a **Full** flag which is distributed to the active Masters in the whole column in order to deny more region to be accessed at the same time. The readout then propagates down the column from Master to Master, skipping the empty cores; the Master selected for the readout is the one with the flag high and with an input (from top) **Token** equal to 0. In the example in figure 3.16 the **Token** is propagated from the Pixel Region (PR) 10 to the PR 7. In the three readout steps the red Masters are the ones selected for the readout, while the yellow are the ones which an active flag high; gray color is used for empty regions. When a specific Master has been selected, a **Read** signal is generated both to transmit the data to the EoS and also to generate a reset for the just read pixels. Once the pixels are reset, the Master's **Full** and **Token** flags fall, and the following region which satisfies the two readout conditions explained above, becomes selected.

The performances of the readout has been studied with simulations by the designer of the chip. Random hits events with cluster size of 4 pixels on average, with a Poissonian distribution in time and uniformly distributed on the matrix has been generated. They state that with particle hit rate of 100 MHz/cm², considering a portion of matrix of three section (512×96), the efficiency results to be 98.7%, while reducing the hit rate to 80 MHz/cm² it is even higher achieving the 99.95%.

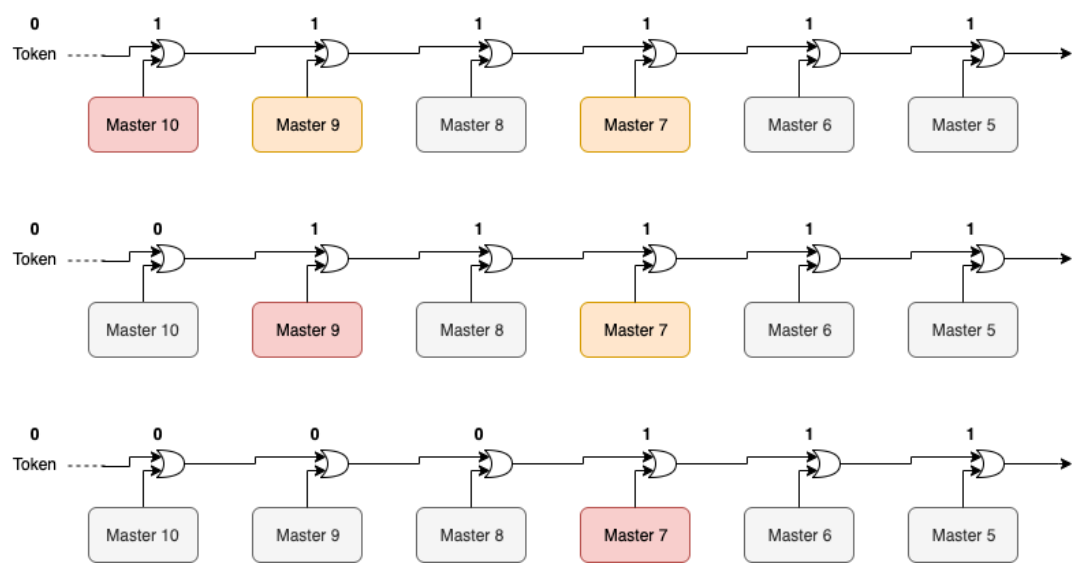


Figure 3.16

1048 **Chapter 4**

1049 **Characterization**

1050 Rifai il conto della lunghezza di attenuazione. Ho trovato (presentazione Luciano Mus) 29
1051 um per ka e 37 um per kb.

1052 **4.1 TJ-Monopix1 characterization**

1053 **4.1.1 Threshold and noise: figure of merit for pixel detectors**

1054 A characterization of threshold and noise is typically necessary since these values have an
1055 impact on the operating conditions and on the performance of the chips, so much that
1056 the signal to threshold ratio may be considered as the figure of merit for pixel detectors
1057 rather than the signal to noise ratio. The mean minimum stable threshold evolved through
1058 different generation of chips: in the 1st generation it was around 2500 e^- while in the 3rd
1059 (corresponding to nowadays chips) is less than 500 e^- . This allows in thinner sensors with
1060 smaller signals: from $16\,000 \text{ e}^-$ produced in $200 \mu\text{m}$, the signal expected moved down to
1061 2000 e^- produced in $25 \mu\text{m}$. In agreement with this, the threshold of TJ-Monopix1 is
1062 around 500 e^- .

1063 Obviously the threshold has to be located between the noise peak around the baseline
1064 and the signal distribution, in particular it has to be low enough to mantain a high signal
1065 efficiency, but also high enough to cut the noise: for a low threshold many pixels can fire
1066 at the same time and a positive feedback can set off a chain reaction eventually, causing
1067 all the other pixels to fire. Thus, the noise sets a lower bound to the threshold: if an
1068 occupancy $\leq 10^{-4}$ is required, for example, a probability of firing lower than that value
1069 is needed and this, assuming a gaussian noise, requires that the threshold is set at least
1070 3.7σ , with σ the RMS of the noise. In this case, if the noise is 100 e^- (resonable), the
1071 threshold must be higher than $3.7 \times 100 \text{ e}^-$. Typically this argument sets only a minimal
1072 bound to the threshold since the variation with time and from pixel to pixel have to be
1073 taken into account: the temperature, the annealing (for example, the radiation damages in
1074 the oxide layer causes shift of MOSFET threshold voltage) and the process parameters
1075 variation across the wafer (as for example process mismatch between transistors).

1076 On the other hand, concerning the noise, given that the first stage of amplification is
1077 the most crucial, since in the following stages the signal amplitude is high compared to
1078 additional noise, it is valued at the preamplifier input node. Then, the noise is parame-
1079 terized as Equivalent Noise Charge (ENC), which is defined as the ratio between the noise
1080 N at the output expressed in Volt and the out voltage signal S produced by 1 e^- entering

1081 in the preamplifier:

$$ENC = \frac{N_{out}[V]}{S_{out}[V/e-]} = \frac{V_{noise}^{RMS}}{G} \quad (4.1)$$

1082 with G expressed in V/e-; as the gain increases, the noise reduces .

1083 Considering the threshold dispersion a requirement for the ENC is:

$$ENC < \sqrt{(T/3.7)^2 - T_{RMS}^2(x) - T_{RMS}^2(t)} \quad (4.2)$$

1084 where the T is the threshold set, T_{RMS} is the threshold variation during time (t) and
1085 across the matrix (x); a typical reasonable value often chosen is 5 ENC.

1086 Because of the changing of the 'real' threshold, the possibility of changing and adapting
1087 the setting parameters of the FE, both in time and in space is desiderable: these parameters
1088 are usually set by Digital to Analog Converter (DAC) with a number of bit in a typical
1089 range of 3-7. Unfortunately DAC elements require a lot of space that may be not enough
1090 on the pixel area; therefore, the FE parameters are typically global, which means that they
1091 are assigned for the whole chip, or they can be assigned for regions the matrix is divided
1092 into. The former case corresponds to TJ-Monopix1's design in which 7 bits are used for
1093 a total 127-DAC possible values, while the latter corresponds to the ARCADIA-MD1's
1094 one, **where quanti bit??**. An other possibility, for example implemented in TJ-Monopix2,
1095 is allocate the space on each pixel for a subset of bits, then combinig the global threshold
1096 with a fine tuning. If so, the threshold dispersion after tuning is expected to decrease
1097 depening on the number of bits available for tuning:

$$\sigma_{THR,tuned} = \frac{\sigma_{THR}}{2^{nbit}} \quad (4.3)$$

1098 where σ_{thr} is the RMS of the threshold spread before tuning.

1099 To measure the threshold and noise of pixels a possible way is to make a scan with
1100 different known injected charge: the threshold corresponds to the value where the efficiency
1101 of the signal exceeds the 50%, and the ENC is determined from the slope at this point.
1102 Assuming a gaussian noise, e.g. a noise whose transfer function turns a voltage δ pulse in a
1103 gaussian distribution, the efficiency of detecting the signal and the noise can be described
1104 with the function below:

$$f(x, \mu, \sigma) = \frac{1}{2} \left(1 + erf \left(\frac{x - \mu}{\sigma\sqrt{2}} \right) \right) \quad (4.4)$$

1105 where erf is the error function. Referring to 4.4 the threshold and the ENC corresponds
1106 to the μ and σ .

1107 I used the injection circuit available on the chip to inject 100 pulses for each input
1108 charge for a fixed threshold. The injection happens on a capacity at the input of the FE
1109 circuit, whose nominal value is 230 aF and from which the conversion factor from DAC
1110 units to electrons can be obtained: for the PMOS flavor, for example, since the DAC are
1111 biased at 1.8 V, the Least significant Bit (LSB) corresponds to a voltage of 14.7 mV from
1112 which the charge for LSB $1.43 \text{ e-}/\text{mV}$ and the conversion factor therefore is $20.3 \text{ e-}/\text{DAC}$.
1113 While this value is equivalent for all the PMOS flavor, the HV flavor is expected to have a
1114 different conversion factor, $\sim 33 \text{ e-}/\text{DAC}$, beacuse of the different input capacity. Besides
1115 the charge, also the duration and the period of the injection pulse can be set; it is important
1116 to make the duration short enough to have the falling edge during the dead time of the
1117 pixel (in particular during the FREEZE signal) in order to avoid the undershoot, coming

	PMOS A	PMOS B	PMOS C	HV
Threshold [e ⁻]	401.70±0.15	400.78±0.24	539.66±0.58	403.87±0.19
Threshold dispersion [e ⁻]	32.90±0.11	32.97±0.17	55.54±0.42	44.67±0.15
Noise [e ⁻]	13.006±0.064	12.258±0.068	13.88±0.11	11.68±0.10
Noise dispersion [e ⁻]	1.608±0.044	1.504±0.046	1.906±0.072	1.580±0.068

Table 4.1: Mean threshold and noise parameters for all flavor and their dispersion on the matrix.

at high input charge, triggering the readout and reading spurious hits. Since the injection circuit is coupled in AC to the FE, if the falling edge of the pulse is sharp enough to produce an undershoot, this can be seen as a signal.

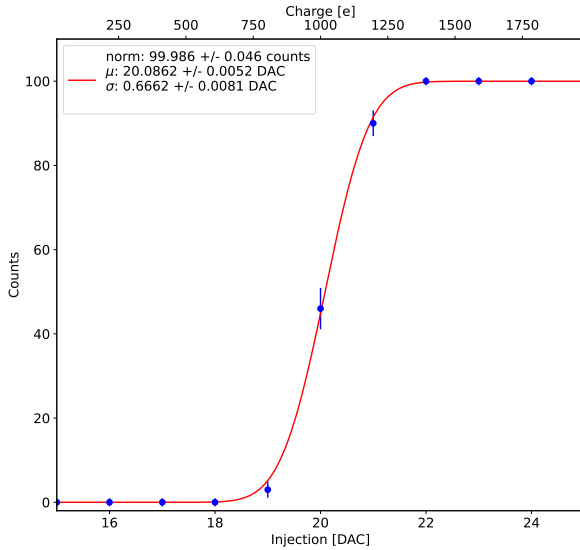


Figure 4.1: S-curve for pixel (10, 10) of the PMOS flavor (flavor B) with IDB fixed at 40 DAC. The conversion of charge injected from DAC to electrons has been performed using a nominal conversion factor of 20.3 e⁻/DAC *Mi sono resa conto che l'asse superiore è sbagliato. Devo rigenerare il plot*

with IDB equal to 40 DAC

Therefore I fitted the counts detected using the function in equation 4.4. Figure 4.1 shows an example of such fit for a pixel belonging to the flavor B, while in figure 4.2 are shown the 1D and 2D distributions of the parameters found. I fitted the 1D distributions with a gaussian function to found the average and RMS of the noise and the threshold for each flavor across the matrix. The results are reported in table 4.1.

In the map at the top right panel of figure 4.2 (IDB=40 DAC) a slightly lower threshold is visible in the first biasing section (columns from 0 to 14); similar structures, but extended to the entire matrix, appear more evidently when using different IDB values. The systematic threshold variation across the biasing group has not a known motivation, but one could certainly be the transistor mismatch of the biasing DAC registers IDB and ICASN, which both adjust the effective threshold (I recall that ICASN regulate the

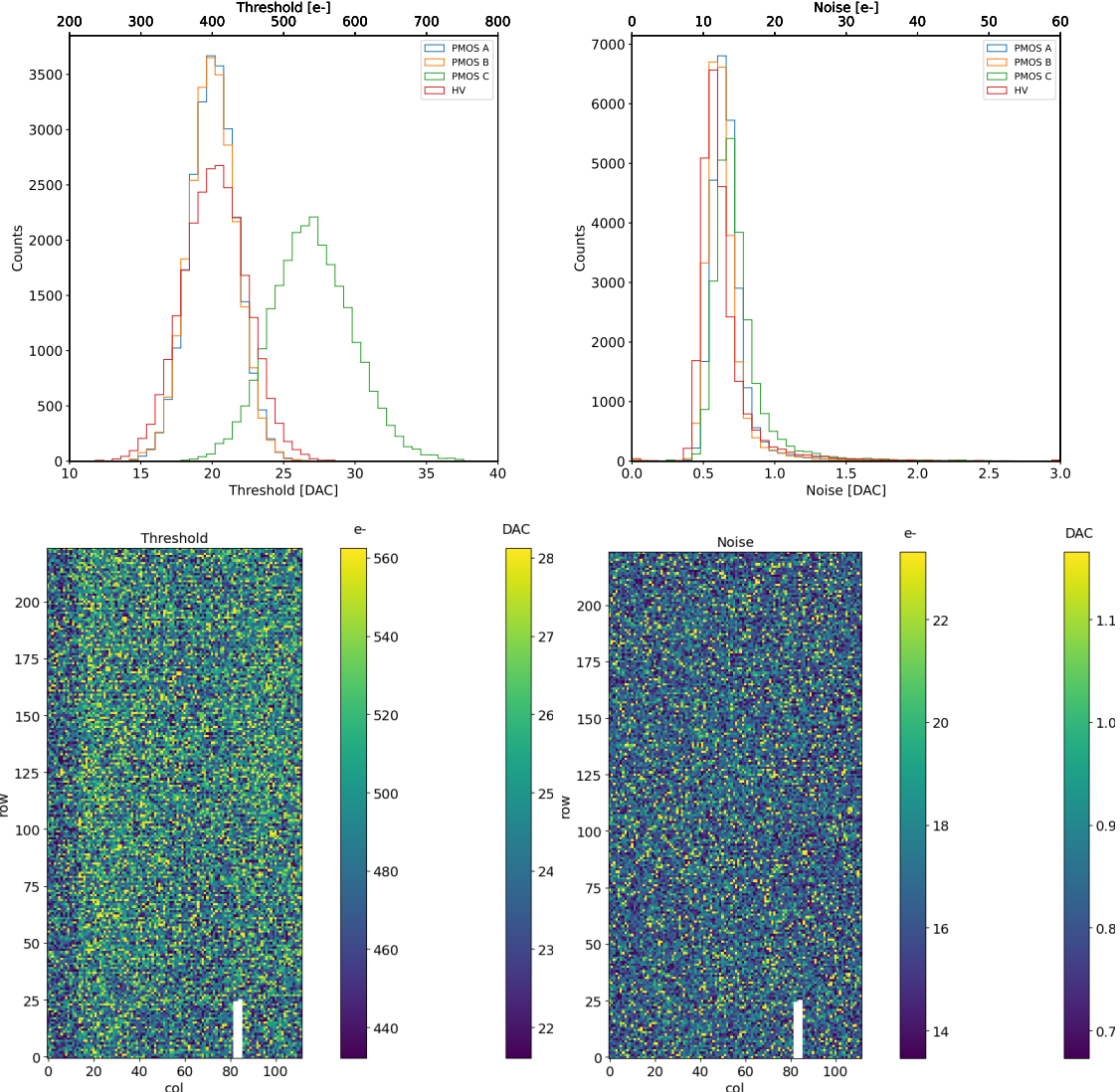


Figure 4.2: Histograms of the threshold (a) and the noise (b) found fitting the s-curve of all flavor with IDB fixed at 40 DAC. Below there are the maps of the threshold (a) and the noise (b), respectively, found fitting the s-curve with IDB fixed at 40 DAC for the PMOS flavor (B). The white pixels have the injection circuit broken.

1133 baseline).

1134 To verified the trend of the threshold as a function of the front end parameter IDB and
 1135 find its dynamic range, I have permormed different scans changing the FE register IDB.
 1136 For each IDB I have injected the whole matrix and search for the mean and the standard
 1137 deviation of the threshold and noise distributions. The results are shown in figure 4.3:
 1138 the blue points are the mean threhsold found whithin the matrix, while in green is shown
 1139 the width of the threshold distribution, aka the threshold dispersion. While the threshold
 1140 increases, the ENC decreases of $\sim 4 \text{ e-}$,which is $\sim 1/3$ of the noise at IDB=40 DAC.

1141 Then, to evaluet the operation and the occupancy of the chip at different threshold
 1142 I have made long acquisitions of noise at different IDB and check how the number of
 1143 pixel masked changes with the threshold. The masking algorithm I have used search for
 1144 pixels with rate $> 10 \text{ Hz}$ and mask them. With such algorithm, in our standard condition,

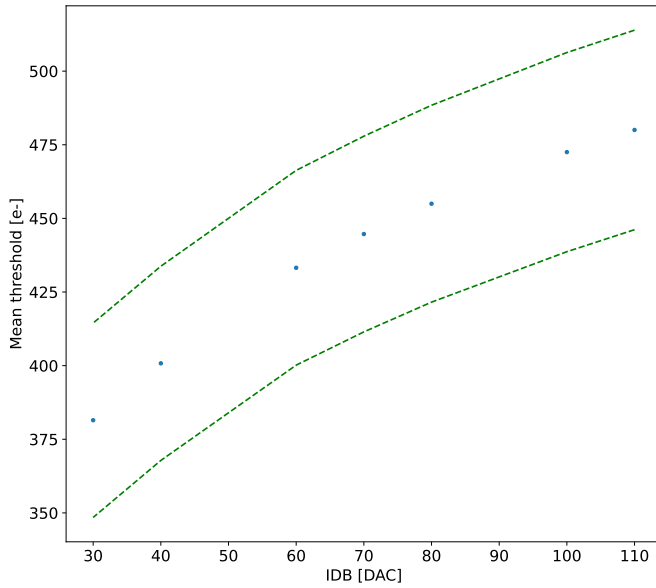


Figure 4.3: Flavor PMOS (B) with Psub-Pwell biased at -6 V. Threshold measured in electrons vs the register which sets the threshold, IDB.

1145 IDB=40 DAC, a very low noise hit rate is intentionally achieved masking a dozen of pixels
 1146 of the whole flavor.

1147 4.1.2 Linearity of the ToT

1148 I have already said in chapter ?? that TJ-Monopix1 returns an output signal proportional
 1149 to the charge released by a particle in the epitaxial layer, which is the Time over Threshold;
 1150 the ToT is saved as a 6-bit variable and then has a dynamic range equal to 0-64, which
 1151 corresponds to 0 μ s to 1.6 μ s assuming a clock frequency of 40 MHz. When a pulse is longer
 1152 than 1.6 μ s the counter rolls back to zero and there is no way to distinguish that charge
 1153 from a lower one with the same ToT: that is the rollover of the ToT (4.4(a)).

1154 In order to associate the ToT (in range 0-64) to the charge, a calibration of the signal
 1155 is necessary. Assuming the linearity between ToT and the charge, Q can be found:

$$Q [DAC] = \frac{(ToT [au] - offset [au])}{slope [au/DAC]} \quad (4.5)$$

1156 where m and q are the fitted parameters of the calibration. It is important to keep in mind
 1157 that the main application target of TJ-Monopix1 is in the inner tracker detector of HEP
 1158 experiments, then the main feature is the efficiency, then a rough calibration of the signal
 1159 to charge is fine. The ToT information can be used both to better reconstruct the charge
 1160 deposition in cluster in order to improve the track resolution, and for particle identification,
 1161 especially for low momentum particles which do not reach the proper detectors.

1162 The study of the output signal is made possible via the injection: since the pulses
 1163 are triangular, the ToT is expected to be almost therefore, to prevent th linear. To verify
 1164 this statement and study the deviations from linearity I fitted the ToT versus the charge
 1165 injected for all the pixels within the matrix. In figure 4.4(b) there is an example of fit

for a pixel belonging to the flavor B, while in figure 4.5 there are the histograms and the maps of the parameters of the line-fit for all flavors with IDB fixed at 40 DAC. Here again a difference among the biasing section appears: since the slope of the ToT is related with the gain of the preamplifier (increasing the gain also increases the ToT), the mismatch is probably due to the transistor contributing to the amplification stage.

I fitted the average ToT of all the pulses recorded as a function of the pulse amplitude; data affected by rollover have been removed in order to avoid introducing a bias in the mean values. In figure 4.4 (b) are shown both the fits with a line (red) and with a second order polynomial (green): at the bounds of the ToT range values deviate from the line model. Since the deviation is lower than 1% and it only interests the region near the 0 and the 64, in first approximation it is negligible.

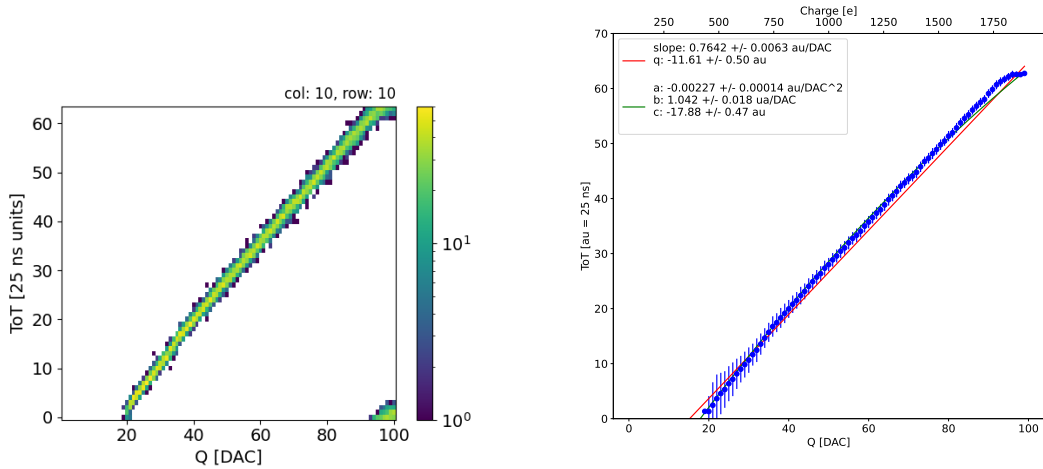


Figure 4.4: The figures refer to pixel (10,10) of the PMOS-reset flavor B with IDB fixed at 40 DAC. (a) Histogram of the injection pulses: the ToT is in range 0-64 since it is represented by 6 bit, so when achieving the 64 it rolls over back to the zero. (b) Mean ToT vs the the charge: the mean has been calculated cutted the rolling hits.

4.1.3 Calibration of the ToT

Finding a calibration for the ToT means defining a way to pass from the ToT values (0-64 clock counts) to a spectrum expressed in electrons collected. The principles of the calibration are the following: the ToT in clock counts maps (eq.4.1.2) a DAC range between the threshold and a value which depends on the pixel and generally is around 90-100 DAC. Assuming that a 0 DAC signal corresponds to 0 e⁻, if another reference point is fixed, a linear calibration function can be defined. After the calibration the ToT goes to map a charge range between the threshold and Q_{max} which is a function of the pixel and is around 2 ke⁻.

Moreover, considering that the charge injected in the FE goes to fill a capacitor C which is different from pixel to pixel, the true charge injected does not correspond to what expected assuming C equal to 230 aF, which is the nominal value. Accordingly to that, a measurement of this value provides both an absolute calibration of C and a conversion factor K to have a correspondence of the DAC signal in electrons. K and C are defined

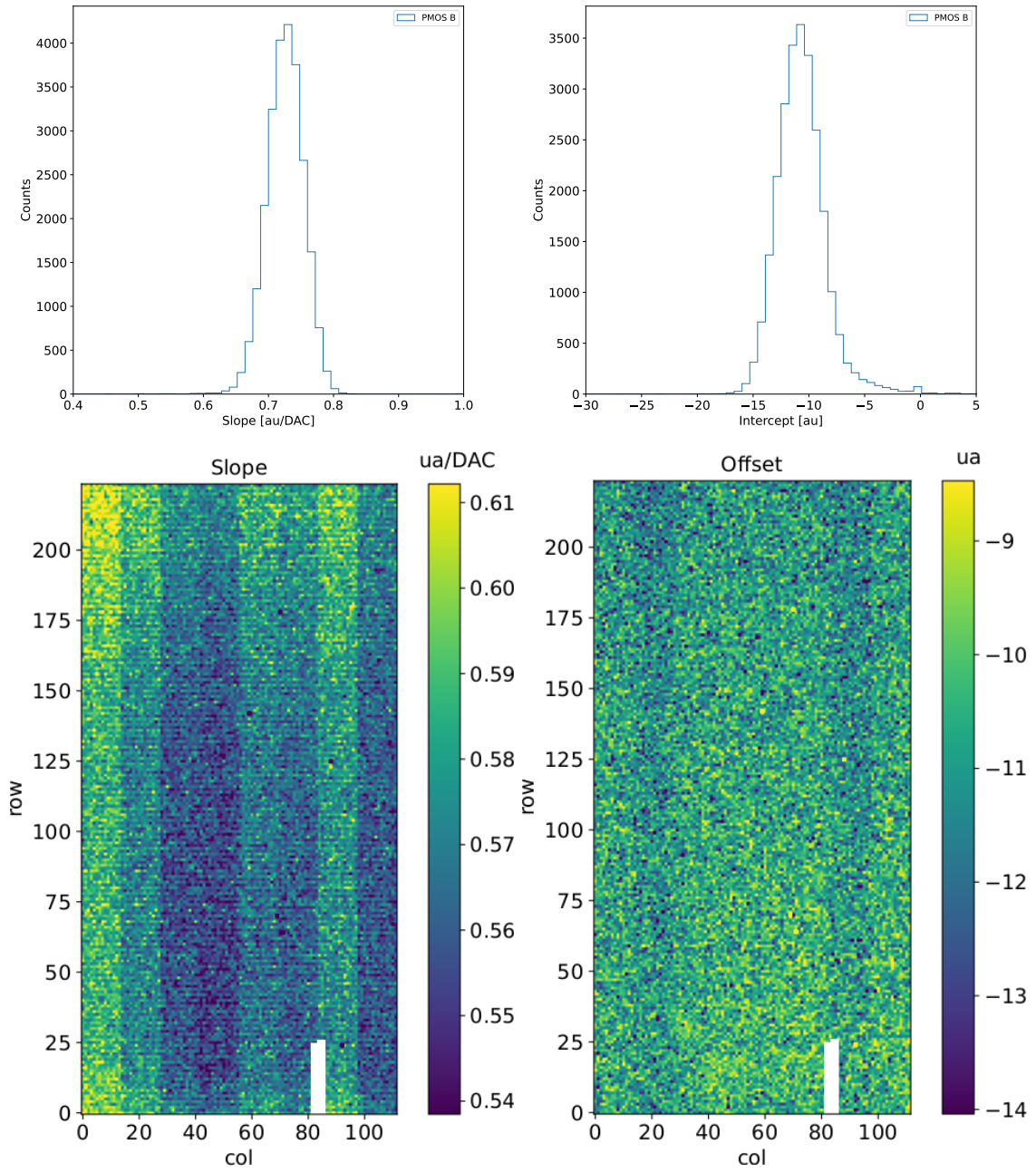


Figure 4.5: Histograms of the calibration parameters, slope (a) and offset (b), found fitting the ToT with a line, for the flavor B and with IDB fixed at 40 DAC. Maps of the calibration parameters, slope (a) and offset (b), found fitting the ToT with a line, with IDB fixed at 40 DAC.

1191 respectively as:

$$K [e^- / DAC] = \frac{1616 [e^-]}{Q [DAC]} \quad (4.6)$$

1192

$$C [F] = [e^- / DAC] \frac{1.6 \cdot 10^{-19} [C]}{14.7 [mV]} \quad (4.7)$$

1193 where K is expected to be $20 e^- / DAC$, assuming the nominal value of C equal to $230 aF$,
1194 and where 1616 is the expected number of electrons produced by the calibration source

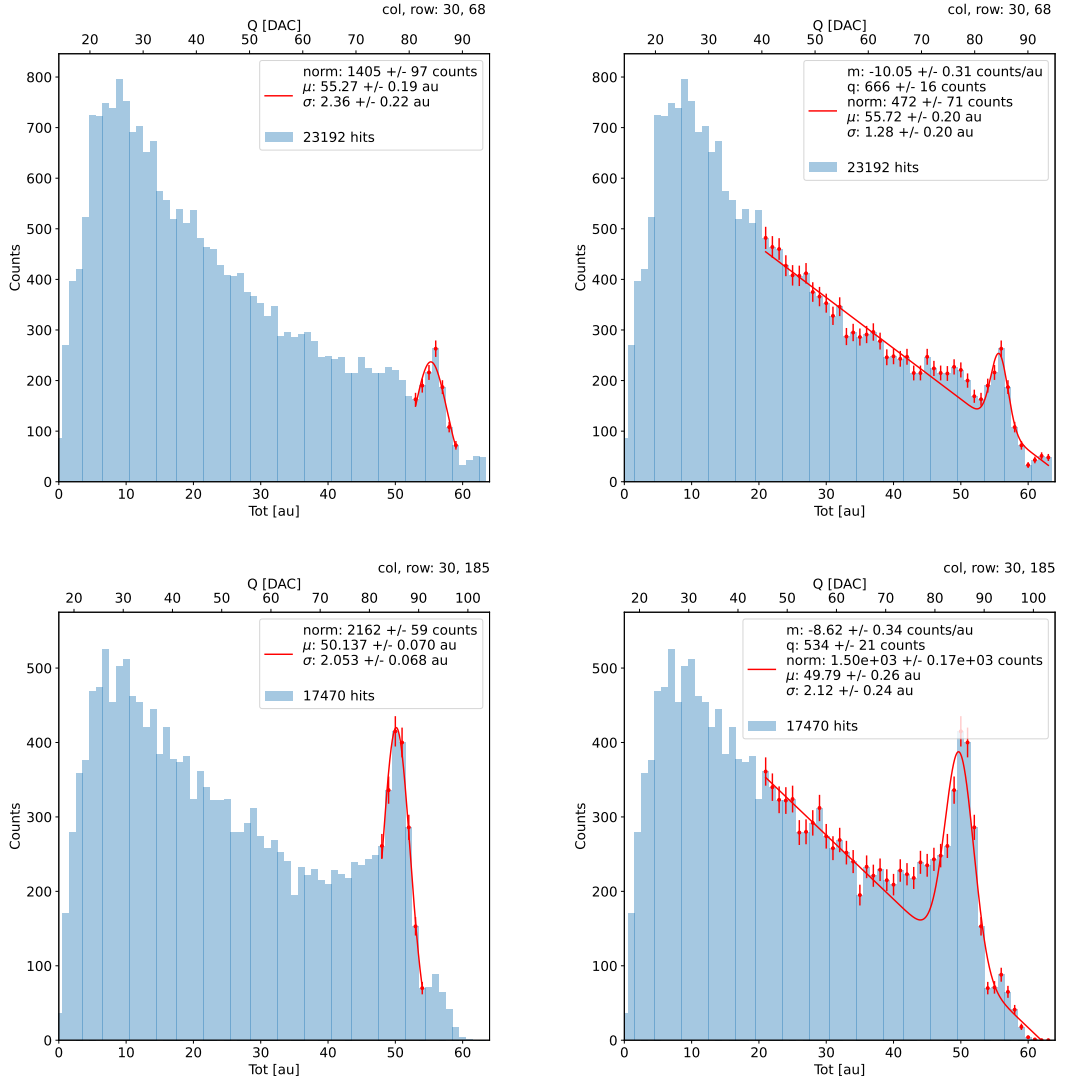


Figure 4.6: due pixel per far vedere la differenza tra i fit. Sottolinea che in rosso ci sono i bin fittati. La doppia scala utilizza le info trovate nel paragrafo precedente per il dato pixel in questione. Per avere una corrispondenza grezza in elettroni basta moltiplicare per 20 e- / dac.

1195 used, Fe55. Fe55 is an extremely important radionuclide in the calibration of X-ray spec-
 1196 trometers, proportional counter and scintillator detector since it emits two X-photons
 1197 during the electron capture decay: the first one (K_{α}) at 5.9 keV and the second one (K_{β})
 1198 at 6.5 keV. The K_{α} photon, which does photoelectric effect in silicon, has an absorption
 1199 length $\lambda=7 \mu\text{m}$ to $8 \mu\text{m}$, and the probability of being absorbed in the $25 \mu\text{m}$ thick epitaxial
 1200 layer is $\sim 0.95\%$. The electron emitted has an energy equal to the photon, so recalling
 1201 that the mean energy needed to produce a couple electron-vacuum is 3.65 eV, the signal
 1202 produced by the Fe55 source is expected to be 1616 e- . In figures 4.6 are shown two
 1203 histograms of the ToT spectrum of the Fe55 source for two different pixels. The peak on
 1204 the right corresponds to the events with complete absorption of the charge in the depleted
 1205 region, while the long tail on the left to all the events with partial absorption due to charge
 1206 sharing among neighbors pixels. In order to reduce the consistent charge sharing, the pixel
 1207 dimension in TJ-Monopix2 has been reduced down to $30 \times 30 \mu\text{m}^2$. The events on the right

side of the peak, instead, corresponds to the K_β photons. Looking at the histograms for pixel (30, 185) and (30, 69) a significant difference in the peak to tail ratio leaps out, which can be related with the position of the pixel in the matrix. In particular, because of a different charge collection property, pixels in the upper part of the matrix (rows 112-224) have a more prominent peak, while in pixels in the lower part (rows 0-111) there is a higher partial absorption. Indeed, as discussed in section ??, there is a distinction in the structure of the low dose-epi layer among the rows, in particular pixels in rows 112-224, which have a RDPW, are supposed to have a higher efficiency in the pixel corner.

For the calibration I needed to establish the peak position; to do that I fitted the ToT histogram of each pixel. I tested two different fit functions:

$$f(x, N, \mu, \sigma) = \frac{N}{\sigma\sqrt{2\pi}} e^{-\frac{1}{2}(\frac{(x-\mu)}{\sigma})^2} \quad (4.8)$$

1218

$$f(x, m, q, N, \mu, \sigma) = m x + q + \frac{N}{\sigma\sqrt{2\pi}} e^{-\frac{1}{2}(\frac{(x-\mu)}{\sigma})^2} \quad (4.9)$$

The additional linear term in equation 4.9 is meant to model the tail due to incomplete

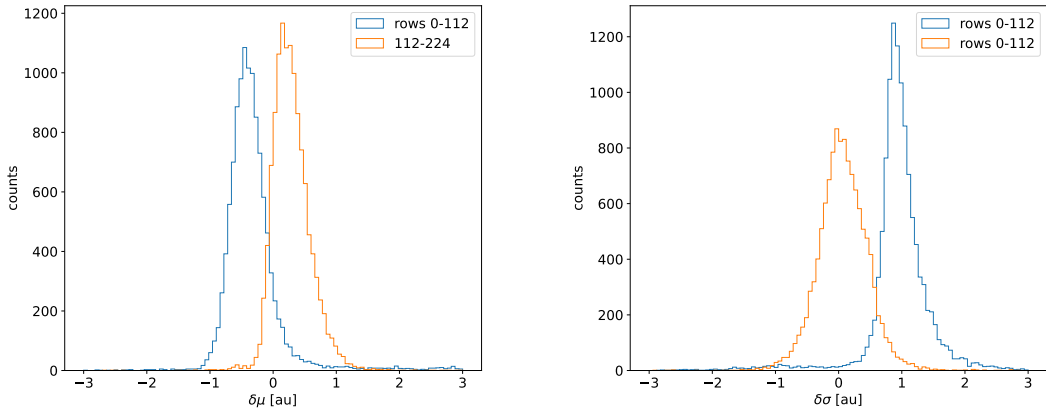


Figure 4.7: Difference between the parameters μ and σ obtained with the gaussian fit and those obtained with a gaussian plus a line. When $\mu < 0$ the fit with function 4.8 is generally worse (the peak is shifted to the left); when $\sigma < 0$, the fit with 4.9 is worse (larger sigma).

1219

charge collection and prevent it from introducing a bias in the fitted peak position.

1220

For this reason, when fitting with eq.4.9, I selected a larger region compared to the fit with eq.4.8, for which I used only a small reagion around the peak. The optimal fit region was chosen in both cases through an iterative routine: for the fit with eq.4.9 it starts from an interval including all the pixels above 20 DAC and progressively reduces it by increasing the left boundary; for the fit with eq.4.8, it starts from an interval of 5 bins around the expected peak position and reduces the interval of 1 bin at each iteration.

1221

Even if the difference in the peak position between the two fit strategies is not really relevant for the purpose of the calibration, being of the order of 0.8-1.5% (4.7),it still introduces a systematic bias towards lower values due to the contribution of the tail. Indeed, we know that the sharp edge on the right must correspond to the case of complete absorption of the photon, so that, in general, the closest to this feature is the fitted peak position, the better the fit is. A poor fit tends also to overestimate the peak width. Even

looking at the χ^2 , the fit function 4.8 seems to be the better choice, except for a sample of pixels in the lower part of the matrix, the one with lower efficiency.

The resolution of the detector, which is expected to be determined by the statistical fluctuations in the number of charge carriers generated in the detector as well as by the ENC, can be compared to the observed Fe55 peak width. Ideally:

$$\sigma_{Fe} = \sqrt{ENC^2 + F \times N} \quad (4.10)$$

Since the number of e/h pairs produced in the sensor is 1616, recalling that F for a silicon detector is 0.115 and that the ENC measured with the injection is 12e^- , the σ_{Fe} is expected to be $\sim 18\text{e}^-$. Looking at figure 4.8 the resolution achieved with the Fe55 source seems to be much higher. A contribution we have not taken into account but is certainly relevant is the systematic overestimation of the standard deviation of the Fe55 peak: this, as I already explained, is principally due to the high background of incomplete charge collection, which broadens the fitted peak.

2D maps of the value of the capacity and of the conversion factor found are shown in 4.9. The evident stripe-structure in the matrix shows an evident correlation among the same row; the same structure, which is also visible in the slope map of the calibration of the ToT (fig.1.3), may be related with the structure of the bias lines.

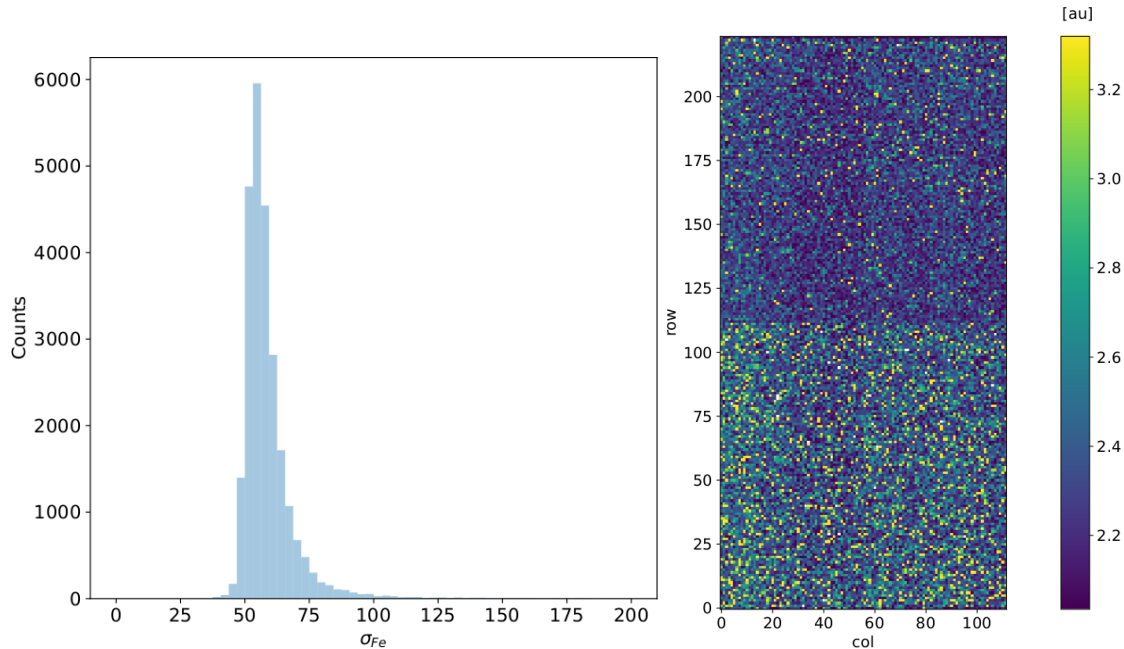


Figure 4.8: Histogram (a) and map (b) of the fitted Fe55 peak width.

1248

1249 HV flavor calibration

An attempt of calibrating the HV flavor, which is the most different from the PMOS B flavor, has been performed; however, because of the loss of signal caused by the higher capacity, we have been unable to identify the Fe55 peak in every FE and bias configuration. An example of Fe55 spectrum collected with the HV flavor is shown in figure 4.10.

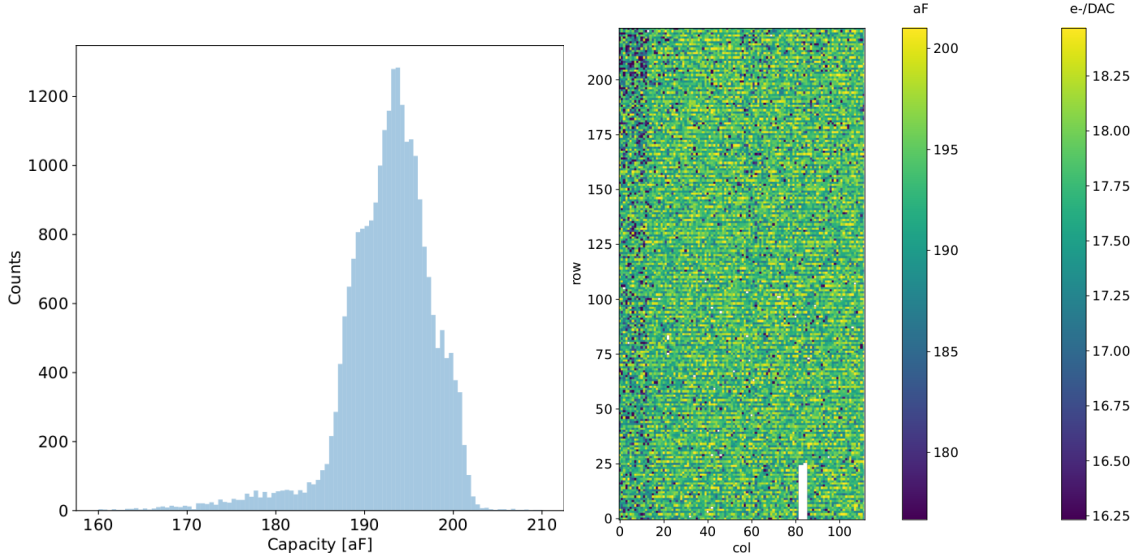


Figure 4.9: Histogram (a) and map (b) of the calibrated capacity of the injection circuit.

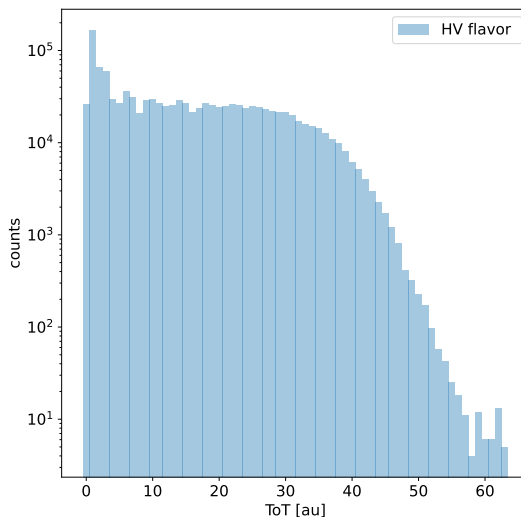


Figure 4.10: Fe55 spectrum with the HV flavor

1254 4.1.4 Changing the bias

1255 In order to study the behavior of the sensor as a function of the bias, I performed several
 1256 injection scans in different configurations. Indeed, the thickness of the depletion region has
 1257 to be considered an important parameters affecting the signal efficiency, and in particular
 1258 it affects the charge released by a particle which crosses the sensor (since the signal is
 1259 proportional to the thickness of the epitaxial layer). The measured output voltage ampli-
 1260 tude and gain in the case of the PMOS and HV flavours are shown in figure 4.11 Given
 1261 that the chip under examination has a gap in the low dose epi-layer, we were not able to
 1262 change independently the bias of the substrate (PSUB) and of the p-well (PWELL), but
 1263 they must be kept at the same value, differently from other chips of the same submission.
 1264 Lowering the bias, the depletion region is expected to narrow and the efficiency to reduce,

	-6 V	-3 V	0 V
Threshold [DAC]	20.0 ± 1.6	21.0 ± 1.6	24.5 ± 1.8
Noise [DAC]	0.613 ± 0.075	0.625 ± 0.078	0.822 ± 0.098
Slope [au/DAC]	0.726 ± 0.027	0.707 ± 0.028	0.573 ± 0.021
Offset [au]	-10.8 ± 1.9	-11.2 ± 1.8	-11.1 ± 1.5

Table 4.2: The errors are the standard deviations of the corresponding distributions. The conversion factor from DAC to electrons is $\sim 20 \text{ e}^-/\text{DAC}$.

1265 especially in the pixel corner, thus raising the threshold and the noise and decreasing the slope as a consequence of the reduction in the gain.

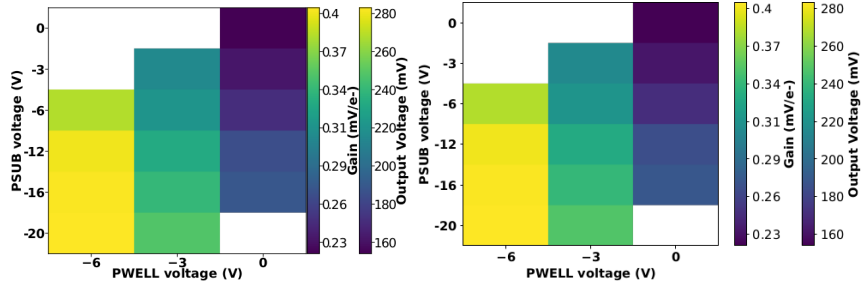


Figure 4.11: Output voltage amplitude and gain with respect to the p-well and p-substrate voltage in the case of the PMOS reset front-end (B)

1266
1267 In order to test the behavior of the chip when not completely depleted, I have performed
1268 an injection scan with PSUB/PWELL bias at 0 V, -3 V and -6 V (results in tab.4.2), and
1269 some acquisitions with the Fe55 source (fig. 4.12). There are reported the values of the
1270 K_α peak position, the normalization of the events above the peak and the rate, everything
1271 has been normalized to the value at the reference condition, which is with PSUB/PWELL
1272 at -6 V.

1273 4.1.5 Measurements with radioactive sources

1274 In order to completely validate the operation of the whole sensor¹, I have performed several
1275 acquisitions with radioactive sources, specifically Fe55 and Sr90Y, which is a β^- emittitor
1276 with electron endpoint at 2.2 MeV, and cosmic rays. I used the data collected with Sr90
1277 and cosmic rays, to study charge sharing and events with more than one hit.

1278 I define *cluster* the ensamble of all the hits with the same timestamp. This is obviously
1279 a coarse requirement, but it gave me the opportunity of using a simple and fast clustering
1280 algorithm, which is fine when the random coincidence probability is neglibile. Defining
1281 R_1 and R_2 as the two events rate, and τ as the dead time of the detector, the random
1282 coincidence rate can be found:

$$R_{coinc} = R_1 \times R_2 \times \tau \quad (4.11)$$

1283 As I am going to prove in the next section, the dead time strictly depends on the occupancy
1284 of the matrix, even though we can assume a dead time of $\sim 1 \mu\text{m}$, which corresponds to

¹As I will discuss in chapter 5.2 these measurements serves also as a reference for the spectrum observed at the test beam

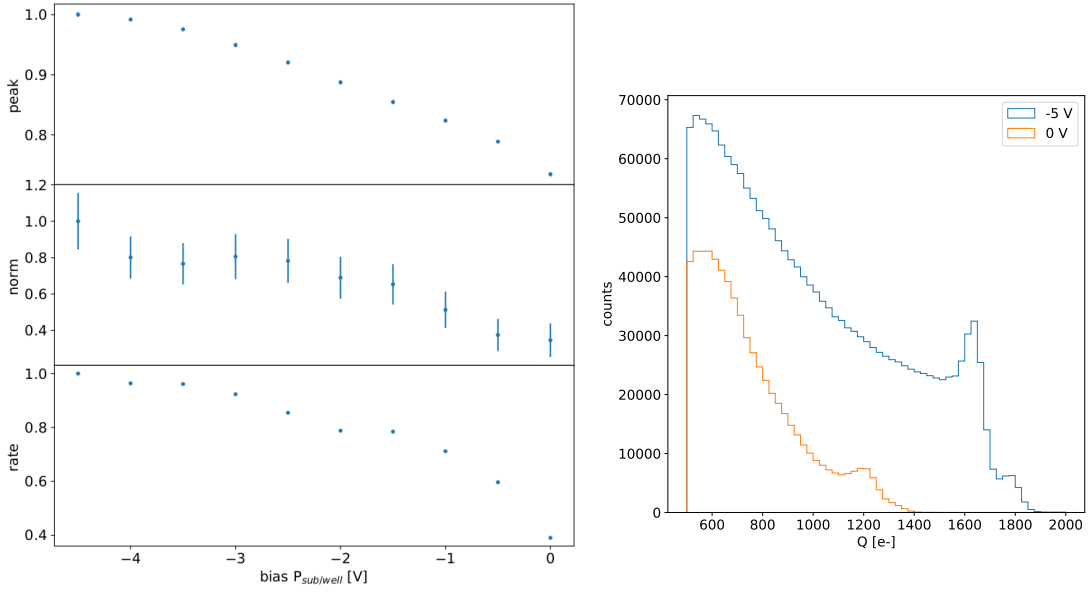


Figure 4.12: (a) Peak position, peak amplitude and rate as a function of the bias. Since during the collection of the whole data the source has been moved, it is not guaranteed that it has always had a repositioning in the same exactly place, then small the fluctuation of the rate along the decreasing trend are acceptable. The peak position and amplitude are estimated by fitting the spectrum with a gaussian in the region around the peak. (b) Fe55 spectrum at different $P_{sub/well}$ bias. The ToT values have been calibrated as explained in section. 4.1.3.

1285 the mean dead time per pixel. However, if in an event a particle hits two different pixels
 1286 producing a cluster, the total dead time simply doubles. Since the measured rate on the
 1287 whole matrix of noise, Fe55, Sr90 and cosmic rays are \sim Hz, 3.3 kHz, 40 Hz and \sim 10 mHz²,
 1288 the random coincidence probability are negligible except the one of two Fe55 events, which
 1289 is 11 Hz.

1290 In figure 4.13 I report the histograms of the number of pixels in the cluster and of the
 1291 dimension of clusters, defined in terms of the max and min coordinates on the matrix as:

$$d = \sqrt{(y_{max} - y_{min})^2 + (x_{max} - x_{min})^2} \quad (4.12)$$

1292 Looking at the shape of the histogram of the dimension, generally the Sr90 and the
 1293 cosmic rays produce bigger clusters and hit a higher number of pixels, a trend that can
 1294 be explained considering that the Fe55 photoelectron is much less energetic than the Sr90
 1295 electron and cosmic rays. Below I have also attached a sample of hitmap of events produced
 1296 by the three different sources (fig.4.14, 4.15).

1297 In figures 4.18, 4.19, 4.21 are shown the distributions per different cluster dimension
 1298 events, of the charge collected by a single pixel (figures on the left) and the charge collected
 1299 by summing the charge collected by the pixels within the cluster (figures on the right).
 1300 Since the noise rate is comparable with the cosmic rays and Sr90 ones, I have removed the
 1301 single pixel events which are separately shown in figure 4.17; despite we cannot identify
 1302 and selecting only the noise events, these distributions, and especially the cosmic rays
 1303 one, are expected to be mostly populated by noise events. The distributions have a peak

²The cosmic rays rate at the sea level is expected to be \sim 1/cm²/s

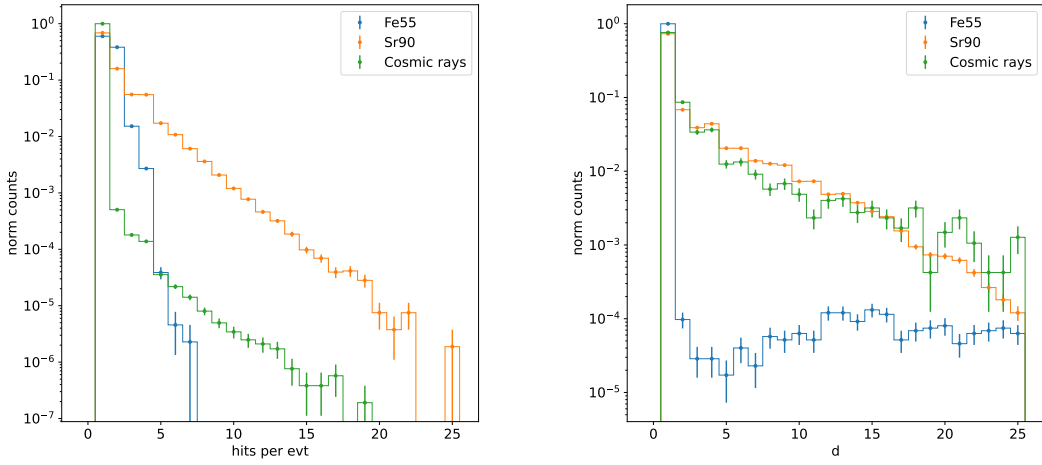


Figure 4.13: (a) Distribution of the number of hits per event with different sources. (b) Dimension of cluster defined as eq.4.1.5. Compared with the Sr90 and the cosmic rays, the Fe55 d distribution is characterized by a clear discontinuity in the cluster dimension. The very thin peak around 0 corresponds to the effective cluster, while the long tail at bigger cluster d is principally made of random coincidence.

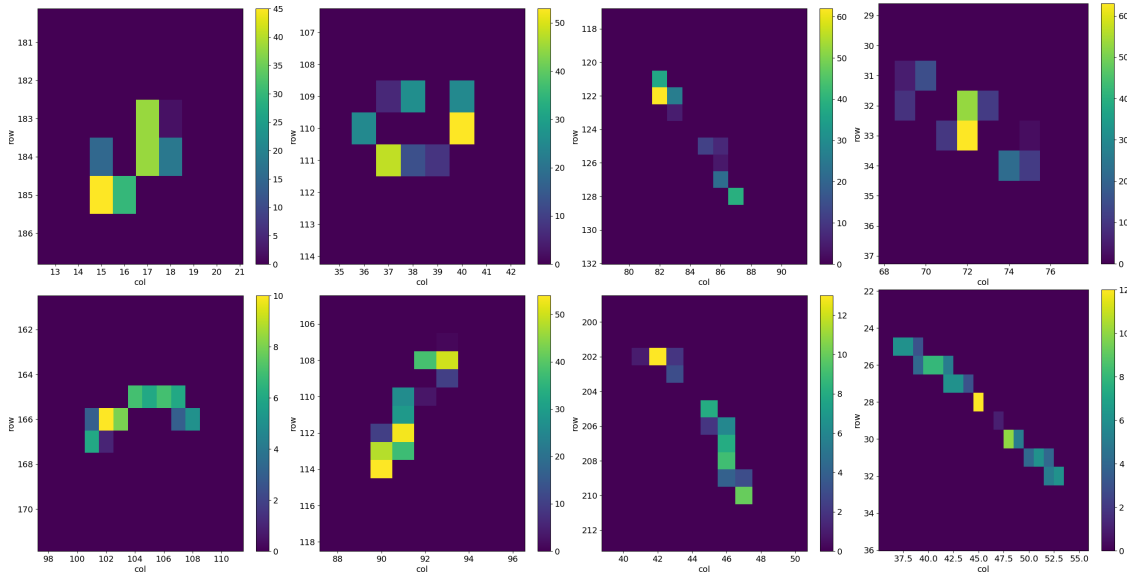


Figure 4.14: 2D histograms of the ToT in different events in an acquisition of cosmic rays.

1304 around the threshold, which is compatible with the fact that the noise events typically
1305 have a low ToT.

1306 Looking at the spectra of Sr90 instead (fig:4.19), the maximum of the distribution of
1307 the cluster charge seems to follow a linear dependence on the number of pixels hit (tab.4.3);
1308 this can be accepted as a first approximation considering that the pitch ($36 \mu\text{m}$ and $40 \mu\text{m}$)
1309 depending on the direction, and the epitaxial layer thickness ($25\text{-}30 \mu\text{m}$) are comparable.
1310 However a more accurate model which takes into account the impact angle of the particle
1311 should be developed for a more precise comparison. The charge per length covered Q/l
1312 released by a particle which crosses more pixels and is not completely absorbed in the

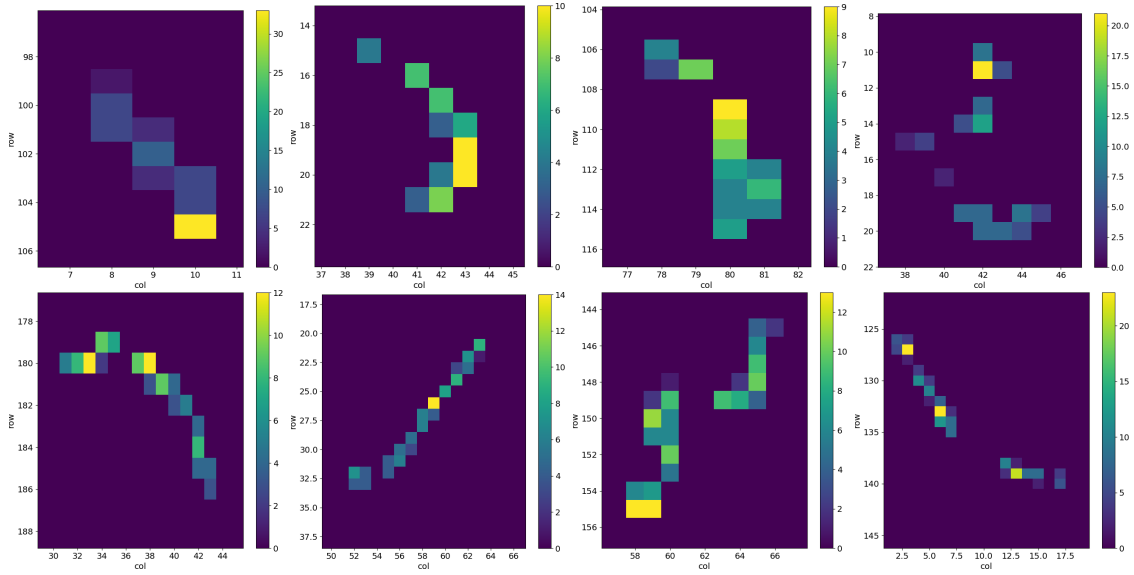


Figure 4.15: 2D histograms of the ToT in different events in an aquistion of Sr90.

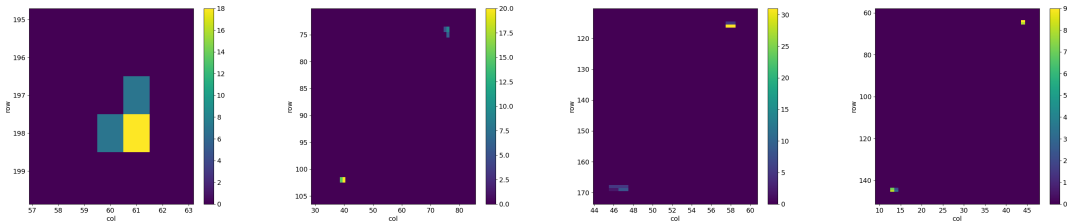


Figure 4.16: 2D histograms of the ToT in different events in an aquistion of Fe55

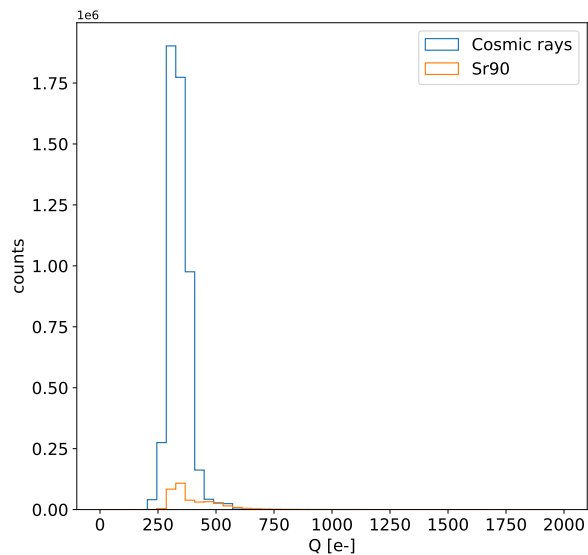


Figure 4.17: Histograms of the charge released in the pixels in events in which only a single pixel turns on.

Pixel per evt	Measured [e-]
2	950 ± 30
3	1450 ± 30
4	2050 ± 30
5	2450 ± 30

Table 4.3: Position of the maximum of the distributions in figure 4.19(b) of the summed charge released in the clusters depending on the number of pixel in the cluster.

1313 sensor (fig.??) can be described by the following relation. Considering that:

$$l = \frac{t}{\cos(\lambda)} = \frac{t}{\sqrt{1 + tg^2\lambda}} = \frac{t}{\sqrt{1 + (x/t)^2}} \quad (4.13)$$

1314 it can be expressed as:

$$\frac{Q}{l} = \frac{Q}{t} \sqrt{1 + (n - 1)^2 p^2 / t^2} \quad (4.14)$$

1315 where p/t is the ratio between the pitch and the epitaxial layer thickness, and then it
1316 is different in the x and y directions ($40 \mu\text{m}$ and $36 \mu\text{m}$ respectively). Taking as value of
1317 p/t 1.52, which is the mean on the two axis, the value of Q/l expected by the scaling
1318 relation and the charge actually measured in the acquisition with the Sr90 are illustrated
1319 in table 4.3; because of the decision of cutting the single pixel events in order to have
1320 a clean sample, the expected value has been obtained by the two hits cluster dividing
1321 the charge by 2. By the inversion of the formula ??, the single pixel charge is then
1322 expected to be 522 e-. FORSE DATO CHE LA MASSIMA CARICA RILASCIATA
1323 SCALA LINEARMENTE CON IL NUMERO DI PIXEL NON SCRIVEREI QUESTA
1324 COSA? O MAGARI LA METTO COME CORREZIONE? The measured value has been
1325 obtained by the maximum of the distributions in the left plots in ??

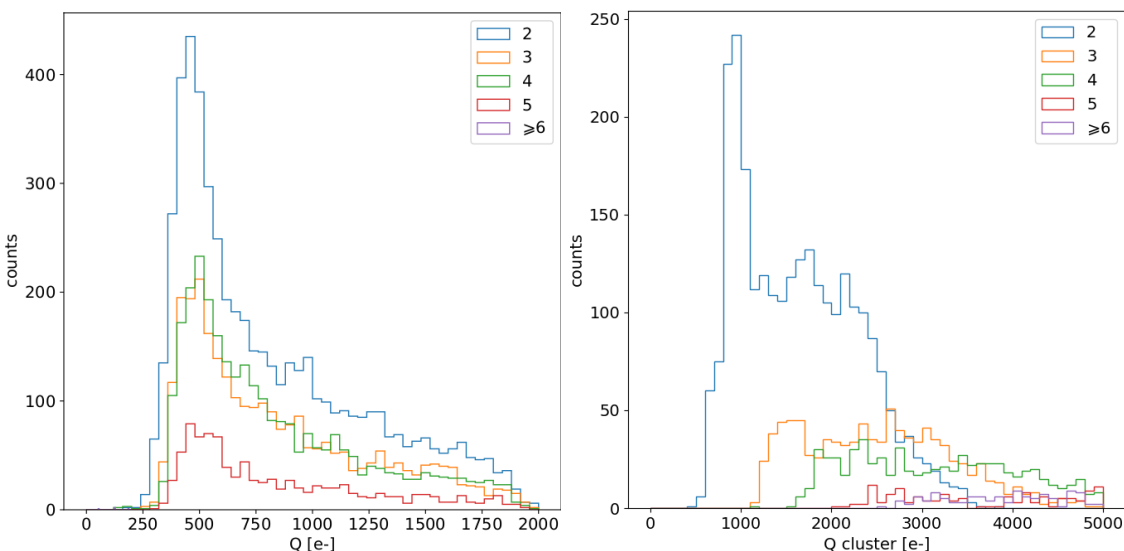


Figure 4.18: Acquisition of cosmic rays with IDB=40 DAC

1326 Regarding the Fe55, the bump in the cluster spectrum at $\sim 1616 \text{ e-}$ corresponds to
1327 photons which had converted at the boundary of nearby pixels thus sharing their charge
1328 among them. Starting from 4-pixels clusters the peak moves to the right: this is due to

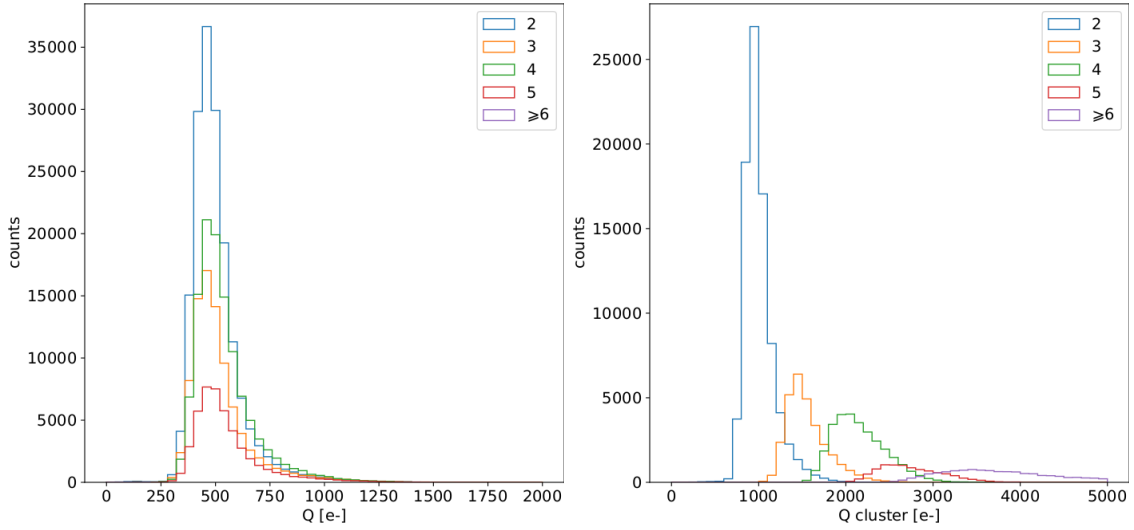


Figure 4.19: Acquisition of Sr90 with IDB=40 DAC

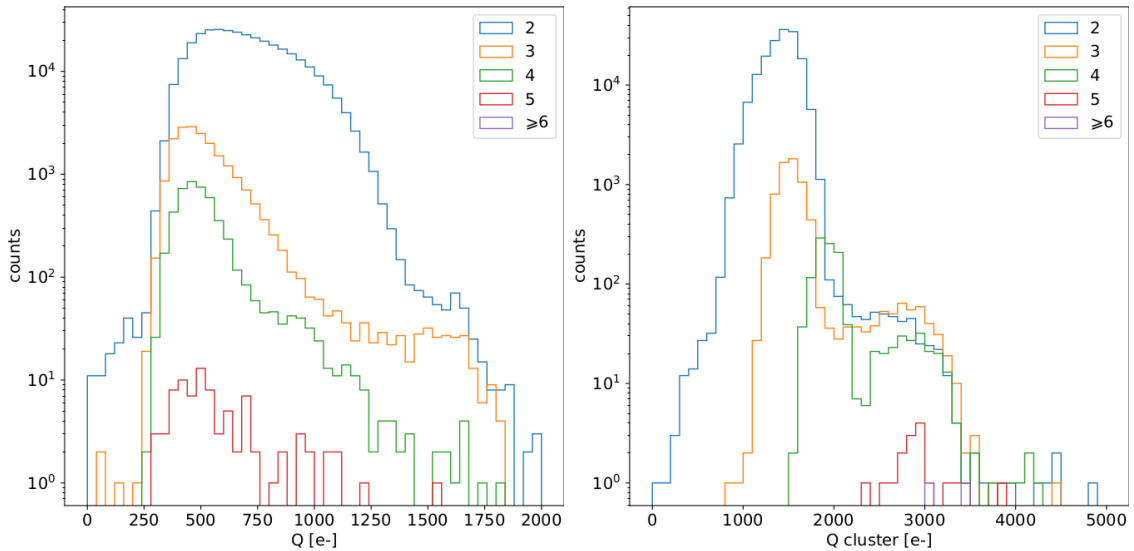


Figure 4.20: Acquisitions with radioactive source and cosmic rays at IDB=40 DAC.

Figure 4.21: Acquisition of Fe55 with IDB=40 DAC

the fact that the cluster with more than 3 pixels are principally random coincidence events Fe55-Fe55 or Fe55-noise. Recalling that the noise typically just exceeds the threshold and then has low ToT, the peak position in the spectrum 1.3 of 4-pixel cluster can be explained admitting that one of the four pixel is a noise signal. The shoulder on the right, instead, which have an edge at about 3200 e⁻ corresponds to the events with coincidence of two photons. Looking at the charge on the single pixel spectrum (fig.1.3), instead, a small bump can be seen around 1616 e⁻: these events correspond to photons which released almost all the charge on one pixel.

4.1.6 Dead time measurements

The hit loss is due to analog and digital pile up: the first one occurs when a new hit arrives during the pre-amplifier response, the second instead when the hit arrives while

1340 the information of the previous hit has not yet been transferred to the periphery. Since the
 1341 pre-amplifier response has a characteristic time \sim ToT, the dead time τ_a introduced by it
 1342 will be at most 1.6 μ s; using the IRESET and VRESET FE parameters the reset time can
 1343 be lowered down, but as explained in section ?? it must be longer than the preamplifier
 1344 characteristics time in order to not cut the signal. Regarding the latter contribution instead,
 1345 since only one hit at a time can be stored on the pixel's RAM, until the data have completed
 1346 the path to get out, the pixel is paralyzed. Moreover since there is no storage memory
 1347 included on TJ-Monopix1 prototypes, the digital dead time τ_d almost corresponds to the
 1348 time needed to trasmit the data-packets off-chip.

1349 The exportation of data from pixel to the EoC occurs via a 21-bits data bus, therefore
 1350 only one clock cycle is needed and the dead time bottleneck is rather given by the
 1351 bandwidth of the serializer which trasmits data off-chip from the EoC. In our setup the
 1352 serializer operates at 40 MHz, thus to transmit a data packet (27-bit considering the ad-
 1353 dition of 6 bits to identify the double-column at the EoC) at least 675 ns are needed. For
 1354 what we have said so far, the R/O is completely sequential and therefore is expected a
 1355 linear dependence of the reading time on the number of pixels to read:

$$\tau = 25 \text{ ns} \times (\alpha N + \beta) \quad (4.15)$$

1356 where α and β are parameters dependent on the readout chain setting.

1357 To test the linearity of the reading time with the number of pixels firing and to measure
 1358 it, I have used the injection circuit which allows me choosing a specific hit rate: I made
 1359 a scan injecting a fix number of pulses and each time changing the number of pixels
 1360 injected. Indeed the injection mode allows fixing not only the amplitude of the pulse,
 1361 which corresponds to the charge in DAC units, but also the time between two consecutive
 1362 pulses (DELAY). The hit rate then corresponds to 25 ns/DELAY.

1363 Unfortunately a high random hit rate on the matrix cannot be simulated by the in-
 1364 jection because of the long time (\sim ms) needed to set the pixel registers of the injection;
 1365 then I was forced to specify at the start of the acquisition the pixels to inject on, and for
 1366 convenience I chose those on a same column. In figure 4.22 is shown the dependence of
 1367 the efficiency on the DELAY parameter in two different cases. For the 5 pixels example
 1368 the efficiency goes down the 90% at a DELAY of \sim 185 clock counts, which corresponds
 1369 to 4.625 μ s and to a rate of 216 kHz, while in the 10 pixels example, the efficiency goes
 1370 under the 100% at \sim 380 clock counts, which corresponds to 9.5 μ s and to a rate of 105 kHz.
 1371 From the efficiency curves I have then looked for the time when the efficency decreases.
 1372 In figure 4.23(a) is shown the dead time per pixels as a function of N with different R/O
 1373 parameters configuration, the meaning of which is explained in chapter 3.3. The default
 1374 value suggested by the designer of the chip are reported in table 4.4; moving too much
 1375 the readout parameters from the default ones, the readout does not work properly, and no
 1376 hits can be read at all. The problem probably stays in the firmware setting of the readout
 1377 which are specially fixed for our chip **Sul repository, nei commenti ci sono altri valori pos-
 1378 sibili per il FREEZE, ma avevamo detto che probabilmente sono relativi ai setting di altri
 1379 chip.** Despite the single pixel reading time does not depend on the position on the pixel
 1380 matrix, whithin a clock count which is \sim 25 ns, and it is equal to 106 clock counts, since
 1381 the τ_d critically depends on the pixel position on the matrix: in particular the reading
 1382 sequence goes from row 224 to row 0, and from column 0 to column 112, making the pixel
 1383 on the bottom right corner the one with the longest dead time.

1384 Furthermore to test that there is no dependece of the digital readout time from the

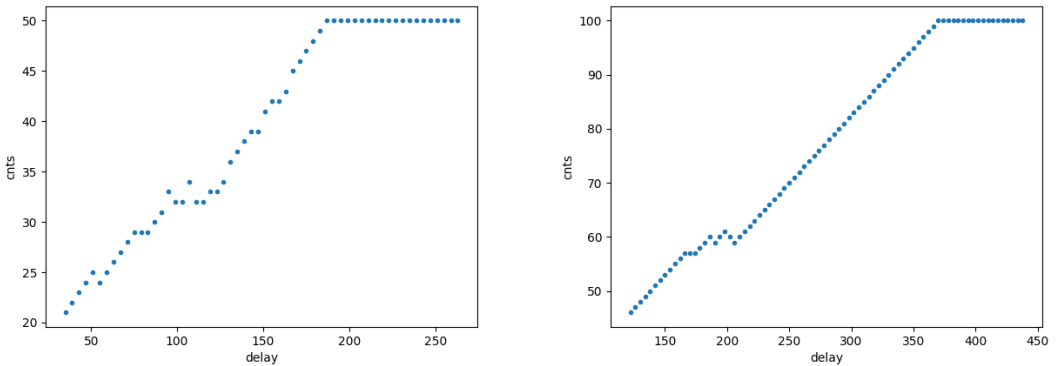


Figure 4.22: Efficiency vs the DELAY parameters. (a) I made a scan injecting 5 pixels with 50 pulses for each DELAY configuration and (b) 10 pixels with 100 pulses for each DELAY

Parameter	Value [DAC]	Value [μ s]
START_FREEZE	64	1.6
STOP_FREEZE	100	2.5
START_READ	66	1.65
STOP_READ	68	1.7

Table 4.4: Default configuration of the R/O parameters

charge of the pulse, I have try to change the amplitude of the pulse injected, but the parameters found were consistent with the default configuration ones. No difference in the α and β coefficients has been observed between the two case. Referring to eq.4.15, the factor α is proportional to the difference (STOP_FREEZE - START_READ), while the offset β lies between 5 and 15 clock counts.

The readout time found by this test is so long because in the prototypes no parallelization of the informations (with the instruction of more serializer for example) and no storage memory are included; this feature are typically added in the final prototypes. An example closely linked to TJ-Monopix1 is OBELIX: it will include on the chip a storage buffer to optimize the dead time and to keep a low occupancy even at high fluence.

4.2 ARCADIA-MD1 characterization

Unfortunatly the characterization of MD1 has not yet been completed because of some problems with the functionality of the first chip we received on which we have been able to make only a few electrical and communication test in order to test the operations of the FPGA and the breakount board (BB). We asked for another chip then but we, due to delay in the extraction and the bonding of the wafer, have received it one week ago; an exhaustive characterization and testing of the new chip have been going on in the clean room on the INFN, and I am going to show here only some preliminary results.

The problem with the broken chip occurs when it is biased, in particular, when the HV voltage is lowered down 0V, the sensor requires too much power and a too high current draw sets. We have discussed the problem with the designers of the chip whose helped

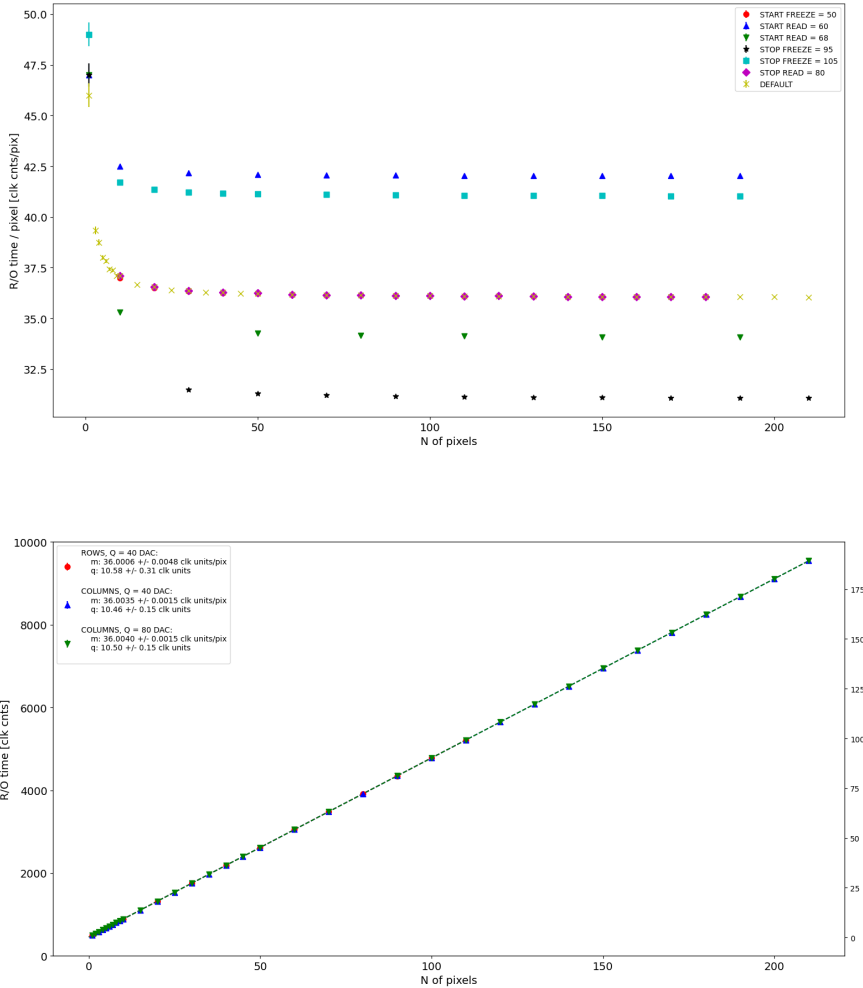


Figure 4.23: (a) Readout time per pixel as a function of the number of pixel injected obtained with different FE setup. (b) Readout time as a function of the number of pixels injected obtained injecting pulses with amplitude of 80 DAC (green), of 40 DAC on the same row (red) and on the same column (blue).

us indentifying the motivation of the break: the chip has been glued using too much conductive tape and hence have a short-circuit between the sides and the back, which makes impossible the biasing. Unfortunately, since both the sensor and the FE require at least -10 V to work properly, no measurement was possible except the acquisition of the noise in the FE circuit.

The second chip we received is a minid2, that is a "mini demonstrator" from the second submission. The two have the same charateristics but the minid2 is smaller than the MD1, in particular it only have 32×512 pixels, instead of 512×512 .

Up to now we used the injection circuit in order to make a threshold scan on a few pixels: differently from the TJ-Monopix1's charaterization where we performed a scan changing the injection charge of the pulse, with the minid2 we have instead changed the threshold (whose register is VCASN) keeping the charge of the pulse fixed. For each threshold we inject 100 pulses of amplitude $10 \mu\text{s}$. The dependece of the efficiency on the threshold for two pixels is shown in figure 4.25. Even if the behavior is reasonable, as the

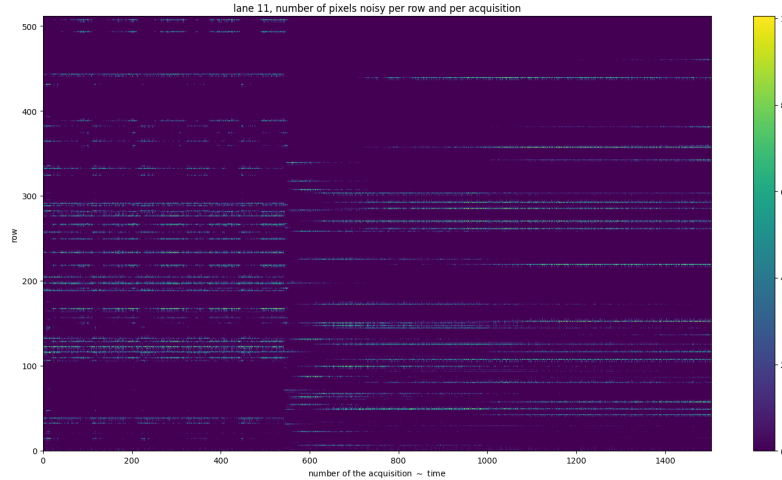


Figure 4.24: Noise in the front end circuit depending on the bias road across the matrix was recorded.

1420 threshold is reduced the efficiency becomes higher, it is possible that the bias (-50 V) is not enough to full deplete the sensor, since the counts does not reach the 100% steadily.

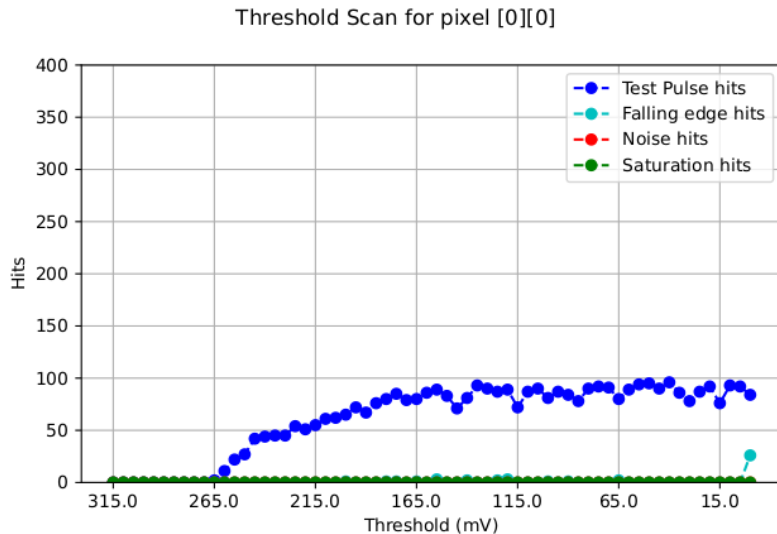


Figure 4.25: Threshold scan on the pixel (0,0). The sensors is polarized with $\Delta V = -50$ V.

1421
1422 The value of the SNR and the ENC Charge injection circuit uses $C_{inj} = 2.325$ fF The
1423 SNR, the ENC and the threshold dispersion on the matrix are expected to be respectively
1424 ~ 90 , $3 e^-$ and $\sim 35 e^-$ with a detector capacity of 7 fF, that is about the capacity expected
1425 for the detector. The injection capacity is expected to be ~ 2.325 fF, and in this condition
1426 the the minimum and maximum signals generated are respectively 0.08 fC and 2.6 fC.

1427 Substantial differences have been observed with VCASN=40 DAC in both the efficiency
1428 and the threshold among the sections; this suggests that with this particular FE config-
1429 uration there is a big threshold dispersion on the matrix. The hitmap of an acquisition
1430 with the Fe55 source is shown in figure 4.26: the whole MD1 matrix with only the bottom
1431 region (32 rows) working is represented in (a), while in (b) there is a zoomed hitmap. The

¹⁴³² rate seen within the region 8 (green region in the figure (a)) is compatible with the rate of the same radioactive source measured with TJ-Monopix1, that it ~ 3.3 kHz. Looking to

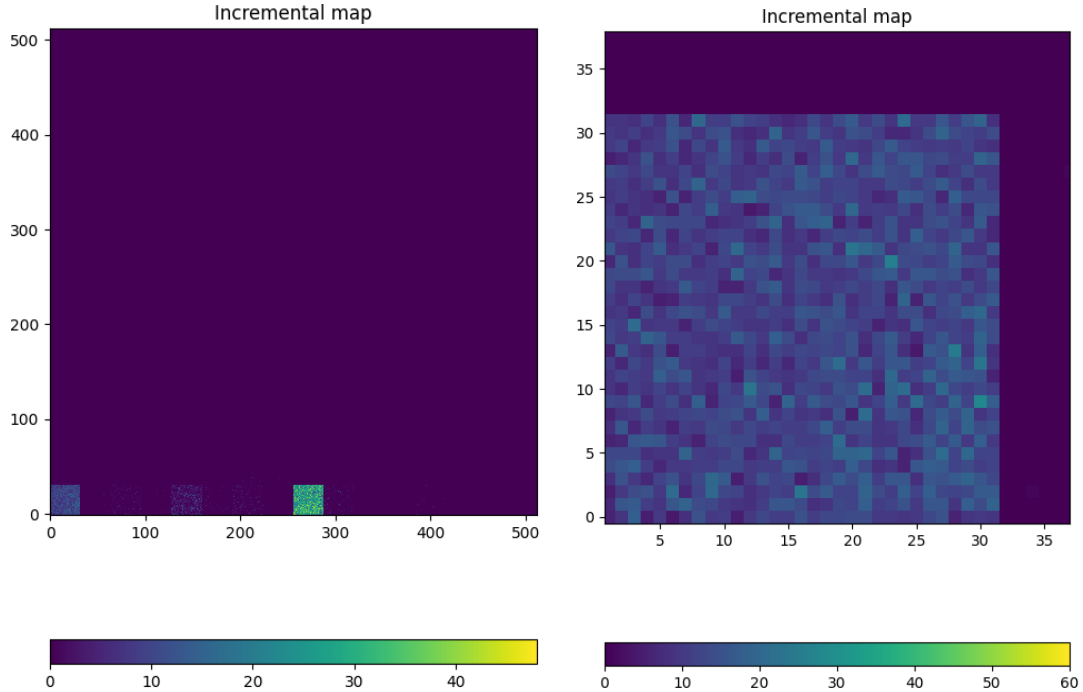


Figure 4.26: Fe55 acquisition with VCASN=40 DAC. (a) All the matrix 512×512 is plotted even if the minid2 has only the rows in range 0-32. (b) A zoom on the first section (col 0-32).

¹⁴³³

¹⁴³⁴ the Sr90 acquisitions (fig.4.27) many clusters and tracks can be immediately distinguished, confirming what observed with TJ-Monopix1.

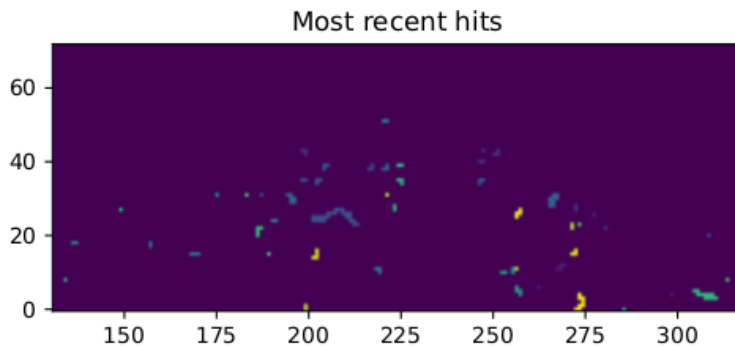


Figure 4.27: Sr90 acquisition with VCASN=40 DAC. The different colours are related with the time of arrival of the hits: in yellow the most recent hits, while in blue the old ones.

¹⁴³⁵

₁₄₃₆ **Chapter 5**

₁₄₃₇ **Test beam measurements**

₁₄₃₈ During August 2022 a testbeam took place in Santa Chiara hospital in Pisa, where a
₁₄₃₉ new accelerator designed for both medical research and R&D on FLASH-RT, and for this
₁₄₄₀ reason called "ElectronFlash", have been installed a few months ago. The motivation
₁₄₄₁ of the testbeam measurements were testing TJ-Mopopix1 at high dose rate with a focus
₁₄₄₂ on investigating the possibility of the application in radiotherapy. Despite this particular
₁₄₄₃ device does not seem fitting the requirements imposed for that application, especially
₁₄₄₄ regarding the readout time, the measurements have been useful since help us characterizing
₁₄₄₅ the setup for future advance, and also give us the possibility of a complete characterization
₁₄₄₆ of the chip.

₁₄₄₇ Given that in medical physics the dose is the standard parameter to characterize the
₁₄₄₈ beam, because of its obvious relation with the damage caused in the patient, I am going
₁₄₄₉ to explain the meaning of it by the point of view of the instrumentation. Infact, when
₁₄₅₀ interacting with measuring systems a more common and useful parameter is the rate or
₁₄₅₁ the fluence of particles. The conversion between the two quantity can be found thinking to
₁₄₅₂ the definition of dose: it is the concentration of energy deposited in tissue as a result of an
₁₄₅₃ exposure to ionizing radiation. Assuming total absorption of electrons in water, defined
₁₄₅₄ by law as the ordinary reference medium, the dose can be expressed as:

$$D[Gy] = \frac{NE[eV]}{\rho[g/cm^3]A[cm^2]x[cm]} \quad (5.1)$$

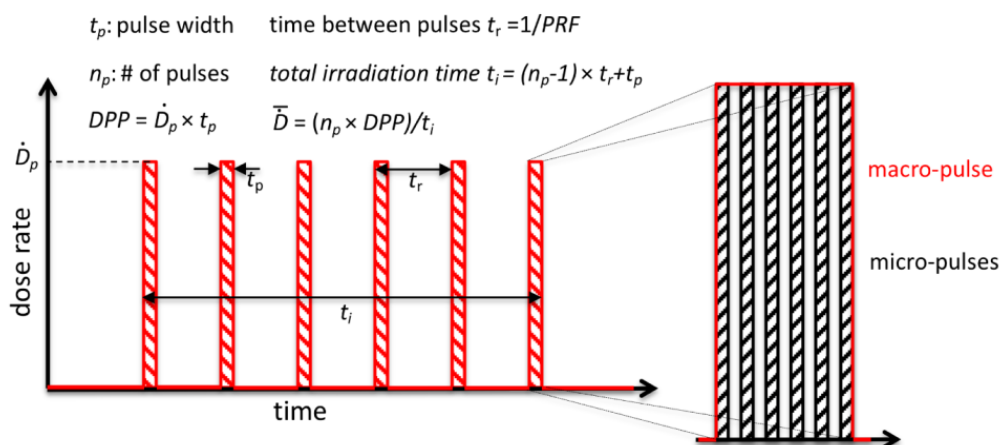


Figure 5.1: Typical beam structure of a beam used in electron radiotherapy

\bar{D}	Dose rate (mean dose rate for a multi-pulse delivery)	0.005-10000 Gy/s
\dot{D}	Intra pulse dose rate (dose rate in a single pulse)	0.01-1 10^6 Gy/s
DDP	Dose in a single pulse	0.04-40 Gy
PRF	Pulse repetition frequency	1-350 Hz
t_p	Pulse width	0.2-4 μ s
n	Number of pulses	single/pulse train

Table 5.1: The parameters that can actually be set by the control unit are the PRF, DDP, t_p and n (in particular the modality of singular irradiation or pulse train), while the other changes consequently.

1455 After having applied the conversion of the energy from eV to J and noticed that $E/\rho x$
 1456 roughly corresponds to the stopping power S of electrons in water, a simple estimation of
 1457 the dose released in water is:

$$D[Gy] = 1.602 \cdot 10^{-10} N[cm^{-2}] S[MeV cm^2/g] \quad (5.2)$$

1458 5.1 Apparatus description

1459 In order to shield the outdoor from ionizing radiation the accelerator is placed in a bunker
 1460 inside the hospital. The bunker has very thick walls of cementum and both the control
 1461 units of the accelerator and of the detector were placed outside in a neighbor room.

1462 5.1.1 Accelerator

1463 The ElectronFlash accelerator is an electron Linear Accelerator (LINAC) with two energy
 1464 configurations, at 7 MeV and 9 MeV, and it can reach ultra high intensity (40 Gy/pulse)
 1465 keeping the possibility of accessing many different beam parameters and changing them
 1466 independently from each other, a characteristic that makes it almost unique worldwide
 1467 and which is fundamental for research in FLASH-RT, both for the medical aspects¹ and
 1468 for the studies on detectors. The accelerator implements the standard beam structure
 1469 used in RT with electrons (fig. 5.1), that is a macro pulse divided in many micropulses;
 1470 the parameters used to set the dose and their range of values settable by the control unit
 1471 is reported in table 5.1.

1472 The accelerator is also provided of a set of triod cannons ~ 1.2 m long and with diameters
 1473 in range from 1 cm to 12 cm and a collimator that can be used as beam shaper to
 1474 produce a squircle shape. The triode, which is made by plexiglass, must be fix to the gun
 1475 during the irradiation and is needed for producing, via the scattering of electrons with it,
 1476 an uniform dose profile (fig.5.2) which is desired for medical purpose.

1477 5.1.2 Mechanical carriers

1478 The tested detector consists in one chip, the Device Under Test (DUT), mounted on
 1479 a board and connected to FPGA with same arrangement of figure 1.3. These boards
 1480 have been positioned vertically in front of the triode on a table specifically built for the

¹For example, it is not yet really clear the dependence of the efficacy of the FLASH effect on the whole beam parameters

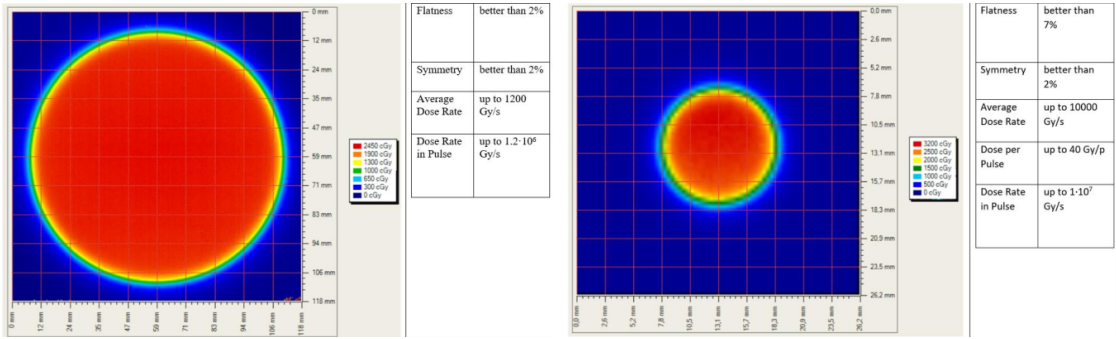


Figure 5.2: Two example of x-y isodose curves for two different triodes, 10 cm and 1 cm respectively, reported by the producer in the manual with the specific of the accelerator (S.I.T. - Sordina IORT Technologies S.p.A.). With the smaller collimator the dose rate in pulse is comparatively higher.

1481 testbeam. The tree board have been enclosed in a box of alluminium with a window on
 1482 the DUT and with the required holes at the side to enable the biasing via cables and the
 1483 connection with the DAQ provided via ethernet cable. A trigger signal coming from the
 1484 control unity and syncronized with the pulses emitted from the beam has been also sent to
 1485 the FPGA. This digital signal cannot be considered a real trigger, since the TJ-Monopix1
 1486 prototype has been designed to be triggerless, but its Time of Arrival (ToA) had allowed
 1487 the reconstruction of the correct timing during the analysis.

1488 In order to shield the sensor from the whole particles emitted from the gun, two
 1489 alluminium collimators have been fabricated: one has been positioned at the triode exit
 1490 while the other in front of the DUT. The collimators are $t=32$ mm thick and have a
 1491 diameter d equal to 1 mm: assuming a beam divergence bigger than $d/t=1/32 = 1.8^\circ$,
 1492 which is the case, the collimator at the triode output was supposed to work as a point
 1493 source and to reduce the rate on the DUT of a factor at least $4 \cdot 10^{-4}$. The second one,
 1494 being near the DUT, was instead supposed to shield the sensor from the electrons which
 1495 have passed the first one, except for a region of 1 mm^2 configurable using **come si chiamano**
 1496 **quei cacciavitini per settare la posizione? sliding trimmer?**.

1497 5.2 Measurements

1498 Because of the dead time of TJ-Monopix1 it is not possible resolving the bunch sub-
 1499 structure and almost no one pixel can read more than a hit per bunch. I recall, indeed,
 1500 that the dead time per pixel depends on the location on the readout priority chain and
 1501 for each pixel $\lesssim 1 \mu\text{s}$ are needed; therefore, assuming a pulse duration of $4 \mu\text{s}$, only a few
 1502 pixels at the top of the priority chain (placed at the upper left on the matrix) can fire a
 1503 second time, as they can be read a first time before the end of the pulse and then can be
 1504 hit again.

1505 Since resolving the single electron track is impossible, a way this sensor could be used
 1506 in such context is reducing its efficiency and taking advantage of the analog pile up and
 1507 of the linearity of the analog output (ToT), in order to see a signal produced not by the
 1508 single particle but by more electrons. Reducing the efficiency and the sensibility of the
 1509 sensor is essential in order to decrease the high charge signal produced in the epitaxial
 1510 layer and mitigating the saturation limit: the smaller the output signal produced by a

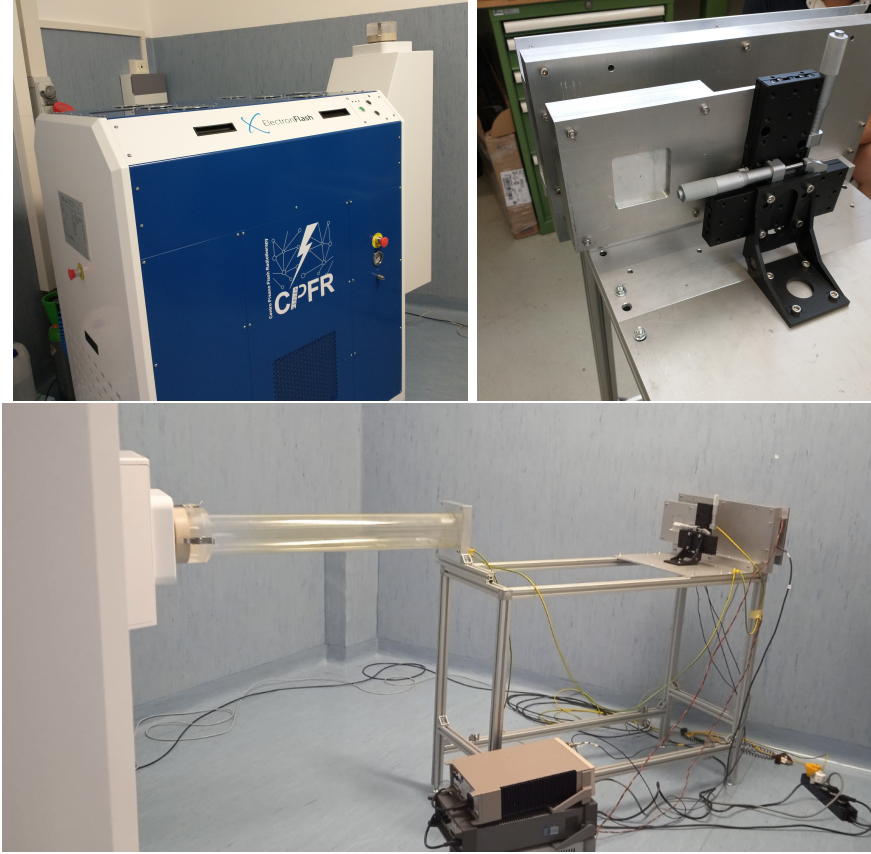


Figure 5.3: Experimental set up. (a) ElectronFlash accelerator: a rotating gantry allows the gun orientation from 0° to 90° (horizontal /vertical). (b) Collimator and DUT box. (c) Whole structure mounted: we used the 10 cm diameter and 1.2 m long triode; the DUT which is in the box behind the two collimators is connected to the power supply units.

1511 particle and the higher the fluence the detector can cope with. There is an obvious limit in
 1512 this context that is the ToT rollover, indeed, the signal stop giving information when this
 1513 value has been overridden and is no more bijective. With the standard configuration of
 1514 the FE parameters and the epitaxial layer completely depleted, a MIP produces a charge
 1515 at the limit of representation with a 6-bit ToT; to obtain smaller output signals one can
 1516 operate on the reduction of the gain.

1517 Recalling the results in section 4.1.4, I have shown that concerning the PMOS flavor
 1518 B, reducing the bias from -6 V to 0 V brings a reduction of efficiency down to 40 %, and a
 1519 reduction in the gain of a factor $\sim 1/3$, while the reduction of the gain of the preamplifier
 1520 allows a reduction of **circa 10, ma da controllare**.

1521 In order to take advantage of the analog pile up and integrating the charge, for
 1522 simplicity assume of two electrons, the second one must hit the pixel before the ToT goes
 1523 under the threshold. The general condition is then $\overline{\Delta T} < \overline{ToT}$, but if a high $P_\mu(n \geq 1)$ is
 1524 required, a lower $\overline{\Delta T}$ may be desired:

$$P(n \geq 1) = \sum_{n=1}^{\infty} \frac{e^{-\mu} \mu^n}{n!} = 1 - P(0) = 1 - e^{-\mu} \quad (5.3)$$

1525

$$\mu = \frac{\overline{ToT}}{\overline{\Delta T}} \quad (5.4)$$

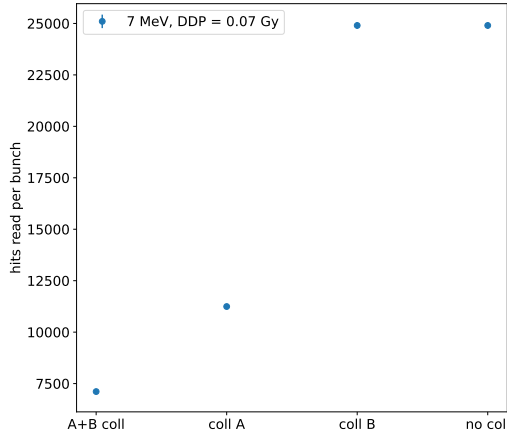


Figure 5.4: Mean number of hits read per bunch at DDP=0.07 Gy, with all the possible setup condition: with both the collimator, with only the collimator far from the chip (A), with only the collimator near the chip (B), and without any collimator.

1526 If a $P_\mu(n \geq 1) = 99\%$ then the $\overline{\Delta T}$ must be $\sim 0.22 \overline{ToT}$. The ToT is in range [0,64] but
 1527 since the rollover must be avoided, the \overline{ToT} must be lower than 32, and then the minimum
 1528 rate on the pixel must be 1.25 MHz.

1529
 1530 During the testbeam many runs have been performed, spanning the energy, the dose
 1531 per pulse and the four possible configurations with/without the collimators. We have
 1532 collected data with the PMOS flavor A in the standard configuration: with the PWELL
 1533 and PSUB biased at -6 V and set the standard default FE parameters reported in table
 1534 ???. During all the data acquisitions we have selected on the control unit of the accelerator
 1535 pulses with t_p of 4 μ m and with the smallest PRF settable, which is 1 Hz, in order to start
 1536 in the most conservative working point excluding the digital pile up of events from different
 1537 bunches. In these conditions, even if the whole matrix turns on, the total readout time
 1538 corresponds to $25000 \times 1 \mu s = 25 \text{ ms}$ is still lower than the time between two consecutive
 1539 pulses. In figure 5.4 is shown the mean number of hits read during one accelerator pulse
 1540 in different setup condition.

1541 The readout starts with the trailing edge of the first pulse going down the threshold:
 1542 about 50 clk=1.25 μ s after this moment the FREEZE signal is sent to the whole matrix,
 1543 and the transmission of the data to the EoC begins. The hits read during the FREEZE
 1544 signal are the ones whose TE occurred before the start of the FREEZE and which have the
 1545 TOKEN signal high; the ones, instead, whose TE occur during the FREEZE are stored in
 1546 the pixel memory until the end of the FREEZE. At this point a second readout starts and
 1547 a second FREEZE is sent to the matrix. An example of the two sub-pulses corresponding
 1548 to an electron bunch is shown in figure 5.5: in the acquisition we injected 5 pulses with
 1549 both the collimators mounted on the table. Looking at the spectrum we can see that the
 1550 second sub-pulse has a populated tail on the right; this is due to the fact that the hits
 1551 which arrive before the start of the first FREEZE but have a long ToT that falls during
 1552 the FREEZE, are read at the second sub-pulse.

1553 The 2D histograms in figure 5.5, reveal an important characteristics of our setup: in

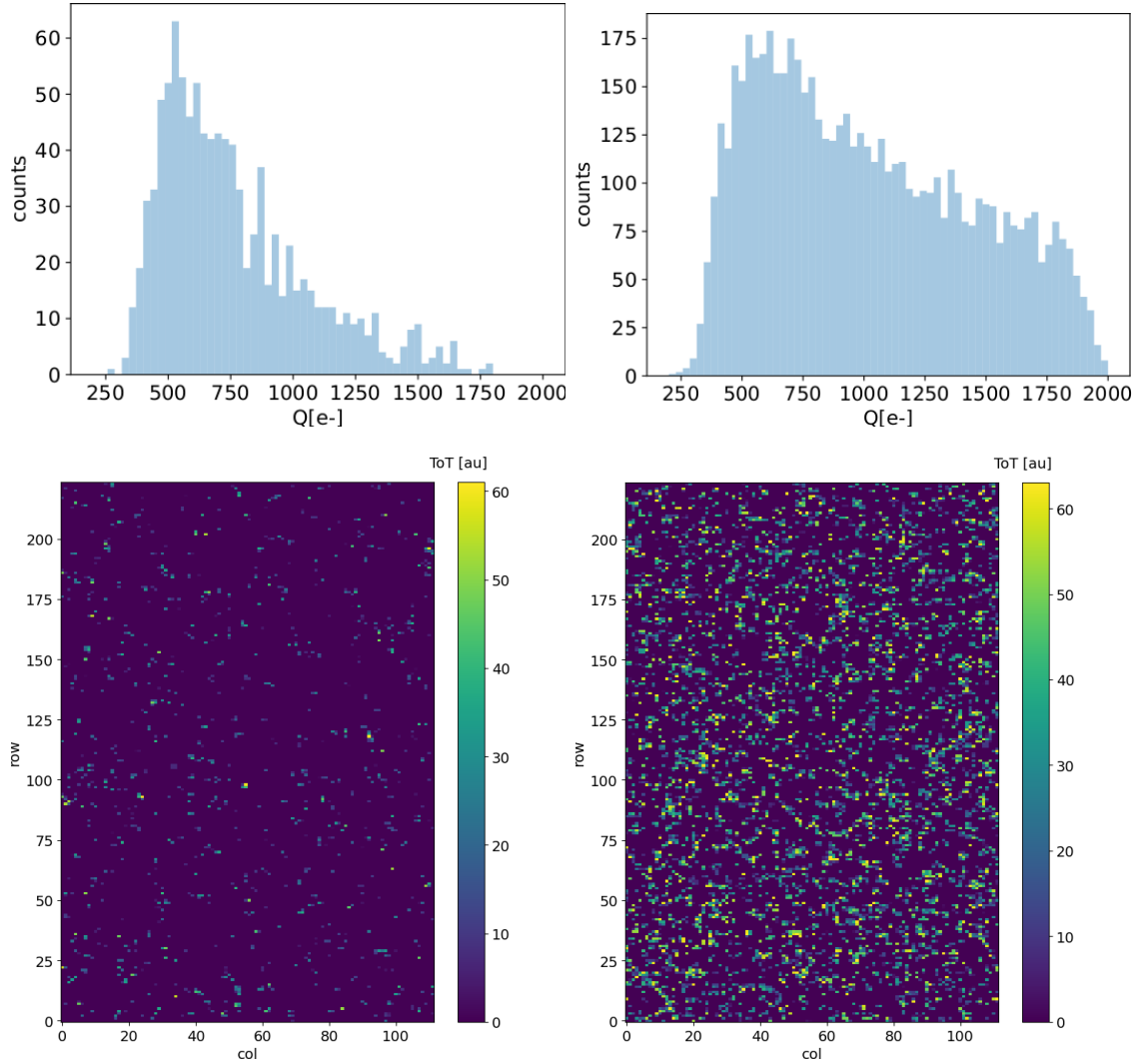


Figure 5.5: Acquisition with both the collimators: 5 pulses at $DDP=0.07\text{ Gy}$. (a) Spectrum of the charge released in the sensor: to apply the conversion I used the information found in the previous chapter. (b) 2D histogram of the ToT of the hits arrived in the sub-pulses.

fact, being uniform and not showing disomogenities, it follows that the collimators do not shield all the particles. We supposed that this was due to a Bremsstrahlung photon background higher than expected but a full verification of that and the analysis of the data is still going on. In figure 5.6, instead, the histograms with a higher DDP value is shown; in the example the matrix turns on completely, but again this happens in two different consecutive read chain.

When we have put aside the collimators, instead, the fluence increase a lot and the two-pulses substructure no more appears (fig. 5.7), but, because of the high attivity of the matrix, after each readout new hits with a fixed ToT were induced due to crosstalk. This problem had already been observed on other prototypes of TJ-Monopix1, and thanks to a simulation it has been observed that the main source of crosstalk is the voltage drop of the pre-amplifier ground as a result of the accumulated current that is drawn from the discriminator.

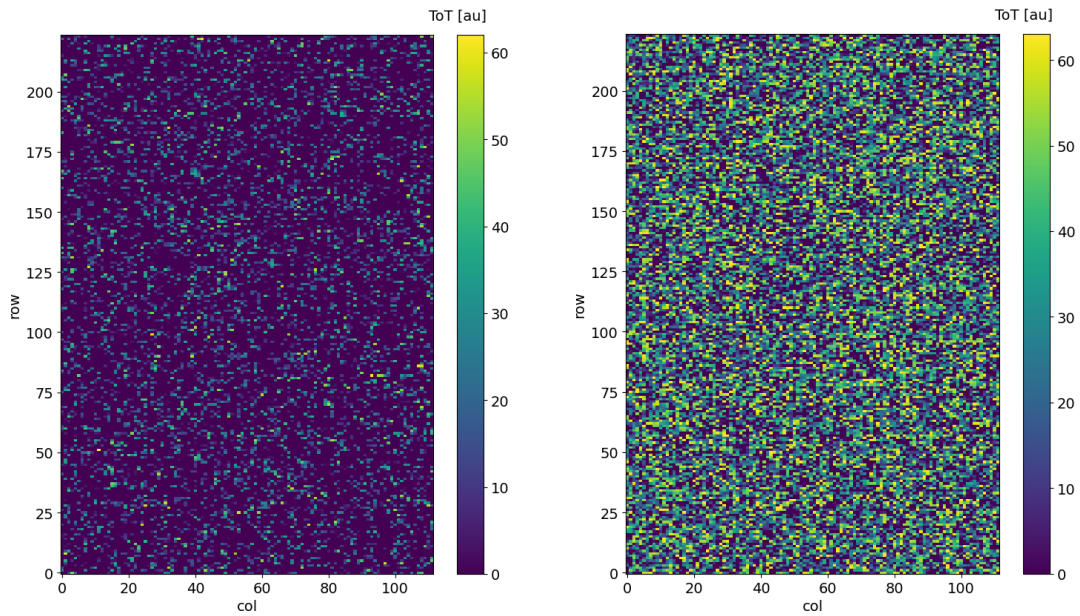


Figure 5.6: Acquisition with both the collimators: 5 pulses at $DDP=0.6\text{ Gy}$. 2D histogram of the ToT of the hits arrived in the sub-pulses. Compared with the previous maps, since the DDP is much higher, more pixels turn on.

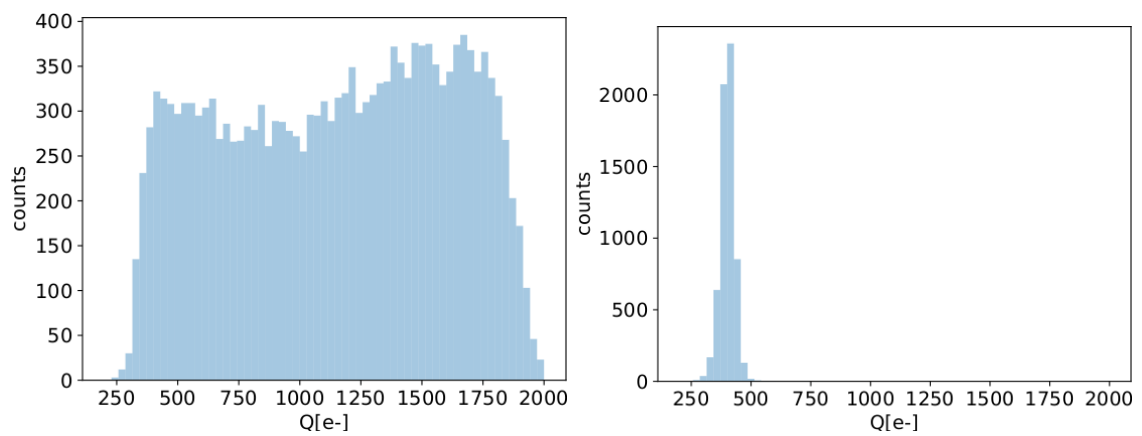


Figure 5.7: Acquisition without any collimator: 5 pulses at $DDP=0.04\text{ Gy}$.

Bibliography

- 1567 [1] W. Snoeys et al. “A process modification for CMOS monolithic active pixel sensors
1569 for enhanced depletion, timing performance and radiation tolerance”. In: (2017).
1570 DOI: <https://doi.org/10.1016/j.nima.2017.07.046>.
- 1571 [2] H. Kolanoski and N. Wermes. *Particle Detectors: Fundamentals and Applications*.
1572 OXFORD University Press, 2020. ISBN: 9780198520115.
- 1573 [3] E. Mandelli. “Digital Column Readout Architecture for 10.1109/NSSMIC.2009.5402399
1574 the ATLAS Pixel 0.25 um Front End IC”. In: (2002).
- 1575 [4] M. Garcia-Sciveres and N. Wermes. “A review of advances in pixel detectors for
1576 experiments with high rate and radiation”. In: (2018). DOI: <https://doi.org/10.1088/1361-6633/aab064>.
- 1578 [5] C. Marinas. “The Belle-II DEPFET pixel detector: A step forward in vertexing in the
1579 superKEKB flavour factory”. In: (2011). DOI: [doi:10.1016/j.nima.2010.12.116](https://doi.org/10.1016/j.nima.2010.12.116).
- 1580 [6] J. Baudot. “First Test Results Of MIMOSA-26, A Fast CMOS Sensor With Inte-
1581 grated Zero Suppression And Digitized Output”. In: (2010). DOI: [doi:10.1109/NSSMIC.2009.5402399](https://doi.org/10.1109/NSSMIC.2009.5402399).
- 1583 [7] A. Dorokhov. “High resistivity CMOS pixel sensors and their application to the
1584 STAR PXL detector”. In: (2011). DOI: [doi:10.1016/j.nima.2010.12.112](https://doi.org/10.1016/j.nima.2010.12.112).
- 1585 [8] Giacomo Contin. “The STAR MAPS-based PiXeL detector”. In: (2018). DOI: <https://doi.org/10.1016/j.nima.2018.03.003>.
- 1587 [9] Nolan Espplen. “Physics and biology of ultrahigh dose-rate (FLASH) radiotherapy:
1588 a topical review”. In: (2020). DOI: <https://doi.org/10.1088/1361-6560/abaa28>.
- 1589 [10] Fabio Di Martino et al. “FLASH Radiotherapy With Electrons: Issues Related to
1590 the Production, Monitoring, and Dosimetric Characterization of the Beam”. In:
1591 *Frontiers in Physics* 8 (2020). ISSN: 2296-424X. DOI: [10.3389/fphy.2020.570697](https://doi.org/10.3389/fphy.2020.570697).
1592 URL: <https://www.frontiersin.org/articles/10.3389/fphy.2020.570697>.
- 1593 [11] M. Dyndal et al. “Mini-MALTA: Radiation hard pixel designs for small-electrode
1594 monolithic CMOS sensors for the High Luminosity LHC”. In: (2019). DOI: <https://doi.org/10.1088/1748-0221/15/02/p02005>.
- 1596 [12] M. Barbero. “Radiation hard DMAPS pixel sensors in 150 nm CMOS technology
1597 for operation at LHC”. In: (2020). DOI: <https://doi.org/10.1088/1748-0221/15/05/p05013>.
- 1599 [13] K. Moustakas et al. “CMOS Monolithic Pixel Sensors based on the Column-Drain
1600 Architecture for the HL-LHC Upgrade”. In: (2018). DOI: <https://doi.org/10.1016/j.nima.2018.09.100>.

- 1602 [14] I. Caicedo et al. “The Monopix chips: depleted monolithic active pixel sensors with
1603 a column-drain read-out architecture for the ATLAS Inner Tracker upgrade”. In:
1604 (2019). DOI: <https://doi.org/10.1088/1748-0221/14/06/C06006>.
- 1605 [15] D. Kim et al. “Front end optimization for the monolithic active pixel sensor of the
1606 ALICE Inner Tracking System upgrade”. In: *JINST* (2016). DOI: doi:10.1088/
1607 1748-0221/11/02/C02042.
- 1608 [16] L. Pancheri et al. “A 110 nm CMOS process for fully-depleted pixel sensors”. In:
1609 (2019). DOI: <https://doi.org/10.1088/1748-0221/14/06/c06016>.
- 1610 [17] L. Pancheri et al. “Fully Depleted MAPS in 110-nm CMOS Process With 100–300-
1611 um Active Substrate”. In: (2020). DOI: 10.1109/TED.2020.2985639.